UNIVERSITY OF GREENWICH

DOCTORAL THESIS

Renewable Energy Supply and Storage: Liquid Metal Battery Stability

---

Author:
Andrejs TUCS

Supervisors:
Prof. Valdis BOJAREVICS
Prof. Koulis PERICLEOUS

A thesis submitted in fulfillment of the requirements
for the degree of Doctor of Philosophy

in the

Computational Science and Engineering Group
Department of Mathematical Sciences

June 25, 2018

Declaration of Authorship

I certify that the work contained in this thesis, or any part of it, has not been accepted in substance for any previous degree awarded to me, and is not concurrently being submitted for any degree other than that of Doctor of Philosophy being studied at the University of Greenwich. I also declare that this work is the result of my own investigations, except where otherwise identified by references and that the contents are not the outcome of any form of research misconduct.

Andrejs Tucs (Author)

Prof. Valdis Bojarevics (Supervisor)

Prof. Koulis Pericleous (Supervisor)

Abstract

Liquid metal batteries (LMBs) offer a new opportunity for large-scale electrical energy storage. The three liquid layer self-segregated structure of the battery provides a number of advantages in comparison to classical batteries: fast kinetics, long lifetime, large current densities, easy recycling. Liquid metal batteries bear a close similarity to aluminium electrolysis cells.

In this work the mathematical model for three density-stratified electrically conducting liquid layers is developed starting with the full 3D formulation, afterwards introducing the shallow layer approximation in order to account for specific MHD effects during periods of battery charge/discharge.

The linear stability model for the interface wave analysis is developed and applied to study the multiple mode interaction. It is found that for the selection of liquid materials most suitable for practical implementation, the interface between the lower (heavy) metal and the electrolyte is significantly more stable than the interface between the electrolyte and the top (lighter) metal. The simplified 2-layer approximation is sufficient in the most of the considered cases for stability prediction of the batteries.

An analytical stability criterion including the dissipation rate is derived for different interaction cases accounting for the cell aspect ratio, the liquid layer electrical conductivities and thicknesses. The criterion is equally applicable to the aluminium electrolysis cells.

A fully coupled 3-layer numerical model based on the spectral function representation has been developed. It is well suited for analysis of the following situations: interaction of the background melt flow and the interface deformations, for the spatially complex, time-dependent distribution of the base electric current and the magnetic field. It was found that for the case when the density difference at the upper interface is much smaller than the density difference at the lower interface, only the

upper interface is significantly deformed in the course of the perturbation growth. The instability onset matches very well with the linear stability model results both for the 2-layer and 3-layer models. This behaviour is similar to the aluminium electrolysis cells. In the case where the density differences at the two interfaces are comparable, both interfaces are significantly deformed, and the behaviour of the system is very different from that of a Hall-Heroult cell. The interfacial waves at the top and bottom interfaces can be coupled either symmetrically or antisymmetrically depending on the initial conditions. The presence of the second deformable interface has a stabilizing effect.

The study covers two LMB design cases for a possible practical implementation: the single collector cell, and the multiple collector cell. The numerical model demonstrates that it is possible to design a stable to dynamic perturbations operating cell if using an optimized bus bar configuration.

Acknowledgements

I would like to express my gratitude to my supervisors Prof. Valdis Bojarevics and Prof. Koulis Pericleous for providing the opportunity for me to undertake a PhD at the University of Greenwich. I am deeply grateful to them for their invariable support, encouragement and trust in my work. My understanding of the subject owes much to their vast experience gained during decades of a front-line research. Prof. V. Bojarevics and Prof. K. Pericleous have been invaluable mentors for me.

Contents

Declaration of Authorship ii

Abstract iii

Acknowledgements v

1 Introduction 1

1.1 Overview . . . 1

1.2 Thesis Objectives . . . 2

1.3 Thesis Outline . . . 4

2 Basic principles 5

2.1 Overview . . . 5

2.2 Concept of Liquid Metal Battery (LMB) . . . 5

2.3 Process governing equations . . . 9

3 Literature Review 13

3.1 Overview . . . 13

3.2 Electro-Vortex Flows (EVF) . . . 13

3.2.1 Theory . . . 13

3.2.2 Experimental observations in the LMB model . . . 15

3.3 Thermal convection . . . 16

3.4 Tayler Instability (TI) . . . 18

3.4.1 Numerical model results related to TI . . . 19

3.5 Pinch-type instability at the rigid edge of a semi-infinite planar sheet carrying a uniform tangential electric current . . . 20

3.6 Shallow water approximation . . . 21

3.6.1 Boussinesq approximation . . . 22

3.7 Long wave interfacial instability . . . 22
3.7.1 Theory for Hall-Heroult Cells (HHC) . . . 22
3.7.2 Extension to 3-layer modelling . . . 27
3.8 Fully coupled models . . . 28
3.8.1 HHC modelling . . . 28
3.8.2 LMB modelling . . . 29
3.8.3 Summary . . . 31

4 3D electric current distribution in the battery **32**
4.1 Overview . . . 32
4.2 Numerical model for electric current flow prediction in 3D . . . 32
4.3 Model results . . . 39

5 Shallow water approximation **43**
5.1 Overview . . . 43
5.2 Interfacial dynamics . . . 43
5.3 Electric current distribution . . . 50
5.4 Fluid dynamics . . . 55
Drag coefficient determination for the layered system . . . 55
5.5 Numerical model for fully coupled 3 shallow layers . . . 64
5.5.1 Interfacial dynamics . . . 64
5.5.2 Electric current flow . . . 67
5.5.3 Fluid dynamics . . . 68
Potential flow . . . 68
Vortical flow . . . 69

6 Linear stability analysis **73**
6.1 Overview . . . 73
6.2 Coupled 3-layer problem . . . 73
6.3 Coupled gravity waves . . . 76
6.4 MHD eigenvalue problem . . . 82
6.5 Stability of cell when aspect ratio is natural number . . . 85
6.6 Stability criteria with friction effect . . . 86

6.7 Numerical example 90

7 Wave dynamics for more realistic battery cases **95**

7.1 Overview 95

7.2 3D magnetic field effect on the stability of LMB 95

7.3 Full interaction with 3D magnetic field 103

7.3.1 Single collector battery 103

7.3.2 Multiple collector battery 107

8 Research Summary and Further Work **111**

8.1 Research Summary 111

8.2 Further Work 113

References **115**

9 Publications and conference presentations produced by this research **122**

List of Figures

1.1 Schematic diagram of LMB basic working principles. 1

2.1 Schematic diagram of a LMB a) discharging, b) charging [2]. 6
2.2 Comparison of the present state of the art in LMB and HHC technologies. 9
2.3 Comparison of the small size vs large size LMB and their integration into the electricity grid. 10

3.1 Electric current passing along a cylindrical conductor [23]. 14
3.2 Current flow through media with different conductivities [23]. 15
3.3 Mixing time ($\tau = L/\langle u^2 \rangle^{1/2}$) variation with current density [4]. 15
3.4 Spatial structure of developed finite-amplitude convection flow [25]. . 17
3.5 "Sausage" and "Spiral" instabilities with longitudinal magnetic field [26]. 18
3.6 Schematic representation of the problem considered in [7, 30]. 19
3.7 Temporal development of EVF in a cylindrical container [7]. 20
3.8 Principle scheme of HHC. `http://www.essentialchemicalindustry.org/metals/aluminium` 23
3.9 Schematic representation of the HHC. 25
3.10 Busbar configuration for Trimet cell [37]. 28
3.11 Metal interface just befor the short circuiting after the anode change [37]. 28
3.12 Minimal relative height of the salt layer depending on the vertical magnetic background field [52]. 31

4.1 Schematic diagram of the LMB discharge for the analysis of collector arrangement impact on the distribution of electric current. 33

4.2 The electric current distribution in the cell with symmetrically arranged collectors. 39
4.3 Schematic representation of the non-optimized collector cell. 40
4.4 The electric current distribution in the non-optimized collector cell. . . 40
4.5 Schematic representation of the optimized collector cell, and possible connections to neighbours. 41
4.6 The electric current distribution in the optimized collector cell. 41

5.1 Schematic diagram of the LMB discharge for the analysis of interfacial wave stability. 44
5.2 1D velocity distribution in the 2-layer system response to differential forcing action $f_1 > f_2$. 59
5.3 1D velocity distribution in the 3-layer system response to a differential forcing action $f_3 > f_1 > f_2$. 64
5.4 Flow chart of the fully coupled 3-layer simulation model. 71

6.1 3-layer coupled gravity waves as initial value problem for different perturbation cases for a Mg||Sb battery: the left hand side corresponds to the interface oscillations at the fixed position ($x = 0$, $y = 0$); the right hand side shows the Fourier power spectra. 78
6.2 3-layer coupled gravity waves as initial value problem for different perturbation cases for a Li||Te battery: the left hand side corresponds to the interface oscillations at the fixed position ($x = 0$, $y = 0$); the right hand side shows the Fourier power spectra. 80
6.3 LMB energy storage costs according to [2]. 82
6.4 Eigenvalue/eigenvector analysis for the upper interface: (a) eigenvalues; (b) eigenvector magnitudes ($|\varsigma_{2,k}| = \sqrt{\mathrm{Re}(\varsigma_{2,k})^2 + \mathrm{Im}(\varsigma_{2,k})^2}$) with the incremental rise of magnetic field $B_z = B_z^0 + \Delta B$, where $0 \leq B_z \leq 3$ mT, $\Delta B = 0.1$ mT, $L_x / L_y = 2.2$. 84

6.5 Comparison of the growth increment dependency on applied magnetic field for the 2-layer and 3-layer models for various values of the electrolyte thickness for cells with different aspect ratio: (a) $(1,0)+(0,1)$ ($L_x = L_y = 5.36$ m); (b) $(1,1)+(2,0)$ ($L_x = 7.58$ m, $L_y = 3.79$ m); (c) $(4,1)+(5,0)$ ($L_x = 9.29$ m, $L_y = 3.09$ m); (d) $(7,1)+(8,0)$ ($L_x = 10.73$ m, $L_y = 2.68$ m). 86

6.6 The critical stabilizing friction dependency on the magnetic field for two mode interaction: the thick lines from the asymptotic relations (6.33), the thin lines (6.26). The symbols $(\star)$ indicate representative numerical test cases shown in the Figure 6.8. 89

6.7 Critical stability comparison for different battery compositions: (■) linear stability for the 2-layers, (●) linear stability for the 3-layers, (▲) decoupled 2 interface simulation, (♦) fully coupled 3-layer simulation. 1) Li||Te, 2) Na||Sn, 3) Li||Bi, 4) Li||Pb, 5) Na||Bi, Na||Pb, 6) Li||Zn, 7) Li||Sn, 8) Ca||Sb, 9) Ca||Bi, 10) Mg||Sb. 91

6.8 Numerical results for the top interface oscillation at a fixed position ($x = 0$, $y = 0$) following the initial $(1,0)$ mode perturbation at $A = 0.005$ m: a) oscillation in the frictionless case ($\gamma = 0$) for subcritical and overcritical magnetic fields, b) the power spectra for $\gamma = 0$ cases, the black triangles mark the gravity wave frequencies, c) oscillation in the presence of friction , d) the power spectra for two friction coefficients at the marginally stable and unstable cases, e) oscillation at higher friction ($\gamma = 0.05\ \mathrm{s}^{-1}$) for B_z near stability limit, f) the spectral peaks near the stability limit. 92

6.9 The computed interface of growing amplitude with the friction $\gamma = 0.02$ and $B_z = 1$ mT. The frames at 10 s illustrate the $(1,0)+(0,1)$ and $(2,1)+(3,0)$ mode interactions. 94

6.10 The computed interface of growing amplitude with $\gamma = 0.05$ and $B_z = 1.3$ mT. The frames show the $(1,0)+(0,1)$ mode interaction. 94

7.1 Comparison of the interfacial oscillations at fixed positions for $I = 75$ kA, $h_{1,3} = 20$ cm, $h_2 = 5$ cm for the two magnetic field cases. 96

7.2 The computed interfaces of growing amplitude for the cell with non-optimized magnetic field distribution at $I = 75$ kA, $h_{1,3} = 20$ cm, $h_2 = 5$ cm. 97
7.3 The computed interfaces of growing amplitude for the cell with optimized magnetic field distribution at $I = 100$ kA, $h_{1,3} = 10$ cm, $h_2 = 2$ cm. 98
7.4 Interfacial oscillation at a fixed position comparison of the decoupled (blue line) and fully coupled (red line) approximation for the non-optimized cells magnetic field distribution ($h_{1,3} = 20$ cm, $h_2 = 5$ cm). . 100
7.5 Comparison of the computed spectra of the decoupled (blue line) and fully coupled (red line) models for the non-optimized magnetic field ($h_{1,3} = 20$ cm, $h_2 = 5$ cm). 101
7.6 Example of the multiphysical coupling in the cell with non-optimized magnetic field when $I = 75$ kA, $h_2 = 5$ cm, $t = 999.2$ s. The lower row corresponds to the lower metal, the upper row corresponds to the upper metal. 102
7.7 Schematic representation of the single collector battery. 103
7.8 Magnetic field distribution in the two metal electrodes for the single collector battery ($I = 50$ kA and $h_2 = 5$ cm). 103
7.9 The return circuit effect on the magnetic field distribution in the top metal ($I = 50$ kA and $h_2 = 5$ cm). 104
7.10 The return circuit effect on the velocity field distribution in the bottom metal ($I = 50$ kA and $h_2 = 5$ cm). 104
7.11 Schematic representation of the single collector battery with rearranged current connector, with added ferromagnetic box. 105
7.12 The effect of the steel box on the magnetic field distribution in the top metal ($I = 50$ kA and $h_2 = 5$ cm). 105
7.13 Oscillation patterns for top and bottom metal/electrolyte interfaces and the computed Fourier spectra for $I = 100$ kA and $h_2 = 8$ cm [38]. . 106
7.14 The final computed stable interfaces for the single collector cell ($I = 100$ kA and $h_2 = 8$ cm) [38]. 106
7.15 Schematic representation of the optimized collector cell (Trimet). . . . 107

7.16 The non-optimized cell ($I = 100$ kA, $h_2 = 8$ cm) versus the optimized cell ($I = 100$ kA, $h_2 = 2.5$ cm) top metal oscillation [38]. 108

7.17 The final computed stable interfaces for the multiple collector cell ($I = 75$ kA and $h_2 = 2$ cm) [38]. 109

7.18 Velocity distribution in positive electrode, electrolyte and negative electrode for the single collector battery (on the left) at $I = 50$ kA with $h_2 = 5$ cm and the multiple collector battery (on the right) at $I = 75$ kA with $h_2 = 2$ cm [38]. 110

List of Tables

1.1 Candidate metals for LMB electrodes and corresponding material properties at reference temperature (near melting point) [6]. 2

2.1 Technology comparison of potential batteries [2, 12, 13]. 6
2.2 Equilibrium cell voltages from full-charge to full-discharge (V) of A-B electrode couples [2]. 8
2.3 Estimated cost of energy for $A - B$ electrode couple candidates ($\$\,\mathrm{kWh}^{-1}$) [2]. 8

6.1 Material parameters used in numerical examples: density ρ, kinematic viscosity ν, conductivity σ of the three fluids comprising magnesium-based LMB ($\triangle\rho_1 \gg \triangle\rho_2$). 77
6.2 Material parameters used in numerical examples: density ρ, kinematic viscosity ν, conductivity σ of the three fluids comprising lithium-based LMB ($\triangle\rho_1 \approx \triangle\rho_2$). 79

List of Symbols

Symbol	Meaning	Units
$\boldsymbol{B}$	magnetic field vector	T
$\boldsymbol{E}$	electric field vector	$\mathrm{V\,m^{-1}}$
E	electromagnetic interaction parameter	-
$\boldsymbol{F}$	depth averaged Lorentz force vector	N
$\boldsymbol{f}$	Lorentz force vector	N
g	gravity of Earth	$\mathrm{m/s^2}$
$G_{k,k'}$	interaction matrix	-
h	layer thickness	m
Ha	Hartmann number	-
I	total electric current	A
$\boldsymbol{j}$	electric current density vector	$\mathrm{A\,m^{-2}}$
$\boldsymbol{k}$	wave vector	$\mathrm{m^{-1}}$
k_f	friction coefficient	$\mathrm{s^{-1}}$
L_x, L_y	horizontal dimensions	m
$\boldsymbol{n}$	normal unit vector	-
p	pressure	Pa
$\boldsymbol{r}$	radius vector	-
Re	Reynolds number	-
Rm	magnetic Reynolds number	-
t	time	s
$T_n(z)$	Chebyshev polynomials of the first kind	-
$\boldsymbol{U}$	depth averaged fluid velocity vector	$\mathrm{m\,s^{-1}}$
$\boldsymbol{u}$	fluid velocity vector	$\mathrm{m\,s^{-1}}$
x, y, z	Cartesian coordinates	m

γ	friction coefficient	s^{-1}
Δt	time step	s
δ	depth parameter (ratio of layer thickness to horizontal dimension)	-
∂_i	special derivative	-
∂_t	temporal derivative	-
η	dynamic viscosity	$\mathrm{Pa\,s}^{-1}$
ϵ	amplitude parameter (ratio of wave amplitude to layer thickness)	-
ϵ_0	electric permittivity	$\mathrm{F\,s}^{-1}$
ζ_1, ζ_2	interfacial displacements of the lower and upper metal	m
μ	complex eigenvalue	s^{-1}
μ_m	magnetic permeability	$\mathrm{N\,A}^{-2}$
ν	kinematic viscosity	$\mathrm{m}^2\,\mathrm{s}^{-1}$
$\boldsymbol{\nabla}$	gradient	-
∇^2	Laplace operator	-
$\boldsymbol{\nabla}\cdot$	divergence	-
$\boldsymbol{\nabla}\times$	curl	-
ρ	density	$\mathrm{kg\,m}^{-3}$
σ	electrical conductivity	$\mathrm{S\,m}^{-1}$
Φ	perturbed electric potential	V
φ	electric potential	V
ϕ	velocity potential	s^{-1}
ψ	stream function	s^{-1}
ω_k	shallow layer gravity wave frequency	m^{-1}

Chapter 1

Introduction

1.1 Overview

Liquid Metal Batteries (LMBs) enable ultra-fast electrode charge-transfer kinetics due to liquid-liquid electrode-electrolyte interfaces, high rate capability, low ohmic losses, as well as rapid mass transport of reactants and products to and from the electrode-electrolyte interface by liquid-state diffusion [1–3]. The aforementioned properties allow LMBs to operate with relatively high voltage efficiencies at high current densities. Such characteristics are essential for practical use of these batteries on a national power grid scale (Figure 1.1).

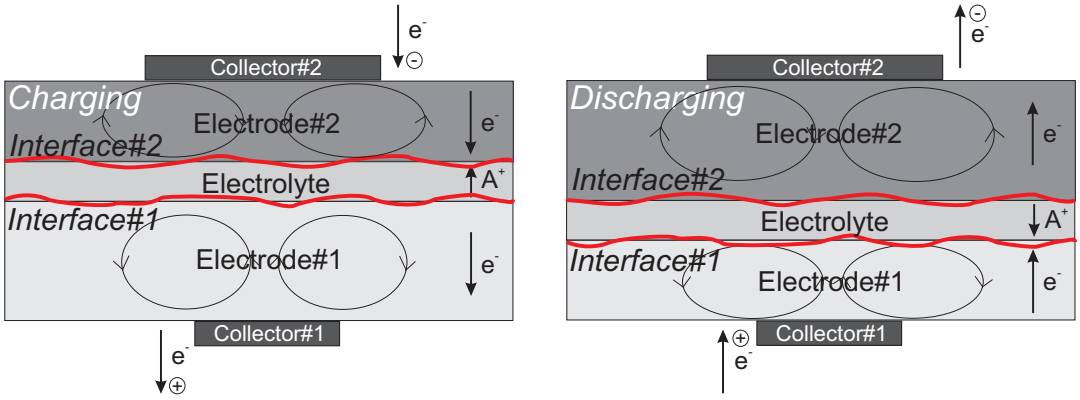

FIGURE 1.1: Schematic diagram of LMB basic working principles.

LMBs also have the important advantage of being low cost because many of the candidate electrode materials are earth-abundant and inexpensive (Table 1.1). The density segregation of the active liquid components allows simpler, lower-cost cell fabrication compared with that of conventional batteries. One of the most important features of this type of batteries is the continuous creation and partial annihilation of the liquid metal electrodes during the charge-discharge cycling (see Figure 1.1).

Electrode	Atomic number	Density, $kg\,m^{-3}$	Electrical conductivity, $S\,m^{-1}\cdot 10^6$	Reference temperature, ^0C	Averaged monthly prices, $\$\,mol^{-1}$
Negative					
Li	3	525.0	4.17	180.5	0.430
Na	11	809.0	10.37	97.0	0.057
Mg	12	1585.7	3.65	650.0	0.069
Ca	20	1365.0	4.00	865.0	0.140
Positive					
Zn	30	6025.0	2.67	419.5	0.150
Ga	31	6090.0	3.85	29.8	51.000
In	49	7023.0	3.09	156.6	74.000
Sn	50	7000.0	2.12	232.0	3.200
Sb	51	6483.0	0.88	630.5	1.800
Pb	82	10678.0	1.05	327.0	0.520
Bi	83	10068.0	0.78	217.0	4.900

TABLE 1.1: Candidate metals for LMB electrodes and corresponding material properties at reference temperature (near melting point) [6].

This gives LMBs the potential for outstanding life cycle with immunity to micro-structural electrode degradation mechanisms.

The above picture must be moderated by the fact that, at very large scales, high magnitude electric current passing through LMBs is able to trigger MHD instabilities. Some fluid movement is certainly desirable [4], but there is a danger of a short circuit when the motion becomes too intense. As in the case of the aluminium electrolysis cells, the thickness of the low conductive salt layer has to be kept above a critical threshold to avoid interfacial instabilities [5]. It is therefore necessary to assess all the factors essential for the stable operation of LMBs before contemplating any significant commercialization, and one of the objectives of this Thesis is to contribute to this effort.

1.2 Thesis Objectives

Depending on the battery cross section, which determines the current density, and the projected charge/discharge time, different types of instabilities may arise in the LMBs. Taller cells with high ratio of the depth to horizontal dimension are most susceptible to Tayler Instability (TI) [7]. In contrast, shallow cells with large interfacial area (most suitable for large-scale energy output [8]) are dominated by interfacial

waves, which have broad similarities to MHD waves observed in Hall-Heroult Cells (HHC) [9]. This research is focused on the large scale batteries with shallow geometries similar to the HHC due to the expected higher efficiency. The main focus of this Thesis is MHD driven interfacial instabilities. The electrochemical and heat transfer aspects are not investigated in this study, as these are expected to be less important for the interfacial stability. Global and local heat transfer will be neglected when analyzing the motion of free interfaces and the electrically induced flow in the volume. Due to the relatively high thermal conductivities of metal electrodes the local Joule heating variation is assumed to be uniform and balanced by external loss at the boundaries. It is assumed that densities in each of the layers are constant and uniform.

At the initial stage of the research the literature review will be presented on the relevant subjects.

For proper functionality of LMBs density stratification is essential. Thorough understanding of the interplay of electromagnetic forces and the gravity stratification is required to assess LMB scaling specifics. The driving goal of this research is to study the interfacial stability and the fluid dynamics of the fluid layers carrying an electric current. The set of equations for three density-stratified electrically conductive liquid layers will be derived using the beneficial (from the computational point of view) shallow water approximation [10], taking into account the specific MHD effects during periods of battery charge/discharge.

The final set of equations to describe coupled physical effects are non-linear and not easy to solve using classical analytical methods for realistic cases. Therefore an essential component of this research will involve development and verification of numerical code due to high accuracy based on spectral function representation [11].

For the purpose of the numerical model validation and for better understanding of basic physical mechanisms it is also planned to perform linear stability analysis of the interfacial waves in the presence of MHD interaction.

After the numerical model verification it is essential to find the optimized system configuration leading to LMB design for industrial implementation when accounting for the obtained physical correlations.

1.3 Thesis Outline

This Thesis consists of eight chapters. In Chapter 2 the fundamental concepts of the LMB electro-chemistry and technological requirements are discussed. Set of the governing equations is presented. In Chapter 3 a review of the literature is made, which covers main topics relevant to the MHD phenomena in LMB. Chapter 4 presents the design, development, and implementation of a 3D numerical model for the electric current in the LMB. In Chapter 5 the mathematical model based on shallow water approximation and the fully coupled 3-layer numerical model are presented. Chapter 6 is devoted to the linear stability model for the interface wave analysis which is applied to study the multiple mode MHD interaction. In Chapter 7 decoupled 2 interface simulation is validated against the fully coupled 3-layer simulation for the given 3D magnetic field. Numerical results for two LMB design cases suitable for a possible practical implementation are compared for the single and the multiple collector cell. Chapter 8 contains a summery and conclusions along with opportunities for further work.

Chapter 2

Basic principles

2.1 Overview

In this chapter the fundamentals of the LMB electro-chemistry and technological requirements are discussed. A set of the process governing equations is presented.

2.2 Concept of Liquid Metal Battery (LMB)

Recent achievements with liquid metal battery technology [2, 3, 8, 14–20] suggest that this battery type can compete with conventional batteries (see the Table 2.1). Nevertheless, electrode and electrolyte property adjustment is essential for optimal results. One of the LMB drawbacks is its sensitivity to motion. LMBs are for stationary use therefore.

To identify suitable components for the system the characteristic voltage and electrode material cost per unit of energy storage capacity must be carefully analysed.

The theoretical voltage of electrochemical cells is determined by the thermodynamic properties of the electrode materials. For LMBs, there exist over 100 possible binary alloy electrode combinations [2]. Cell equilibrium voltage is defined by a following equation

$$E_{\text{cell},eq} = -RT/(z_e F) \ln a_{A(\text{in } B)}, \tag{2.1}$$

where R is the universal gas constant, F is the Faraday constant, T stands for the operating temperature in the system and z_e is the number of electrons exchanged

Type	Operating temperature, ^{0}C	Specific energy, Whkg^{-1}	Open circuit voltage, V	Lifetime, cycle	Cost, \$(kWh)$^{-1}$
Lead acid	-40-60	25-40	2.1	≈1000	200-400
Ni-Cd	-10-45	30-45	1.35	2000	800-1500
Na-S	300-350	150-240	2.1	4500	400-555
ZEBRA	300-350	95-120	2.6	3000	400-900
Li-ion	-25-40	155	3-4	4500	500-1420
LMB	>200	50<...<200	<1	>10000	<150

TABLE 2.1: Technology comparison of potential batteries [2, 12, 13].

during the reaction and $a_{A(\text{in}\,B)}$ is the activity. The thermodynamic force for cell discharge resulting from a strong interaction of metal A with metal B, see Figure 2.1.

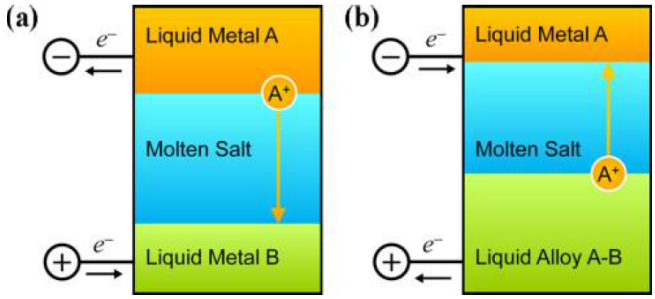

FIGURE 2.1: Schematic diagram of a LMB a) discharging, b) charging [2].

Another important parameter for the LMB is its operating temperature. The minimum cell operating temperature is defined by the melting point of the electrolyte and both electrode materials. A reduction of the cell operating temperature decreases impact of corrosion and self-discharge, as well as simplifies sealing and thermal management [2, 21]. The use of pure metals is not mandatory. LMB electrodes composed of alloys are allowing operation at lower temperatures, which improves electrical performance and extends service lifetime.

Negative electrodes. The alloy $(A - A')$ of the active component A in the negative electrode must remain less dense than the electrolyte and only incorporate elements (A'), which are more noble than component A, to avoid reacting with the electrolyte [2, 3]. The Ca-Mg system for Ca-based cells is an example that satisfies these requirements. In selecting the negative electrode, the negative impact of reduced cell voltage must be balanced with the positive impact of a metal solubility suppression in the electrolyte.

Positive electrodes. A positive electrode material (B) alloying with a second component (B') leads to the formation of an $A - B - B'$ ternary alloy during cell discharge. Binary systems of electropositive elements often exhibit deep eutectics, which are substantially reducing the operation temperature, as it is in case of the Sb-Pb system [2].

Electrolyte. The operation of a rechargeable LMB cell with candidate electrode couples requires suitable electrolytes having the following characteristics [2, 3]:

- low melting temperature
- minimal metal solubility
- no irreversible side reactions
- a density which is intermediate between the positive and negative electrodes
- high ionic conductivity

Candidate electrode systems can be compared based upon the equilibrium cell voltages from the perspective of the cost per energy (\$ kWh^{-1}), see Table 2.2. Table 2.3 summarises the estimated cost of energy for different electrode couple candidates. From these data, a few important conclusions can be made. The range in material prices spans 5 orders of magnitude, while cell voltage values vary by less than 1 order of magnitude, emphasising the importance of a cost metric consideration when selecting candidate electrode couples. Price fluctuations are much more pronounced for positive (B) than for negative (A) electrode materials. From the Table 2.3, it can be seen that the high prices and/or the low equilibrium cell voltages of some metal combinations is significant draw back of their application in grid-scale energy storage. From Table 2.3 it follows that Sb-based couples have the best characteristics with corresponding cell voltages typically above 0.70 V.

Modern experimental LMBs are reaching size in the order of 20 cm (see Figure 2.2 (a)). On the other hand the modern Hall-Heroult Cells (HHC) are typically of about 20 m scale (see Figure 2.2 (b)). There is a significant scale difference between both technologies, however the operational principles are very similar. In a sense, LMB may be considered as an aluminium plant running in reverse, producing power

	A					
B	Li	Na	K	Mg	Ca	Ba
Zn	0.31−0.07			0.21−0.08	0.44−0.17	
Cd	0.56−0.37	0.22−0.02		0.21−0.09		
Hg		0.67−0.13	0.72−0.07			
Al	0.30−0.30			0.20−0.07	0.44−0.41	0.53−0.15
Ga	0.59−0.57	0.20−0.01		0.25−0.14		
In	0.55−0.50	0.30−0.06	0.24−0.02	0.24−0.11	0.62−0.34	
Tl		0.42−0.11	0.44−0.07	0.23−0.12		
Sn	0.70−0.57	0.45−0.22		0.35−0.19	0.77−0.51	1.08−0.71
Pb	0.68−0.42	0.47−0.20	0.51−0.15	0.21−0.13	0.69−0.50	1.02−0.66
Sb	0.92−0.92	0.86−0.61	1.01−0.54	0.51−0.39	1.04−0.94	1.40−1.15
Bi	0.86−0.77	0.74−0.47	0.90−0.45	0.38−0.27	0.90−0.79	1.30−0.97
Te	1.76−1.70	1.75−1.44	2.10−1.47			

TABLE 2.2: Equilibrium cell voltages from full-charge to full-discharge (V) of A-B electrode couples [2].

	A					
B	Li	Na	K	Mg	Ca	Ba
Zn	110			26	26	
Cd	65	140		100		
Hg		31	510			
Al	61			27	12	52
Ga	3300	18000		9600		
In	5300	15000	23000	16000	5600	
Tl		170000	180000	250000		
Sn	210	370		440	190	150
Pb	64	64	630	120	36	40
Sb	89	93	330	150	69	64
Bi	240	300	550	560	220	170
Te	950	1000	1000			

TABLE 2.3: Estimated cost of energy for $A - B$ electrode couple candidates (\$ kWh^{-1}) [2].

instead of consuming it. The advantage of using a few relatively large batteries (with large horizontal dimensions compared to vertical ones) in comparison to the very large number of small batteries for the same capacity is the considerably reduced heat loss, as well as better magnetic stability conditions and simpler construction as it is illustrated in the Figure 2.3.

The reference [8] analyses from electrochemical point of view Na||Zn battery. LMB is proposed as a power buffer in an aluminium plant. The battery with dimensions $L_x \times L_y = 14$ m^2 of 1.4 m height is positioned in an idled potline. The existing infrastructure of aluminium reduction plant such as as buildings, rectifiers, potshells, and busbars were utilized for the battery implementation. Relatively good efficiency rates were obtained. As one of the future developments it was emphasised the importance of MHD stability analysis of the grid-scale LMB.

(a) Current state of experimental LMBs.
http://www.donaldsadoway.com/ds_projects/

(b) Modern aluminium smelter plant, DUBAL, Dubai.
http://primary.world-aluminium.org/processes/reduction/

FIGURE 2.2: Comparison of the present state of the art in LMB and HHC technologies.

2.3 Process governing equations

Systematic derivation of the MHD equations for the continuous media most often used in different practical applications is given in many well-known monographs

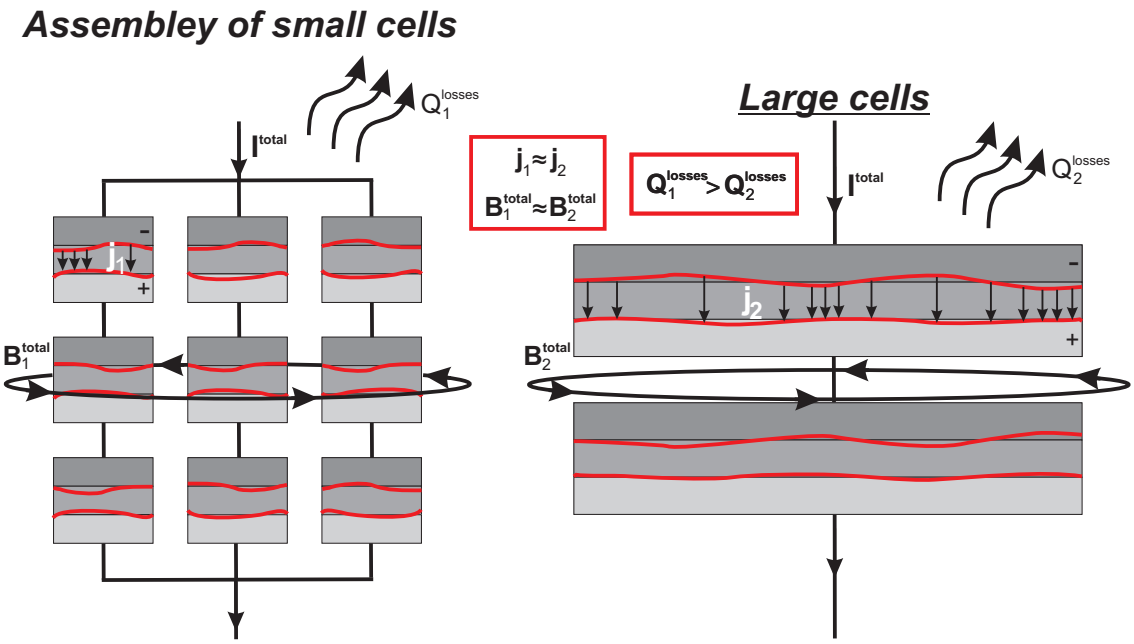

FIGURE 2.3: Comparison of the small size vs large size LMB and their integration into the electricity grid.

(see, for example, [22, 23]). In this Section only the basic assumptions will be provided which are used to obtain the final set of the equations. The medium is electrically conducting (its conductivity is high enough) and without free charges. Physical processes under consideration do not vary too rapidly which allows low-frequency approximation, with typical velocities much smaller than the velocity of light. The displacement current and the convection current can be neglected compared to the conduction current.

The physical properties of the incompressible medium are assumed to be homogeneous, isotropic, except of the magnetic permeability, and independent of temperature, magnetic field and other conditions. Taking into account these assumptions the set of MHD equations consists of

Momentum transfer:

$$\rho[\partial_t \boldsymbol{u} + (\boldsymbol{u} \cdot \boldsymbol{\nabla})\boldsymbol{u}] = -\boldsymbol{\nabla}(p + \rho g z) + \rho\nu\nabla^2\boldsymbol{u} + \boldsymbol{j} \times \boldsymbol{B}, \tag{2.2}$$

Continuity:

$$\boldsymbol{\nabla} \cdot \boldsymbol{u} = 0, \tag{2.3}$$

Maxwell's equations:

$$\nabla \cdot \boldsymbol{B} = 0, \tag{2.4}$$

$$\boldsymbol{j} = \frac{1}{\mu_0} \nabla \times \boldsymbol{B}, \tag{2.5}$$

$$\partial_t \boldsymbol{B} = -\nabla \times \boldsymbol{E}, \tag{2.6}$$

$$\nabla \cdot \boldsymbol{E} = 0, \tag{2.7}$$

Ohm's law for moving media:

$$\boldsymbol{j} = \sigma(\boldsymbol{E} + \boldsymbol{u} \times \boldsymbol{B}), \tag{2.8}$$

Charge conservation:

$$\nabla \cdot \boldsymbol{j} = 0. \tag{2.9}$$

The set of equations (2.2)-(2.9) can be simplified for a stationary case [23]. In this case the electric field is irrotational (from (2.6) it follows that $\nabla \times \boldsymbol{E} = 0$) and the electric field potential φ can be introduced:

$$\boldsymbol{E} = -\nabla \varphi, \tag{2.10}$$

The equation for the potential can derived by Ohm's law substituting there (2.10) and taking divergence, and using (2.9), it can be obtained

$$\nabla^2 \varphi = \nabla \cdot (\boldsymbol{u} \times \boldsymbol{B}). \tag{2.11}$$

The magnetic field distribution can be described by the Biot-Savart law

$$\boldsymbol{B} = \frac{\mu_0}{4\pi} \int_V \frac{\boldsymbol{j} \times \boldsymbol{r}}{r^3} d\tau, \tag{2.12}$$

which is an integral form of equation (2.5). Additionally, if the magnetic material presence is accounted, the equation for the magnetic permeability should be included

$$\mu_m = \mu_m(\boldsymbol{H}), \tag{2.13}$$

where $\boldsymbol{H}$ is the total magnetic field intensity which accounts for electric current self induced field and steel element impact on it, whereas $\boldsymbol{B} = \mu_m \boldsymbol{H}$.

In the most part of this Thesis the medium is considered as non-magnetic (its magnetic permeability is very close to the permeability of free space) except in the Chapter 7. This means that equation 2.13 in the following chapters will be left out. The relevant boundary conditions for the considered set of equations will be provided in Chapter 4 and 5.

Chapter 3

Literature Review

3.1 Overview

In this chapter a review of literature is given. The review focuses on these main topics relevant to the MHD phenomena in LMB: fundamentals of electro-vortex flows, thermal convection, Tayler instability, long wave interfacial instabilities in two and three layer systems, current state of the art in fully coupled modelling of these phenomena.

3.2 Electro-Vortex Flows (EVF)

3.2.1 Theory

Electrically induced flows, as described in Bojarevics *et al.* [23], are resulting from the electromagnetic force caused by the interaction of electric current, supplied from an external source of EMF, with the self-magnetic field. The first step of the evaluation of the force field is a determination of the electric current density $\boldsymbol{j}$ distribution in the fluid volume and the supplying circuit defined by the electric field potential φ. This is done by means of solving equation (2.11) accounting for the corresponding boundary conditions. The next step in the construction of the electromagnetic force is evaluation of the magnetic field induction by means of the Biot-Savart law (2.12). After determination of the field distribution $\boldsymbol{B}$, the electromagnetic force $\boldsymbol{f} = \boldsymbol{j} \times \boldsymbol{B}$ can be evaluated at any point of interest at which the current density $\boldsymbol{j}$ is specified.

The important question is whether the electromagnetic force is potential ($\boldsymbol{\nabla} \times \boldsymbol{f} = \boldsymbol{0}$) or rotational ($\boldsymbol{\nabla} \times \boldsymbol{f} \neq \boldsymbol{0}$). The question of the potential or rotational nature

of the electromagnetic force is equivalent to the question of whether the fluid will remain motionless or will it be set into motion if the electric current passes through it, if the velocity field boundary conditions are homogeneous and the medium is at rest without the electric current supply. The electromagnetic force can be represented as the superposition of a purely potential part and the remaining part, which may include both the potential and rotational parts of the force [23]:

$$\boldsymbol{f} = \boldsymbol{j} \times \boldsymbol{B} = \frac{1}{\mu_0}[(\boldsymbol{\nabla} \times \boldsymbol{B}) \times \boldsymbol{B}] = \underbrace{-\boldsymbol{\nabla}\left(\frac{|\boldsymbol{B}|^2}{2\mu_0}\right)}_{\text{Potential part}} + \underbrace{\frac{1}{\mu_0}(\boldsymbol{B} \cdot \boldsymbol{\nabla})\boldsymbol{B}}_{\text{Vortical part}}. \tag{3.1}$$

Formally the potential part of electromagnetic force can be included in the pressure gradient term. This part of the force will lead to a pressure redistribution in the current carrying volume.

Let us consider an example, the electric current $j_x(y,z)$ passing along a cylindrical liquid conductor of arbitrary cross section (see Figure 3.1). The electric current induces a magnetic field with B_y and B_z components, it is described by means of the relation

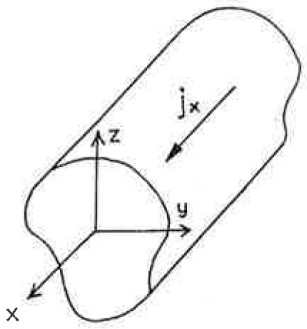

FIGURE 3.1: Electric current passing along a cylindrical conductor [23].

$$j_x = \frac{1}{\mu_0}\left(\partial_y B_z - \partial_z B_y\right). \tag{3.2}$$

The electromagnetic force has the components $f_y = -j_x B_z$ and $f_x = j_y B_x$. The corresponding curl of the force can be expressed as

$$(\boldsymbol{\nabla} \times \boldsymbol{f})_x = \partial_y f_z - \partial_z f_y = B_z \partial_z j_x + B_y \partial_y j_x. \tag{3.3}$$

On the basis of expression (3.3) it can be concluded that, if the electric current density is constant in the cross-section of the conductor, the right-hand side of (3.3) is equal to zero. In this particular case the effect of electromagnetic force leads only to a pressure redistribution over the conductors cross section, and the fluid motion is not present [23].

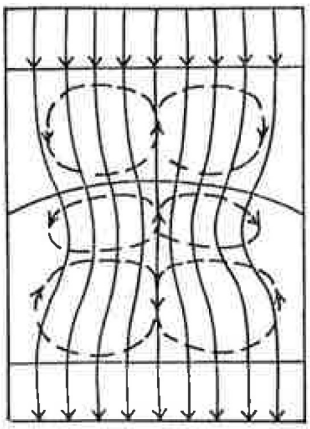

FIGURE 3.2: Current flow through media with different conductivities [23].

If the electrical conductivity is nonuniform, for instance, due to a layered structure of the system, containing free interfaces, like it is in the case of LMB, the electromagnetic force may become rotational for a unidirectional current distribution as it is shown in Figure 3.2.

3.2.2 Experimental observations in the LMB model

Kelley *et al.* [4] analysed a mixing in the convecting molten positive electrode (ePbBi) of a liquid metal battery (cylindrical vessel with diameter $D = 88.9$ mm and 67 mm deep). Ultrasound velocimetry technique was used for the flow measurement in the liquid metal electrode while the current density was varied: $0 \leq j_0 \leq 375$ mA cm^{-2}. It was found that as the current density increases, the flow becomes faster and more regular, which was explained in [4] by the alignment of Benard cells with magnetic field lines. As the current density increases further, the flow develops high-frequency temporal oscillations, likely to lead to a wave-type instability. It was found that this leads to a sharp onset in mixing efficiency at $j_0 = 50$ mA cm^{-2} (see Figure 3.3). This experiment was recently reproduced in [24], and relatively good agreement was found. The fact that mixing improves with the rise of current density extends the rate capability of liquid metal batteries.

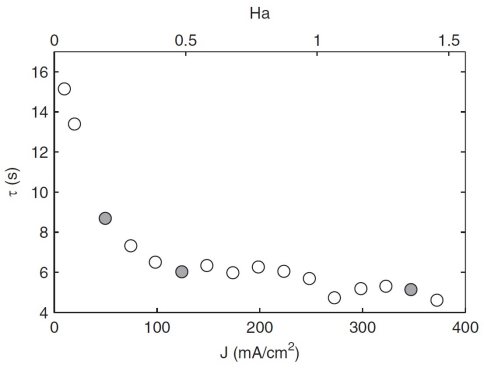

FIGURE 3.3: Mixing time ($\tau = L/\langle u^2 \rangle^{1/2}$) variation with current density [4].

3.3 Thermal convection

Generation of thermal convection flow in the liquid metal battery was numerically analysed by Shen & Zikanov [25]. The following assumptions were made

- A cell was of cylindrical shape. The sidewalls of the battery were assumed thermally and electrically perfectly insulating.
- The current collectors (the top and bottom walls) were assumed to be perfectly electrically conducting and are modelled as equipotential boundaries.
- The electrical and thermal conductivities are assigned as the distinct and realistic values in each layer. For the other physical properties, such as density, viscosity, specific heat, and thermal expansion coefficient, the typical values of the electrolyte are used in all three layers. The thicknesses and physical properties of the three layers were assumed constant.
- The applied electrical current is passing between the top and bottom collector. It is constant, with uniform density

$$\boldsymbol{j}_0 = j_0 \boldsymbol{e}_z, j_0 = const. \tag{3.4}$$

  The current generates a constant, uniform, and purely azimuthal magnetic field

$$\boldsymbol{B}_\theta = B_\theta(r)\boldsymbol{e}_\theta = \frac{\mu_0 j_0 r}{2}\boldsymbol{e}_\theta. \tag{3.5}$$

- The interfaces between the layers were modelled as undeformable, flat and impermeable surfaces.
- The coupling between the flows in adjacent layers via viscous shear stresses, heat transfer, pressure forces, and electromagnetic effects were included into the model.
- The quasi-static approximation was used to evaluate the electric current perturbations induced by the flow velocity and the Lorentz forces resulting from the interaction of these currents with the base magnetic field.

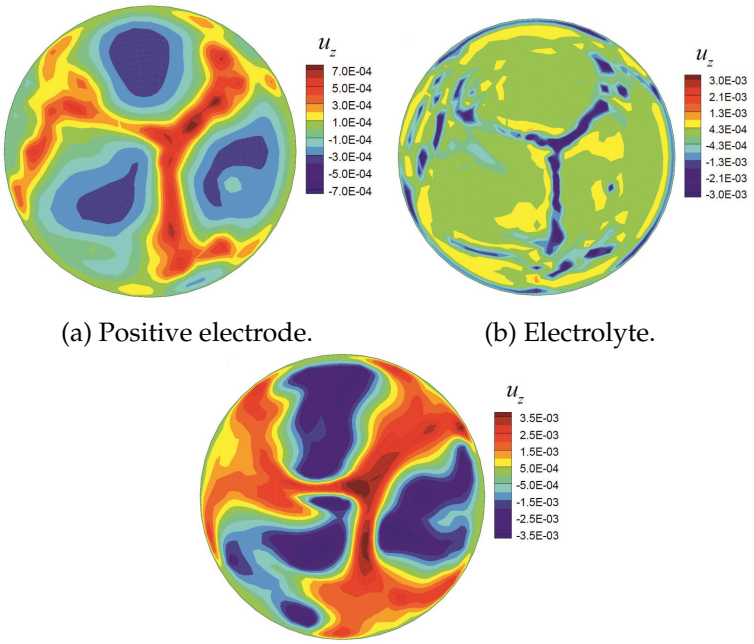

(a) Positive electrode. (b) Electrolyte.

(c) Negative electrode.

FIGURE 3.4: Spatial structure of developed finite-amplitude convection flow [25].

- The Boussinesq approximation is applied to describe the convection effects accounting for effects due to the internal Joule heating by the imposed current.

The main conclusion of the analysis presented in [25] is that thermal convection is unavoidable in LMBs. It was found that for the case of present commercial batteries the effect of the flow on the operation of the battery is weak. No reorientation of the Benard cells with magnetic field lines and formation of the anisotropic structures was clearly observed. The velocity in the bottom metal layer is insufficient for the strong mixing. In the case of thin electrolyte layer, the flow is the strongest in the top liquid metal and the weakest in the bottom metal layer (Figure 3.4). As it was suggested in [25] no significant deformation of the electrolyte-metal interfaces are to be expected. The obtained results, do not show clearly visible MHD effects. According to [25] these conclusions are only valid for small (a few cm in radius) batteries which were analysed in this study. However it is emphasised that the effect is expected to be much stronger in larger scale LMBs say, $R > 1.33$ m at the $j_0 \approx 10$ kA m^{-2}.

3.4 Tayler Instability (TI)

As described by Weber *et al.* [7] the Tayler Instability (TI) is a kink-type flow instability which occurs when the electric current through a conducting fluid exceeds a certain critical value. It was mainly analysed in the astrophysical context. It was suggested that the instability might be a limiting factor for the upward scalability of LMBs, see [9].

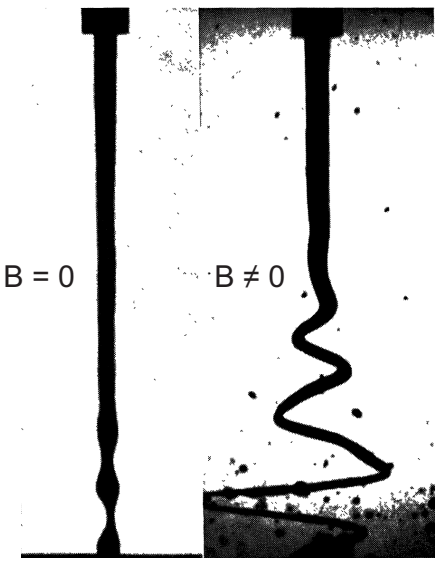

FIGURE 3.5: "Sausage" and "Spiral" instabilities with longitudinal magnetic field [26].

The interaction of an electrical current with its own magnetic field in a conducting fluid can create equilibrium states that are not always stable. For example, the electrical discharge in a plasma column can lead to the axisymmetric "sausage" or the non-axisymmetric "kink" instability. At the conductivity and viscosity values typical for plasmas, such instabilities are very common. For the case of a cylindrical z-pinch the kink instability can only be suppressed by applying an additional longitudinal magnetic field according to Kruskal-Shafranov condition [27]. Things are different for liquid metals, longitudinal magnetic field in some cases may even amplify the instability [26] (see Figure 3.5). However for the bounded systems high values of resistivity and viscosity play a stabilizing role. For the case of a homogeneous current in a cylindrical liquid metal column, the instability onset is governed by the ratio of magnetic to viscous forces, characterised by the square of the Hartmann number $\sim Ha^2$, which is defined as

$$Ha = B_\theta(r) r \left(\frac{\sigma}{\rho\nu}\right)^{1/2}. \tag{3.6}$$

Beyond a critical value of $Ha \simeq 20$, see [28], a non-axisymmetric flow pattern will be induced in the fluid. Recently the kink-type instability was observed in a experiment with liquid metal [29]. This instability, which needs a certain critical current to overcome the stabilizing effect of resistivity and viscosity, is referred to as the Tayler instability.

The TI may also be relevant for the LMBs. Estimates based on the physical properties of typical liquid metals show that the instability can occur in moderately sized batteries ($R = 25$ cm with $j_0 = 10$ kA m^{-2} [25]). As it was suggested in [31], the TI can be shifted to higher Ha values if the design of the battery is modified. For example, introducing backwards directed current in the centre, or applying an external axial magnetic field [9].

FIGURE 3.6: Schematic representation of the problem considered in [7, 30].

As it was found in the recent analysis [32], even when the instability occurs in moderately sized batteries, the kinetic energy of the induced flow is insufficient to disbalance the stable stratification of the three-layer system. According to [32] for realistic batteries the TI becomes dangerous at $R \sim 1.5$ m or even higher.

3.4.1 Numerical model results related to TI

Weber *et al.* [7] analysed the influence of the axial electrical boundary conditions on the characteristic features of the Tayler instability as well as on the occurrence of electro-vortex flows. Impact of feeding line above of the upper, and below of the lower current collector was discussed. The following assumptions were made

- The cylindrical cell is considered. The one single metal column (upper metal electrode) is analysed (Figure 3.6).
- Physical properties of the metal are assumed constant.
- The diameter of the wires is assumed to be half of that of the current collectors.
- The current is purely vertical and uniform only in the feeding line sufficiently far away from the current collectors.
- The quasi-static approximation is used to evaluate the electric current perturbations induced in the system.

Case when the applied current corresponds to $Ha = 250$ was analysed. It was found that as the current enters the current collector, it spreads radially over the

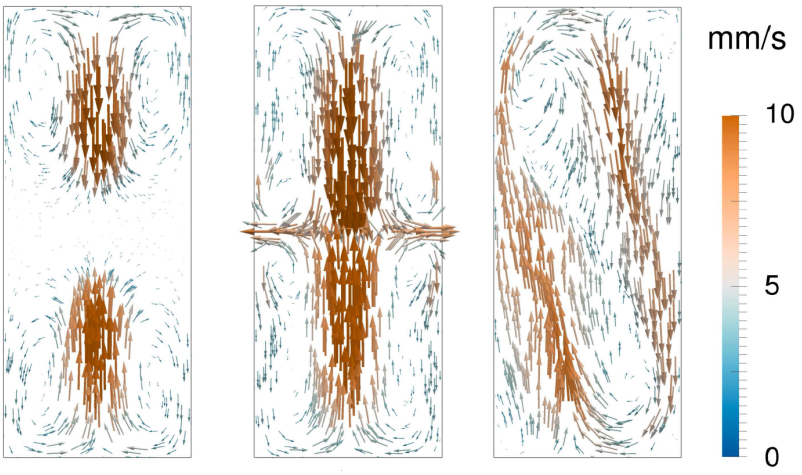

FIGURE 3.7: Temporal development of EVF in a cylindrical container [7].

whole diameter. The resulting force is rotational. This leads to the generation of the electro vortex flow [23]. There is no threshold current for the onset of EVF compared to the TI. The EVF starts as soon as the current is applied, however it takes time for the flow to develop through the whole volume (see Figure 3.7). As observed in [7] the initial flow structure is always axisymmetric, but, after some time, the EVF becomes unstructured. It was concluded that the transition depends on the applied current, on the aspect ratio and conductivity of current collectors and liquid metal.

3.5 Pinch-type instability at the rigid edge of a semi-infinite planar sheet carrying a uniform tangential electric current

Priede [33] analysed numerically a pinch-type instability in a semi-infinite planar sheet of an inviscid incompressible liquid with a straight rigid edge carrying a uniform tangential electric current. The electromagnetic pinch force is produced from the interaction of the electric current with its own magnetic and is balanced by the pressure gradient in quiescent liquid. It was found that this equilibrium state is unstable to the flow perturbation caused by a row of counter-rotating vortices along the edge. The compression and dispersion of the current lines where the flow is directed towards the edge occurs as a weaker magnetic field is advected by the flow towards

the edge and a stronger field is carried away. The interaction of the current perturbation with the base magnetic field results a pinch force that amplifies initial flow perturbation. This part of the pinch force dominates over the competing one which results from the interaction of the magnetic flux perturbation with the base current if an ideally conducting liquid is considered. It is shown in [33] that this instability is caused by the curvature of the magnetic field. The corresponding growth rate is defined by the linear current density and independent of the system size. As it was concluded in [33] that this instability might affect future LMBs with the size of a few metres and corresponding Hartmann number $Ha \approx 60$.

3.6 Shallow water approximation

Liquid layer can be classified as shallow if its depth h is much smaller than the characteristic horizontal length L, so that $\delta = h/L \ll 1$. Due to shallowness the horizontal velocity distribution over a vertical can be considered uniform. This allows reduction of a three-dimensional flow to a plane flow by integrating the horizontal velocity over a vertical in order to obtain a depth-averaged value [34]:

$$U_i = h^{-1} \int_{H_0}^{H_1} u_i(x, y, z) dz. \tag{3.7}$$

If the layer contains free surface, its elevation varies gradually with a small curvature compared with gravitational acceleration. This equals to the assumption that a hydrostatic (linear) pressure distribution over the depth is sufficient in regions of continuous flow. This approximation is not applicable if system contains steep bed slopes or discontinuities, for example hydraulic jumps. These cases are out of scope of this Thesis. The continuity equation (2.3) in the shallow water approximation accounting for the interfacial variations can be rewritten as

$$\partial_t h + \partial_i (U_i h) = 0, \tag{3.8}$$

Whereas the momentum equation (2.2) for horizontal depth averaged velocity components writes as follows

$$\partial_t U_i + U_j \partial_j U_i = -\rho^{-1} \partial_i p - g \partial_i h - k_f U_i + F_i. \tag{3.9}$$

The equation (3.9) accounts for the interfacial variations and for the turbulent dissipation at the solid bottom described by a linear in velocity friction law with the coefficient k_f as well as includes generalised depth averaged volume forces $\boldsymbol{F}$ (Coriolis force, inertial force, tidal force, electromagnetic force etc. [34]).

3.6.1 Boussinesq approximation

The Boussinesq approximation is based on the elimination of the dependency on vertical coordinate from the horizontal velocity components, while retaining vertical coordinate dependency in the varying layer thickness [35]. This approximation permits asymptotic expansion of the horizontal and vertical velocity components:

$$u_i = u_{0i}(x, y, t) + \delta u_{1i}(x, y, z, t) + O(\delta^2), \tag{3.10}$$

$$u_3 = \delta u_{13}(x, y, z, t) + O(\delta^2). \tag{3.11}$$

The Boussinesq formulation allows to generalise problem for non-unidirectionally propagating waves, accounting for side walls and several fluid layers [36]. Combining shallow water and Boussinesq approximations together allows to derive weakly non-linear wave equation to describe interfacial motion. This methodology proves to be sufficient to describe onset of electromagnetically driven unstable interfacial motion between aluminium and cryolite in Hall-Heroult Cells [37]. In this Thesis this methodology will be extended for three density stratified electrically conductive liquid layers.

3.7 Long wave interfacial instability

3.7.1 Theory for Hall-Heroult Cells (HHC)

LMBs are thought to be easily scalable on the cell level due to their simple construction using the natural density stratification of the liquid layers. Large cells of several

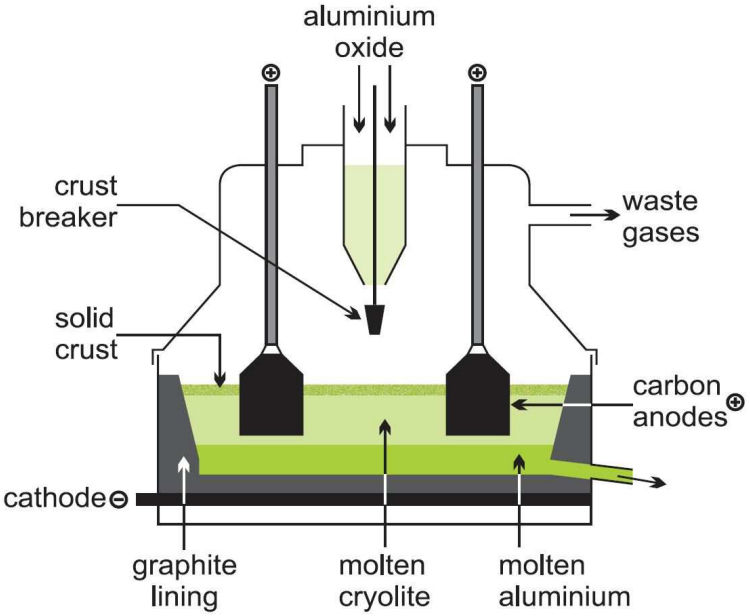

FIGURE 3.8: Principle scheme of HHC.
http://www.essentialchemicalindustry.org/metals/aluminium

cubic meters total volume have a potential to operate at very high power value [38]. High current densities coupled to the magnetic field (created by the currents in the cell, the supply bars and the neighbour cells) will lead to significant electromagnetic forces. Such forces in stratified liquid layers with large surface areas may cause a long wave interfacial instability as it is well known in the case of Hall-Heroult cells (HHC), see Figure 3.8, as first described by [39].

In a typical HHC the electric current, of total magnitude $150 - 800$ kA, enters the cell from the carbon anodes, passes through the liquid electrolyte and aluminium layer, and exits via the carbon cathode blocks at the bottom of the cell. The liquid layers are relatively shallow, $4 - 30$ cm in depth vs $4 - 20$ m in horizontal dimension. The small depth of the layers and the small difference of the liquid densities facilitates the instability development.

The ratio of electrical conductivities of the cell materials is another significant parameter. The liquid metal is a better conductor ($\sim 10^6$ S/m) than the carbon ($\sim 10^4$ S/m), while the electrolyte is about two orders of magnitude less conductive ($\sim 10^2$ S/m). The significantly higher resistivity of the electrolyte means that this layer is responsible for the majority of electrical losses in the cell. Joule heating is necessary to heat the cell and to keep the metal liquid, however the total voltage drop must be as low as possible in order to achieve a better electrical efficiency. A

small perturbation of the interface between liquid layers may cause a substantial redistribution of the current in the cell.

First attempts to explain the interfacial instabilities were made by [39–42]. A more involved understanding of the physical mechanism was provided by [5, 43, 44]. The mechanism is based on the standing gravity wave modification due to the electric current redistribution. The electric current density in the electrolyte increases above the wave crests, resulting in a high density horizontal current in the shallow liquid metal layer. In the presence of a vertical magnetic field the electromagnetic force excites another standing wave mode. The new wave mode is coupled to the original mode, and the oscillation frequency is shifted towards it. The frequency shift increases with the rise of the magnetic field until at a critical value the two wave frequencies coincide. An exponential growth of the amplitude indicates the onset of instability. In general, the above process is described by the following set of equations:

$$\partial_{tt}\widehat{\zeta}_k + \omega_k^2 \widehat{\zeta}_k = E G_{kk'} \widehat{\zeta}_{k'}, \tag{3.12}$$

where $\widehat{\zeta}_k$ is a vector which represents the amplitudes of the original gravitational modes $\boldsymbol{k} = (k_x, k_y)$, ω_k^2 is the matrix of the gravitational frequencies, $G_{kk'}$ is the interaction matrix, E is the dimensionless parameter characterizing the electromagnetic forces. The mode coupling is included in $G_{kk'}$, where each column represents the Lorentz force (Fourier decomposed) in response to the gravitational wave modes. These coupled equations represent an eigenvalue problem for the square of the new complex frequencies μ ($\widehat{\zeta}_k \sim e^{\mu t}$). The matrix $G_{kk'}$ is real anti-symmetric, and in a general case the eigenvalues are shifted increasing the magnetic field [5]. Onset of the instability starts at a critical value of E at which the exponentially growing part of the complex eigenvalue μ appears. A key point noted in [5, 43, 44], is that the dominant contribution to the perturbed Lorentz force arises from the interaction between a horizontal current in the aluminium layer and the vertical component of the background magnetic field. In general case, the interfacial motion in cells with odd aspect ratio (including cylindrical shape) is expected to become unstable [5, 43].

More realistic fluid dynamic description can be achieved starting from the full

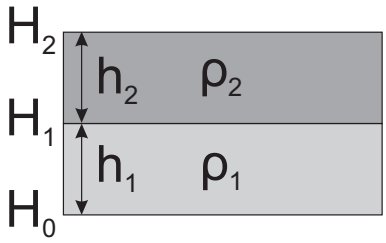

FIGURE 3.9: Schematic representation of the HHC.

set of Navier-Stokes equations by means of the shallow water and Boussinesq approximation following a systematic derivation of a set of coupled wave equations governing the three fluid layers. The hydrodynamic coupling is achieved by pressure continuity at the common interfaces. The continuity of the electric potential and the supplied electric current will introduce the electromagnetical coupling of waves. HHC can be characterized by the set of the following equations:

The **interfacial dynamics** between the aluminium and the electrolyte layer is described by

$$\alpha_1 \partial_{tt}\zeta_1 + k_{fe1}\partial_t\zeta_1 = R_1\partial_{jj}\zeta_1 + \partial_i(F_{i2} - F_{i1}) + \varepsilon[\rho_1\partial_j(U_{k1}\partial_k U_{j1}) - \rho_2\partial_j(U_{k2}\partial_k U_{j2})], \tag{3.13}$$

where

$$\alpha_1 = \frac{\rho_1}{h_1} + \frac{\rho_2}{h_2}, \quad k_{fe1} = \frac{\rho_1 k_{f1}}{h_1} + \frac{\rho_2 k_{f2}}{h_2}, \quad R_1 = (\rho_1 - \rho_2)g, \tag{3.14}$$

where ρ_m and h_m are the layer densities and unperturbed thicknesses, $k_{f,m}$ stands for a empirical coefficient that accounts friction generated by the turbulence in the shallow fluid layers ($m = 1, 2$ stands for layer number) [45, 46]. $\varepsilon = \max A/h \ll 1$ is a small parameter where A is a typical wave amplitude and h is a typical depth, $F_{i,m}$ and $U_{k,m}$ are the depth averaged Lorentz force and velocity fields (see Figure 3.9).

Equation (3.13) contains only the leading order velocities which are defined by a depth-averaged Navier-Stokes equation:

$$\partial_t U_{im} + \varepsilon U_{jm}\partial_j U_{im} = -\varepsilon^{-1}\rho_m^{-1}\partial_i p_p - g\partial_i\zeta_1 - k_{fm}U_{im} + F_{im}. \tag{3.15}$$

Linear form of the (3.15) is

$$\partial_t U_{im} = -\varepsilon^{-1}\rho_m^{-1}\partial_i p_p - k_{fm}\partial_{jj}U_{im} + F_{im}. \tag{3.16}$$

In [36] it was found that (3.16) is sufficient for the HHC description. Velocity components can be expressed in the following form [36, 47] :

$$U_{xm} = \partial_x \chi_m - \partial_y \psi_m, \tag{3.17}$$

$$U_{ym} = \partial_y \chi_m + \partial_x \psi_m, \tag{3.18}$$

where χ_m stands for the velocity potential and ψ_m stands for the stream function. The potential flow field represents the interfacial wave motion:

$$-\frac{1}{h_1}\partial_t \zeta_1 = \partial_{ii}\chi_1. \tag{3.19}$$

Vortical part of the flow field is defined by the rotational part of Lorentz forces. Both flow types can be considered separately in the linear approximation. This can be done by means of the substitution of (3.17) and (3.18) into (3.16) and application of the curl: $\boldsymbol{\nabla}\times$ this leads to

$$\partial_{tjj}\psi_m = -k_{f,m}\partial_{jjjj}\psi_m + (\boldsymbol{\nabla} \times F_{mi})_z. \tag{3.20}$$

Crucial role in the interfacial stability of the HHC plays the **electric current** in the aluminium layer which is defined by the perturbed electric potential:

$$\boldsymbol{j}_1 = -\sigma_1 \left(\partial_x \Phi_1, \partial_y \Phi_1, \frac{j_0}{\sigma_1} + (H_0 - z)\partial_{ii}\Phi_1 \right), \tag{3.21}$$

where σ_1 stands for the electric conductivity. The equation that defines perturbed electric potential distribution is

$$h_1 h_2 \partial_{ii}\Phi_1 - \sigma_{e,1}\Phi_1 = -\frac{j_0}{\sigma_1}\zeta_1, \tag{3.22}$$

where

$$\sigma_{e,1} = \frac{\sigma_2}{\sigma_1}\left[1 + \frac{\sigma_1}{\sigma_3}\frac{h_1}{h_3}\right]. \tag{3.23}$$

If the electric current distribution in the system is known the corresponding **magnetic field distribution** can be determined by the Biot-Savart law (2.12).

3.7.2 Extension to 3-layer modelling

Davidson & Lindsay [44] derived a simple mechanical analogue which captures the basic features of the metal pad instability in the HHC. The liquid aluminium layer is represented by a compound pendulum that consists of a large flat aluminium plate attached to a top surface by a light, rigid strut. The strut is pivoted at its top end so that the plate is free to swing along two horizontal axes x and y. The fluid system of infinite motion freedom is reduced to only two degrees of freedom. Zikanov [48] constructed the mechanical model for instability description in the LMB taking into account an additional top liquid metal layer. The metal layers of the battery are represented by solid metal slabs rigidly attached to weightless rigid struts pivoted at the top. The free oscillations of the slabs imitate the sloshing motion of the liquid layers. The slabs are separated from each other by a layer of a poorly conducting electrolyte. Two destabilization mechanisms were considered: 1) interaction of a purely vertical magnetic field and horizontal currents, similar to HHC, 2) interaction between the current perturbations and the azimuthal self-magnetic field from the total vertical current. The first mechanism will occur in real batteries if a sufficiently strong vertical magnetic field is present (typically $j_0 = 1$ A m^{-2}, $B_z = 3$ mT, $L_x \times L_y = 1.6$ m$\times 0.4$ m, $h_2 = 4.5$ mm). The batteries of a square or a circular horizontal cross section will be always unstable if even a small field is present. The second mechanism appears to be more challenging since the azimuthal magnetic field, unlike the vertical magnetic field, cannot be reduced via optimization of the current supply lines (unless they cross the liquid layer [9]). The existence of the second instability type was predicted by [49] for HHC case, yet needs more clarification for the LMB case. It is predicted to appear at $j_0 = 10$ kA m^{-2}, $R = 0.36$ m, $h_2 = 5$ mm. The approach developed by [44] and [48] is purely mechanical. However, the principal physical mechanism could be valid, due to the fact that sloshing motions generated in the shallow liquid layers

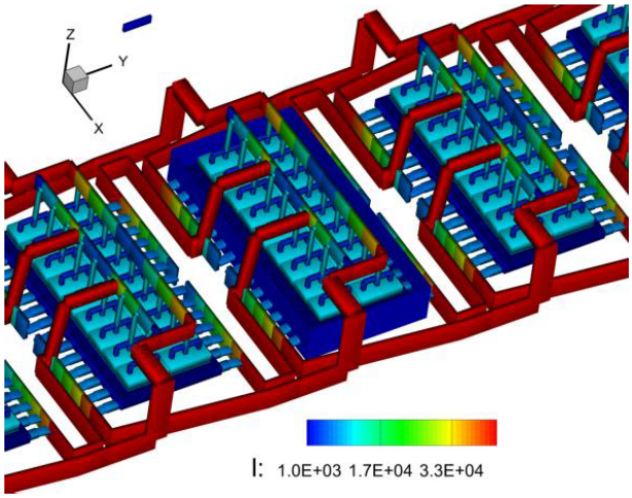

FIGURE 3.10: Busbar configuration for Trimet cell [37].

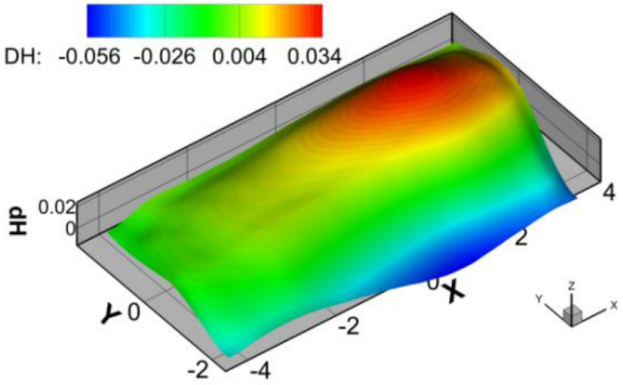

FIGURE 3.11: Metal interface just befor the short circuiting after the anode change [37].

are inherently large scale, and so their qualitative behaviour can be approximately described using the coupled pair of long wave modes approach.

3.8 Fully coupled models

3.8.1 HHC modelling

Industrial aluminium production cells are very well optimised for magnetic field and electric current distribution to avoid MHD instabilities in order to increase the current efficiency and to maintain a stable process of electrolysis. Bojarevics & Evans [37] applied a non-linear dynamically coupled mathematical model and the software based on the full MHD shallow water equations to the Trimet commercial electrolysis cell (see Figure 3.10) [50, 51]. This model is capable of computing time-dependent

currents, voltages, magnetic fields, bath-metal interface shape and turbulent magnetically driven flow in the bath and liquid metal. The bus bar temperatures are controlled and adjusted according to the computed Joule heating losses to the air. The electric current in the anodes is computed at all times following the development of the wave on the interface between liquid layers. Impact of the dome shaped time-averaged deformation of the metal surface (Figure 3.11) on the anode bottom burn-out process is accounted in the model. The electric current distribution in the liquid layers is computed from all the bus bar network connected to the anodes and cathode collectors, coupled with the cell interior details like the ledge profile, bottom shape, collector connections, electrolyte channels and the electrochemical voltage drop. The magnetic field is recomputed at all times. The detailed representation of the cell steel elements adds non-linearity to the overall magnetic field properties. The model results were compared with the electric current distribution variation in time over the anodes obtained from the magnetic field measurements [37]. A good agreement was found between the numerical predictions and the measured results.

As it was discussed in the previous chapter, large scale LMBs are more efficient than a large number of small ones. The main objective of the Thesis is extension of the HHC concept to LMBs. In the Chapters 5 and 7 it will be shown that the described numerical model can be applied for the large scale LMB description.

3.8.2 LMB modelling

Weber *et al.* [52] used a three dimensional multiphase model for the simulation of a LMB. The three different phases of the system are modelled by means of the volume of fluid method [53]. Effects of the surface tension were accounted using a continuum surface force model [54]. The model assumptions are

- The cell is cylindrical.
- Electrical current of constant and uniform density flowing between the top and bottom walls. Magnetic field is defined as

$$\boldsymbol{B} = \boldsymbol{\nabla} \times \boldsymbol{A} + \boldsymbol{B}_\theta + \boldsymbol{B}_z \tag{3.24}$$

where $\boldsymbol{A}$ is vector potential to account magnetic field generated by the horizontal currents, $\boldsymbol{B}_\theta$ is the uniform azimuthal field generated by the current, $\boldsymbol{B}_z$ is the axial uniform magnetic field applied externally.

- The coupling between the flows in adjacent layers is accounted via viscous shear stresses, pressure forces, and the electromagnetic effects.
- The thicknesses and physical properties of the three layers are assumed constant.
- The quasi-static approximation is used to evaluate the electric current perturbations.

Influence of the cell current, magnetic field, unperturbed upper metal and the electrolyte layer thickness as well as impact of density difference and electric conductivity ratio (upper metal vs molten salt) was analysed. If not being the variable quantity, the following values were used: $I = 78.5$ A, $B_z = 10$ mT, $h_1 = h_3 = 4.5$ cm, $h_2 = 1$ cm for $D = 10$ cm.

As it was reported in [52] the increase of the cell electric current and/or the magnetic field are leading to the amplification of the instability. Up to $I = 30$ A there are no significant deformations observed on the interface between the electrolyte and the upper metal. The minimal electrolyte thickness starts to decrease with the current increase. At 170 A contact of both metal electrodes (short-circuit) is observed. Variation of the background magnetic field gives very similar result (see Figure 3.12). The lower metal interface remains very stable for all considered electric current ($I \leq 250$ A) and magnetic field ($B_z \leq 25$ mT) values.

It was observed that for the shallow electrode and electrolyte cases the system is more unstable. The short-circuit is reached very similarly to the previous study cases.

It was found that the minimal critical salt layer thickness depends on the density difference between the liquid salt and the top metal. The system remains stable when $\triangle\rho \geq 515$ kg m^{-3}. The cell fails suddenly below $\Delta\rho = 60$ kg m^{-3}. The density gap between bottom metal and electrolyte was kept constant and very high. Decrease of the electric conductivity ratio (σ_2/σ_3) leads only to the one noticeable

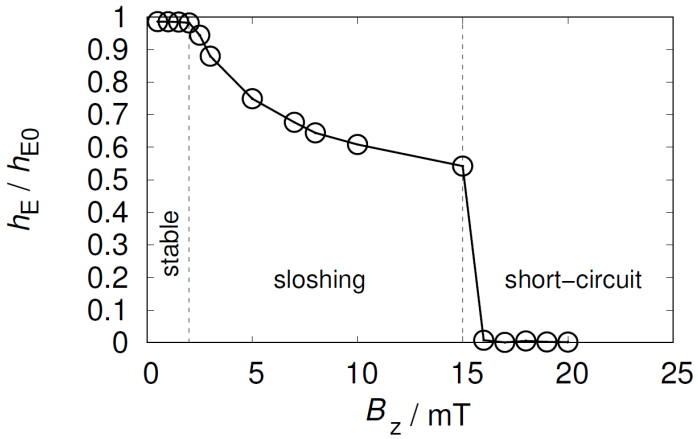

FIGURE 3.12: Minimal relative height of the salt layer depending on the vertical magnetic background field [52].

transition point, when interfacial deformation occurs, while dynamics remains very stable. As it was concluded in [52] the instability onset is well characterised by the criteria derived in [5, 39].

As it will be shown in the Chapter 6, the observed effects can be described by means of shallow water approximation.

3.8.3 Summary

This chapter provided a summary of the related research conducted by other authors. The main conclusions of this review are the following

- Electro-vortex flows are inevitable in LMBs and overall they are beneficial for the battery operation due to improved mass transfer.
- Effects related to thermal convection, Tayler and pinch-type instabilities are expected to be small within the parameter range typical to LMBs.
- The analogy between HHC and LMB allows to consider the battery as aluminium reduction cell, but filled with three liquid layers.
- There are models for HHC that are highly developed and can be used to model LMBs, allowing developments in this Thesis.

Chapter 4

3D electric current distribution in the battery

4.1 Overview

This chapter explores the implementation of the 3D numerical model applicable for a steady-state and time dependent electric current in a LMB. The numerical algorithm is derived and verified. The impact of different electric current collector arrangements is analysed. Three representative cases are considered: the first case is for the current flow in the battery with symmetrically arranged collectors, the second and the third cases are for the non-symmetric collector arrangement: non-optimized (the single collector cell) and optimized (the multiple collector cell).

4.2 Numerical model for electric current flow prediction in 3D

The 3D electric current distribution is required to describe the Lorentz force in the system which eventually will define LMB stability limit. The LMB cells with more uniform electric current distribution are expected to be more stable [38, 55]. In this chapter 3D numerical model is derived and the impact of the current collector arrangement on the electric current flow in the cell is estimated.

The system under consideration is illustrated in the Figure 4.1. In this figure the process of the constant supply of current of discharge is shown. Current is supplied into the battery through the upper electric current collector (Collector 2) and

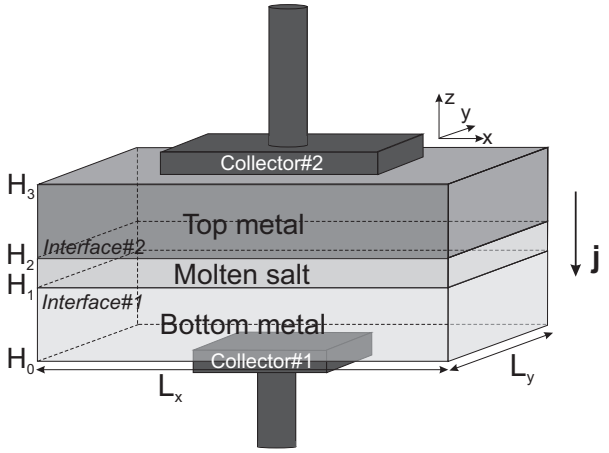

FIGURE 4.1: Schematic diagram of the LMB discharge for the analysis of collector arrangement impact on the distribution of electric current.

collected at the bottom collector (Collector 1). In this analysis metal interfaces are considered undeformable and flat; fluid flow induced currents are neglected (low magnetic Reynolds number approximation) [44, 56]:

$$Rm = \mu_0 \sigma U h = 4\pi \cdot 10^{-7} N/A^2 \cdot 3.65 \cdot 10^6 S/m \cdot 0.01 m/s \cdot 0.1 m \approx 0.004. \tag{4.1}$$

This result indicates that the assumption of the $Rm \ll 1$ is quite reasonable. The 3D numerical solution is constructed to evaluate the effect of the collector arrangement on the current flow in the system. The current flow is described with a set of the coupled Laplace equations for the electric potential:

$$\nabla^2 \varphi_i = 0, \tag{4.2}$$

where $i = 1, 2, 3$ stands for the layer number. The continuity conditions for the electric potential and the normal current component at the interfaces $z = H_m$ $(m = 1, 2)$ are

$$\varphi_m = \varphi_{m+1}, \tag{4.3}$$

$$\sigma_{m+1} \partial_n \varphi_{m+1} = \sigma_m \partial_n \varphi_m. \tag{4.4}$$

The normal derivative at the flat interfaces are defined as:

$$\partial_n \varphi_i = \boldsymbol{n} \cdot \boldsymbol{\nabla} \varphi_i = \partial_z \varphi_i. \tag{4.5}$$

Side walls of the domain are considered to be electrically insulating:

$$(\partial_n \varphi_i)_{x=0,L_x;y=0,L_y} = 0. \tag{4.6}$$

Current distributions on the Collectors 1 and 2 are defined as:

$$(j)_{z=H_0} = -j_1(x,y), \tag{4.7}$$

$$(j)_{z=H_3} = -j_3(x,y). \tag{4.8}$$

The set of the coupled Laplace equations (4.2) with the corresponding boundary conditions (4.3), (4.4), (4.7) and (4.8) can be rewritten in a weak form by means of integrating the equations on the horizontal interface Γ against a regular function q

$$\int_\Gamma (\partial_{zz} \varphi_i) q d\sigma + \int_\Gamma (\boldsymbol{\nabla} \varphi_i, \boldsymbol{\nabla} q) d\sigma = 0, \tag{4.9}$$

where $d\sigma = dxdy$ and the integration is over Γ, similar strategy was applied for the two layer problem based on shallow water approximation in [5]. Solution can be constructed in a Sobolev space $H^1(\Gamma)$, so that φ_i must satisfy the corresponding equations for all test-functions q that belong to $H^1(\Gamma)$. The following set of functions is introduced:

$$\Lambda = \left\{ \frac{2}{\sqrt{L_x L_y}} \epsilon_k \cos(k_x x) \cos(k_y y); k_x = \frac{m\pi}{L_x}, k_y = \frac{n\pi}{L_y}; m,n \in N \right\}, \tag{4.10}$$

$$\epsilon_k = \begin{cases} 1 & \text{if } k_x, k_y \neq 0, \\ 1/\sqrt{2} & \text{if } k_x \text{ or } k_y = 0, k_x \neq k_y, \\ 1/2 & \text{if } k_x = k_y = 0. \end{cases}$$

The elements of Λ form orthogonal basis in $H^1(\Gamma)$. A solution form that satisfies both (4.9) and corresponding boundary conditions (4.3)-(4.8) can be expressed in the

following way:

$$\varphi_i(x,y,z) = \sum_{\boldsymbol{k}} Z_{i,\boldsymbol{k}}(z) \frac{2}{\sqrt{L_x L_y}} \epsilon_{\boldsymbol{k}} \cos(k_x x) \cos(k_y y), \tag{4.11}$$

where $i = 1,2,3$. Taking into account the orthogonality properties of the cosine functions there can be obtained the set of the equations for the $Z_i(z)$ variable

$$\partial_{zz} Z_{i,\boldsymbol{k}} - \boldsymbol{k}^2 Z_{i,\boldsymbol{k}} = 0. \tag{4.12}$$

Solution of (4.12) can be represented by means of Chebyshev polynomials [11, 57, 58]:

$$Z(z) = \sum_{n=0}^{N} a_n T_n(z), \tag{4.13}$$

where $T_n(z)$ stands for Chebyshev polynomials of the first kind. The expansion (4.13) is valid only in the interval $z \in [-1,1]$. This condition requires a coordinate transformation:

$$\widehat{z}_i = \frac{2(z - H_i)}{H_i - H_{i-1}} + 1. \tag{4.14}$$

The resulting spectral problem (4.12) with corresponding boundary conditions can be rewritten:

$$\left(\frac{d\widehat{z}_1}{dz}\right)^2 \frac{d^2 Z_i}{d\widehat{z}_i^2} - \boldsymbol{k}^2 Z_i = 0. \tag{4.15}$$

For the case when $\boldsymbol{k} = (0,0)$ fixed potential conditions are used

$$Z_3(\widehat{z}_3 = 1) = \varphi_3, \tag{4.16}$$

$$Z_2(\widehat{z}_2 = 1) = Z_3(\widehat{z}_3 = -1) = \varphi_2, \tag{4.17}$$

$$Z_1(\widehat{z}_1 = 1) = Z_2(\widehat{z}_2 = -1) = \varphi_1, \tag{4.18}$$

$$Z_1(\widehat{z}_1 = -1) = \varphi_0, \tag{4.19}$$

where potential value on each domain of interest is defined as

$$\varphi_i = \frac{Ih_i}{\sigma_i L_x L_y} + \varphi_{i-1}, \tag{4.20}$$

where $h_i = H_i - H_{i-1}$ is the layer thickness and I corresponds to the total current. For all other $\boldsymbol{k} \neq \mathbf{0}$ cases:

$$\left(\frac{d\widehat{z}_3}{dz}\right) \frac{dZ_3}{d\widehat{z}_3}(\widehat{z}_3 = 1) = \alpha_3, \tag{4.21}$$

$$Z_3(\widehat{z}_3 = -1) = Z_2(\widehat{z}_2 = 1), \tag{4.22}$$

$$\sigma_3 \left(\frac{d\widehat{z}_3}{dz}\right) \frac{dZ_3}{d\widehat{z}_3}(\widehat{z}_3 = -1) = \sigma_2 \left(\frac{d\widehat{z}_2}{dz}\right) \frac{dZ_2}{d\widehat{z}_2}(\widehat{z}_2 = 1), \tag{4.23}$$

$$Z_2(\widehat{z}_2 = -1) = Z_1(\widehat{z}_1 = 1), \tag{4.24}$$

$$\sigma_2 \left(\frac{d\widehat{z}_2}{dz}\right) \frac{dZ_2}{d\widehat{z}_2}(\widehat{z}_2 = -1) = \sigma_1 \left(\frac{d\widehat{z}_1}{dz}\right) \frac{dZ_1}{d\widehat{z}_1}(\widehat{z}_1 = 1), \tag{4.25}$$

$$\left(\frac{d\widehat{z}_1}{dz}\right) \frac{dZ_1}{d\widehat{z}_1}(\widehat{z}_1 = -1) = \alpha_1, \tag{4.26}$$

where α_1 and α_3 are the electric current distribution Fourier expansion coefficients:

$$\begin{pmatrix} \alpha_1 \\ \alpha_3 \end{pmatrix} = \int_0^{\Gamma} \begin{pmatrix} j_1/\sigma_1 \\ j_3/\sigma_3 \end{pmatrix} \cos(k_x x) \cos\left(k_y y\right) d\sigma. \tag{4.27}$$

Using spectral tau methodology with Chebyshev-Lobatto nodes $x_n = \cos(n\pi/N)$, $n = 0, ..., N$ [57] the problem in the matrix representation is expressed as:

$$\mathcal{E} \frac{4}{h_i^2} \boldsymbol{a}^{(i)} - \mathcal{I} \boldsymbol{k}^2 \boldsymbol{a}^{(i)} = 0. \tag{4.28}$$

Corresponding set of the boundary conditions is expressed as:

$$\frac{r^2}{h_3} \cdot \widehat{I} \cdot \boldsymbol{a}^{(3)} = \alpha_3, \tag{4.29}$$

$$(-1)^r \cdot \mathcal{I} \cdot \boldsymbol{a}^{(3)} = \mathcal{I} \cdot \boldsymbol{a}^{(2)}, \tag{4.30}$$

$$\frac{(-1)^{r+1}}{h_3} \cdot r^2 \cdot \widehat{I} \cdot \boldsymbol{a}^{(3)} = \frac{q^2}{h_2} \cdot \widehat{I} \cdot \boldsymbol{a}^{(2)}, \tag{4.31}$$

$$(-1)^q \cdot \mathcal{I} \cdot \boldsymbol{a}^{(2)} = \mathcal{I} \cdot \boldsymbol{a}^{(1)}, \tag{4.32}$$

$$\frac{(-1)^{q+1}}{h_2} \cdot q^2 \cdot \widehat{I} \cdot \boldsymbol{a}^{(2)} = \frac{p^2}{h_1} \cdot \widehat{I} \cdot \boldsymbol{a}^{(1)}, \tag{4.33}$$

$$\frac{(-1)^{p+1}}{h_1} \cdot p^2 \cdot \widehat{I} \cdot \boldsymbol{a}^{(1)} = \alpha_1, \tag{4.34}$$

where $\{\boldsymbol{a}^{(1)} : p = 0, ..., P\}$, $\{\boldsymbol{a}^{(2)} : q = 0, ..., Q\}$ and $\{\boldsymbol{a}^{(3)} : r = 0, ..., R\}$, where P, Q and R represent the expansion terms for each of the layers defined by (4.13). For illustration purpose, the corresponding matrices and vectors in explicit form are:

$$\mathcal{E}^2 = \begin{pmatrix} 0 & 0 & 4 & 0 & 32 & 0 & 108 & 0 & \dots & \dots \\ 0 & 0 & 0 & 24 & 0 & 120 & 0 & 336 & \ddots & \vdots \\ 0 & 0 & 0 & 0 & 48 & 0 & 192 & 0 & & \vdots \\ 0 & 0 & 0 & 0 & 0 & 80 & 0 & 280 & \ddots & \vdots \\ 0 & 0 & 0 & 0 & 0 & 0 & 120 & 0 & & \vdots \\ 0 & 0 & 0 & 0 & 0 & 0 & 0 & 168 & \ddots & \vdots \\ 0 & \dots & \dots & \dots & \dots & \dots & & & \ddots & 0 \\ 0 & \dots & \dots & \dots & \dots & \dots & & & \dots & 0 \end{pmatrix}, \tag{4.35}$$

$$\mathcal{I} = \begin{pmatrix} 1 & 0 & 0 & 0 & 0 & 0 & 0 & 0 & \dots & 0 \\ 0 & 1 & 0 & 0 & 0 & 0 & 0 & 0 & & 0 \\ 0 & 0 & 1 & 0 & 0 & 0 & 0 & 0 & & 0 \\ 0 & 0 & 0 & 1 & 0 & 0 & 0 & 0 & & 0 \\ 0 & 0 & 0 & 0 & 1 & 0 & 0 & 0 & & 0 \\ 0 & 0 & 0 & 0 & 0 & 1 & 0 & 0 & & 0 \\ 0 & \dots & \dots & \dots & & & \ddots & & \dots & 0 \\ 0 & \dots & \dots & \dots & \dots & & & \ddots & \dots & 0 \end{pmatrix}, \tag{4.36}$$

with boundary conditions represented as:

$$(-1)^{q+1} q^2 \widehat{I} = (0, 1, -4, 9, \dots), \tag{4.37}$$

$$q^2 \widehat{I} = (0, 1, 4, 9, \dots). \tag{4.38}$$

In case of $\boldsymbol{k} = (0, 0)$ for $\widehat{z} = -1$ and $\widehat{z} = 1$ correspondingly:

$$(-1)^q \widehat{I} = (1, -1, 1, -1, \dots), \tag{4.39}$$

$$\widehat{I} = (1, 1, 1, 1, \dots), \tag{4.40}$$

whereas

$$\boldsymbol{a}^{(i)} = \begin{pmatrix} a_0^{(i)} & a_1^{(i)} & a_2^{(i)} & a_3^{(i)} & \dots \end{pmatrix}^T. \tag{4.41}$$

The potential distribution is reconstructed with the help of (4.11) for each particular layer:

$$Z_{\boldsymbol{k},1}(z) = \sum_{p=0}^{P} a_p^{(1)} T_p(z), \tag{4.42}$$

$$Z_{\boldsymbol{k},2}(z) = \sum_{q=0}^{Q} a_q^{(2)} T_q(z), \tag{4.43}$$

$$Z_{k,3}(z) = \sum_{r=0}^{R} a_r^{(3)} T_r(z). \tag{4.44}$$

In the numerical examples $P = Q = R = 60$ collocation points and $(N, M) = (87, 31)$ for Fourier modes were found to be sufficient if comparing to simulations with reduced values. The problem was solved using subroutines DGETRF (factorization) and DGETRS (solution) from the linear algebra software library LAPACK. The advantage of the chosen numerical strategy based on the spectral methodology compared to the 3D finite volume based solvers is high accuracy, no numerical diffusion of the free interfaces and significantly reduced computational times [11, 59].

4.3 Model results

Using the previously described numerical strategy for the 3D electric current flow description in the layered structure, the LMB case of Mg|$MgCl_2$-KCl-NaCl|Sb is presented. The electrical conductivity values are $\sigma_1 = 3.3 \cdot 10^6$ S m^{-1}, $\sigma_2 = 250$ S m^{-1}, $\sigma_3 = 3.65 \cdot 10^6$ S m^{-1}, with the bath geometry: $L_x^{bath} \times L_y^{bath} = 8$ m $\times 3.6$ m and the layer thicknesses: $h_{1,3} = 0.2$ m, $h_2 = 0.05$ m; the total current is kept constant $I = 100$ kA for all considered cases.

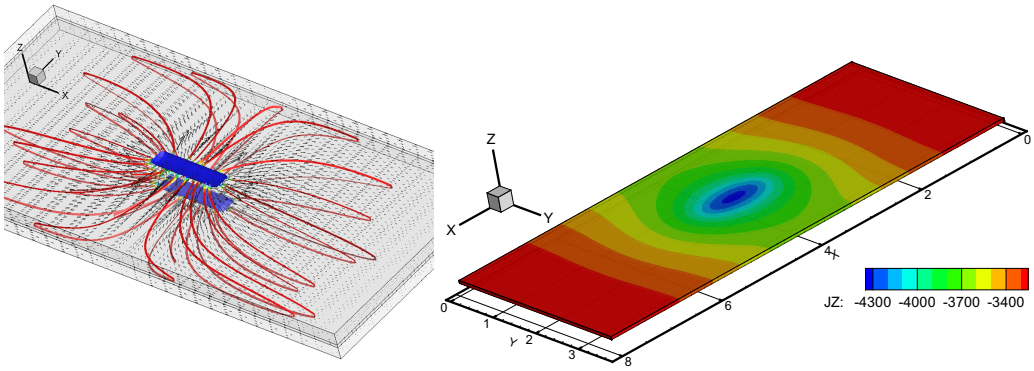

(a) (j_x, j_y, j_z) (b) j_z distribution in the electrolyte layer

FIGURE 4.2: The electric current distribution in the cell with symmetrically arranged collectors.

For the first case, as an illustrative example, analysed with the symmetric electric current collector arrangement. The considered collector dimensions are $L_x^{col12} \times L_y^{col12} = 1.3$ m $\times 0.3$ m. Both collectors are centred and symmetrically positioned against each other. The results are presented in the Figure 4.2. The computed 3D

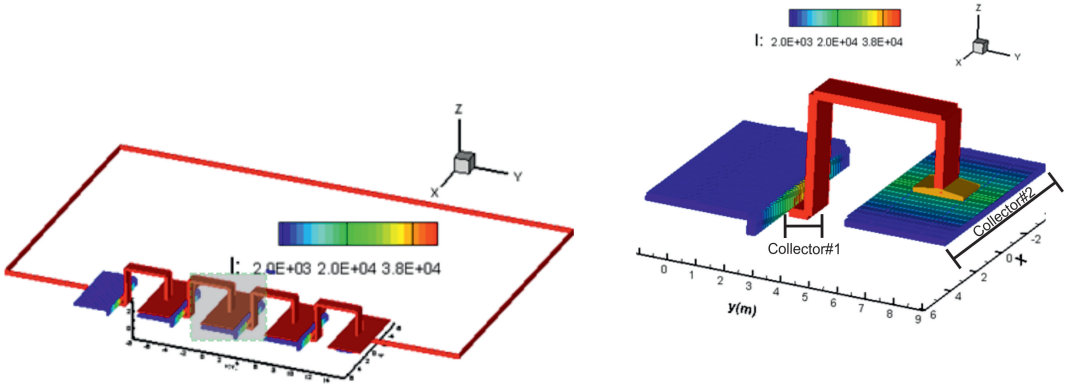

FIGURE 4.3: Schematic representation of the non-optimized collector cell.

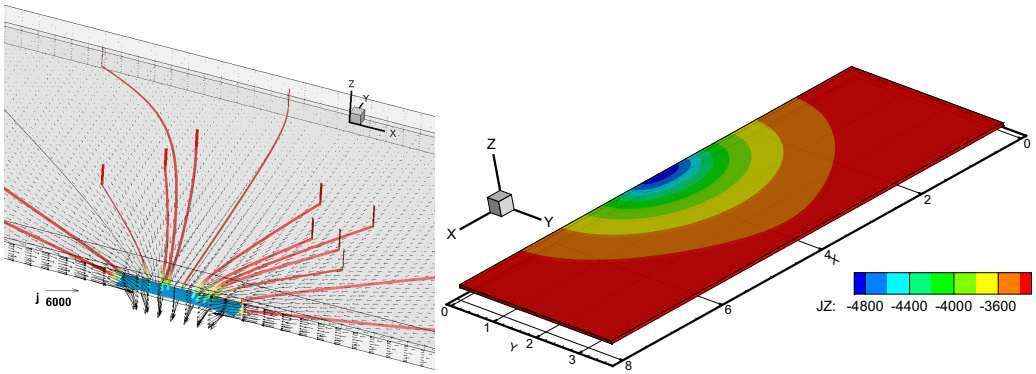

(a) (j_x, j_y, j_z) (b) j_z distribution in the electrolyte layer

FIGURE 4.4: The electric current distribution in the non-optimized collector cell.

electric current flow, see Figure 4.2 (a), pattern demonstrates the presence of high horizontal current density in the metallic electrode layers. Current distribution in the metal electrodes is qualitatively the same. In the electrolyte layer due to the significantly lower electrical conductivity value the electric current is almost purely vertical. The major potential drop is observed in the electrolyte layer ($\approx$ 0.7 V) if compared to the metal layers ($\approx$ 0.0005 V). Figure 4.2 (b) shows the j_z current component distribution in the electrolyte layer. As it can be seen, the distribution is non-uniform and the largest magnitudes are concentrated around the collector locations. This result suggests that the current flow in both metals is correlated.

For the two following cases non-symmetrical collector arrangements are analysed. The first case is for a non-optimized cell (the single collector cell) having collectors $L_x^{col1} \times L_y^{col1} = 1.3$ m$\times$0.3 m and $L_x^{col2} \times L_y^{col2} = L_x^{bath} \times L_y^{bath}$. The collector at the bottom is shifted to one of the long side walls, while the top one is across the

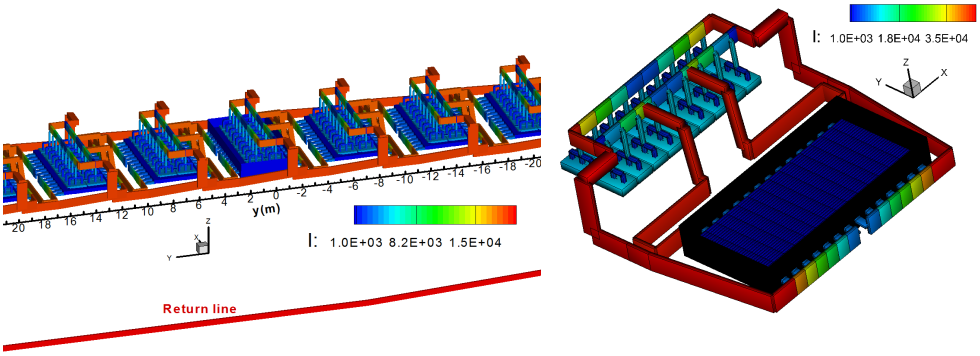

FIGURE 4.5: Schematic representation of the optimized collector cell, and possible connections to neighbours.

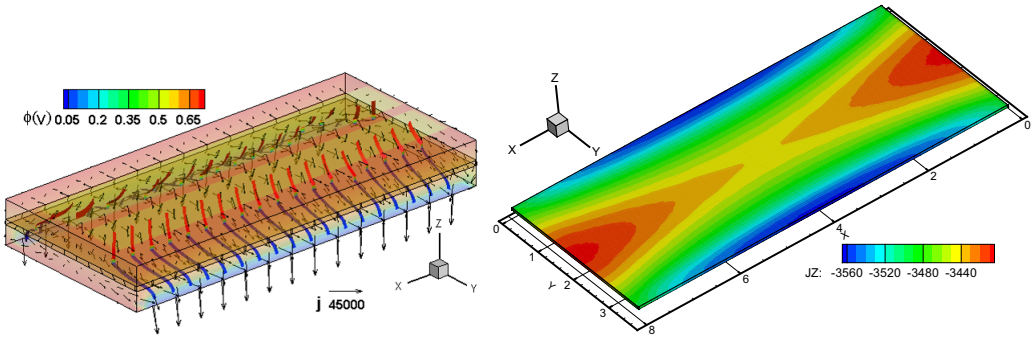

(a) (j_x, j_y, j_z) (b) j_z distribution in the electrolyte layer

FIGURE 4.6: The electric current distribution in the optimized collector cell.

whole upper metal surface (see Figure 4.3). The described geometry is chosen following the trend used in [2–4] for experimental LMBs. The obtained electric current distribution is shown in the Figure 4.4 (a). In this example the current passes almost vertically through the upper electrode and the electrolyte layer. After reaching the lower metal the current redistributes and flows towards the Collector 1. Figure 4.4 (b) shows the j_z current component distribution in the electrolyte layer. It can be seen that also in this case the distribution is non-uniform, with the largest magnitudes concentrated around the Collector 1 location.

In the second case of an optimized cell (the multiple collector cell) the collector geometries are $L_x^{col1} \times L_y^{col1} = 7.6$ m$\times$0.3 m (at bottom side position) and $L_x^{col2} \times L_y^{col2} = 7.6$ m$\times$0.95 m (at the top central position, see Figure 4.5). There are two collectors at the bottom, both are located near the long side walls and start 0.2 m from the corners. At the top there are two current collectors separated from each other by

a 0.3 m gap and starting at 0.2 and 0.7 m from the respective side walls. This particular cell configuration is used for the commercial aluminium reduction cells at Trimet. The current supply bus-bar path is optimized in such a way that the magnetic field is reduced in magnitude and its distribution optimized to avoid the MHD wave instability (see Figure 7.1). The obtained electric current distributions are shown in the Figure 4.6 (a). After entering through Collector 2 the current redistributes in the upper metal electrode. In the electrolyte layer, where the main potential drop is observed the current flows purely vertically. After reaching the lower metal the current redistributes and flows towards Collector 1. Horizontal current components are more pronounced in the lower metal electrode compared to upper one. Figure 4.6 (b) shows j_z current component distribution in the electrolyte layer. Similarly to the previous examples, the current distribution is non-uniform. It is concentrated around the Collector 1 location. The current distribution in the considered examples, Figures 4.2 (b), 4.4 (b) and 4.6 (b), are significantly different. The electric current distribution in the electrolyte layer for the optimized collector arrangement is much more uniform when compared to the symmetric and the non-optimized one. The difference suggests that the horizontal currents in the cell with optimized collector configuration may play less pronounced role. This result hints on the significantly different interfacial stability thresholds between the non-optimized and the optimized cell. This will be discussed in more detail in the Chapter 7.

The examples provided give valuable information to estimate the effect of the various current collector topologies on the current distribution in the LMB with arbitrary geometry. Overall, it is expected that instantaneous variations in electrolyte thickness will be more important than current collector arrangement for the interfacial stability, similarly to HHC. One of the future objectives is an extension of the approach described in this chapter to account for the interfacial variations. Another objective would be a comparison of the 3D model with the shallow water model, and the estimation of the applicability limits for the last one.

Chapter 5

Shallow water approximation

5.1 Overview

In this chapter the mathematical model based on shallow water and Boussinesq approximations is derived. In this approximation the full 3D problem is reduced to a 2D space. The first step in the derivation introduces the small depth and amplitude expansion set of the coupled Navier-Stokes equations, followed by the reduction to the set of equations for coupled waves. In the second step the same strategy is applied for the 3D coupled Laplace equations to describe the electric current which is reduced to a 2D set. In the third step the non-linear interaction with the velocity field is added to the hydrodynamic model. In this analysis it is assumed that each current collector is covering the whole corresponding metal surface.

5.2 Interfacial dynamics

This chapter is devoted to practically realizable LMBs with high aspect ratios. As shown in the literature analysis (see Chapter 3) the shallow water approximation is very suitable for MHD process description in these cells.

The hydrodynamics of the three density stratified electrically conductive liquid layer system, schematically represented in Figure 5.1 in the presence of electromagnetic fields, is described by the following equations

$$\rho\partial_t u_i + \rho u_j \partial_j u_i = -\partial_i(p + \rho g z) + \partial_j \rho\nu(\partial_j u_i + \partial_i u_j) + f_i, \tag{5.1}$$

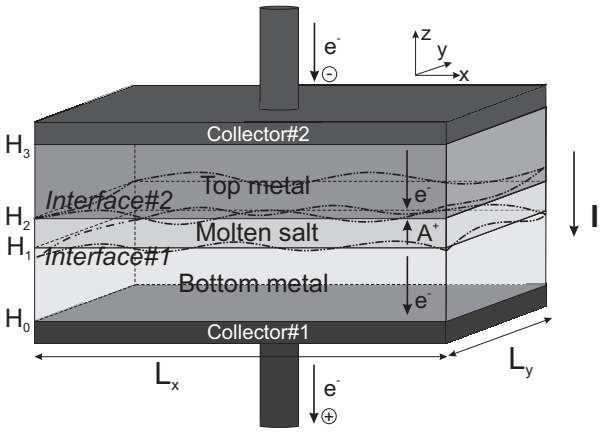

FIGURE 5.1: Schematic diagram of the LMB discharge for the analysis of interfacial wave stability.

$$\partial_i u_i = 0, \tag{5.2}$$

where the indices $i, j = 1, 2, 3$ correspond to the coordinates (x, y, z), the velocity components are given as (u_1, u_2, u_3), the summation over repeated indices is implied. In this analysis the horizontal dimensions of the cell are assumed to be much larger compared to the vertical depth, so that the description can be based on a systematically derived shallow water approximation. Additionally Boussinesq approximation is employed according to which the velocity components in each layer can be represented as an expansion in a small aspect ratio parameter $\delta = \max h / \min L$, where h is a typical depth, for instance the unperturbed metal layer and L is the characteristic horizontal dimension (width of the cell):

$$u_i = u_{0i}(x, y, t) + \delta u_{1i}(x, y, \overline{z}, t) + O(\delta^2), \qquad i = 1, 2, \tag{5.3}$$

$$u_3 = \delta u_{13}(x, y, \overline{z}, t) + O(\delta^2), \tag{5.4}$$

where a stretched vertical coordinate $\overline{z} = z/\delta$ is introduced. The u_3 expansion starts with the δ-order due to (5.2). If all three components of the electromagnetic force density are of the same order of magnitude: $f_x \sim f_y \sim f_z$, and the horizontal pressure gradient components are of the same order as the corresponding force components: $\partial_i p \approx f_i$, then the vertical component of the gradient $\partial_3 p \sim -\rho g \gg f_z$. According to these estimates, the leading horizontal $(i = 1, 2)$ components of (5.1)

are

$$\rho\partial_t u_{0i} + \rho u_{0j}\partial_j u_{0i} = -\partial_i p + \delta^{-1}\partial_{\bar{z}}\rho\nu\partial_{\bar{z}}(u_{0i} + \delta u_{1i}) + f_i. \tag{5.5}$$

The vertical component of the equation (5.1) gives the leading order terms as:

$$-\delta^{-1}\partial_{\bar{z}}(p + \rho g\delta\bar{z}) + f_z = 0. \tag{5.6}$$

The hydrostatic pressure in the liquid layers adjacent to the interface $H_1(x, y, t)$, see the Figure 5.1, can be expressed by

$$p_m^{(1)}(x, y, z, t) = p_p^{(1)}(x, y, t) - \rho_m g(z - H_1) + \delta\int_{H_1(x,y,t)}^{z} f_{zm}dz, \tag{5.7}$$

where the index $m = 1, 2$ stands for the layer number and $p_p^{(1)}$ is the reference pressure at the moving interface $z = H_1(x, y, t)$. Similarly the same pressure can be referenced to the interface $H_2(x, y, t)$, the corresponding pressure given by

$$p_n^{(2)}(x, y, z, t) = p_p^{(2)}(x, y, t) - \rho_n g(z - H_2) + \delta\int_{H_2(x,y,t)}^{z} f_{zn}dz, \tag{5.8}$$

where in this particular case $n = 2, 3$. The respective horizontal gradients of the pressure required in the horizontal momentum equation (5.5) are:

$$\partial_i p_m^{(1)} = \partial_i p_p^{(1)} + \rho_m g\partial_i H_1 + \delta\left[\int_{H_1}^{z}\partial_i f_z dz - f_z(H_1)\partial_i H_1\right], \tag{5.9}$$

$$\partial_i p_n^{(2)} = \partial_i p_p^{(2)} + \rho_n g\partial_i H_2 + \delta\left[\int_{H_2}^{z}\partial_i f_z dz - f_z(H_2)\partial_i H_2\right]. \tag{5.10}$$

The next step is to introduce the depth averaging within each layer. The depth averaging for horizontal velocity components is performed in the following way:

$$U_{ik} = h_k^{-1}\int_{H_{k-1}}^{H_k} u_{ik}(x, y, z)dz, \tag{5.11}$$

where $k = 1, 2, 3$ is the layer number (no summation over k) and $h_k(x, y, t) = H_k - H_{k-1}$ is the local variable depth, see Figure 5.1. The depth averaging can be applied to the continuity equation (5.2):

$$h_k^{-1}\int_{H_{k-1}}^{H_k}(\partial_i u_i+\partial_3 u_3)dz = h_k^{-1}[\partial_i\int_{H_{k-1}}^{H_k}u_i dz - u_i(H_k)\partial_i H_k + u_i(H_{k-1})\partial_i H_{k-1} + u_3(H_k) - u_3(H_{k-1})] = 0, \quad (5.12)$$

where $i = 1, 2$. The vertical velocity u_3 at the $z = H_k(x, y, t)$ is given by the kinematic condition, stating that the interface moves with the local velocity:

$$u_3(H_k) = \partial_t H_k + u_i(H_k)\partial_i H_k. \quad (5.13)$$

Substituting (5.13) into (5.12) leads to

$$\partial_t h_k + \partial_i(U_{ik}h_k) = 0. \quad (5.14)$$

The last equation can be linearised if an additional approximation of a small wave amplitude is introduced: $h_k(x, y, t) = h_{0k} + \varepsilon h'_k(x, y, t)$ for the layer thickness or equivalently $H_m(x, y, t) = H_{0m} + \varepsilon\zeta_m(x, y, t)$ for the interface position, where the additional small parameter $\varepsilon = \max A/h$ is introduced. A is a typical wave amplitude and h_{0k}, H_{0m} are the unperturbed values, ζ_m are the interfacial perturbations. For each particular layer the depth average horizontal velocity divergence can be expressed as:

$$\partial_i U_{i1} = -\frac{\varepsilon}{h_{01}}[\partial_t\zeta_1 + \partial_i(U_{i1}\zeta_1)], \quad (5.15)$$

$$\partial_i U_{i2} = -\frac{\varepsilon}{h_{02}}\{\partial_t(\zeta_2 - \zeta_1) + \partial_i[U_{i2}(\zeta_2 - \zeta_1)]\}, \quad (5.16)$$

$$\partial_i U_{i3} = \frac{\varepsilon}{h_{03}}[\partial_t\zeta_2 + \partial_i(U_{i3}\zeta_2)]. \quad (5.17)$$

The fixed top and bottom condition requires:

$$h_1 + h_2 + h_3 = H_3 - H_0. \quad (5.18)$$

In order to estimate the leading order of terms in the depth averaged momentum equations (5.5) dimensionless variables of order $O(1)$ are introduced using the following scaling: L for the coordinates x, y; h for a typical layer thickness; $\varepsilon\sqrt{gh}$ - for the wave velocity; $L/\sqrt{gh}$ - for the time; $\rho_k g h$ for the pressure ($k = 1, 2, 3$). For typical geometries considered in this analysis $\delta = h/L \approx 0.2\text{m}/8\text{m} = 0.0250 \ll 1$, whereas, $\varepsilon = A/h \approx 0.005\text{m}/0.2\text{m} = 0.0250 \ll 1$.

The horizontal pressure gradient from the expressions (5.9) and (5.10), neglecting terms of the δ and higher order, can be substituted in the depth averaged, nondimensionalized horizontal momentum equation (5.5). For the layers adjacent to the lower interface $H_1(x, y, t)$ the respective momentum equations are

$$\partial_t U_{i1} + \varepsilon U_{j1}\partial_j U_{i1} = -\varepsilon^{-1}\rho_1^{-1}\partial_i p_p^{(1)} - g\partial_i\zeta_1 - k_{f1}U_{i1} + E_1 F_{i1}, \tag{5.19}$$

$$\partial_t U_{i2} + \varepsilon U_{j2}\partial_j U_{i2} = -\varepsilon^{-1}\rho_2^{-1}\partial_i p_p^{(1)} - g\partial_i\zeta_1 - k_{f2}U_{i2} + E_2 F_{i2}, \tag{5.20}$$

where the depth averaged force F_i is defined similarly to (5.11). For the upper interface $H_2(x, y, t)$ the respective equations are:

$$\partial_t U_{i2} + \varepsilon U_{j2}\partial_j U_{i2} = -\varepsilon^{-1}\rho_2^{-1}\partial_i p_p^{(2)} - g\partial_i\zeta_2 - k_{f2}U_{i2} + E_2 F_{i2}, \tag{5.21}$$

$$\partial_t U_{i3} + \varepsilon U_{j3}\partial_j U_{i3} = -\varepsilon^{-1}\rho_3^{-1}\partial_i p_p^{(2)} - g\partial_i\zeta_2 - k_{f3}U_{i3} + E_3 F_{i3}. \tag{5.22}$$

The equations (5.20) and (5.21) formally give the connection between the reference pressures $p_p^{(1)}$ and $p_p^{(2)}$ defined on the two interfaces, however they are valid in the same fluid layer $k = 2$. The alternative representations are required for the wave equation derivation. After the integration over depth the dissipative terms in (5.5) are replaced by empirical expressions used for the shallow water approximation [45, 46] using a linear in velocity friction law with the coefficients k_{fk}. The electromagnetic interaction parameter is introduced as $E_k = IB/(L^2\rho_k g\varepsilon\delta)$ [36]. The corresponding magnitude of E can be estimated, using typical values for $I = 10^5$ A, $B = 10^{-3}$ T, $L = 8$ m (width of cell), $\rho = 1.6 \cdot 10^3$ kg/m^3 (liquid magnesium for the top metal), $\varepsilon = \delta = 0.025$: $E = 0.32 = O(1)$. The electromagnetic term is of the same

order of magnitude as the leading terms, while the nonlinear wave motion terms are of lower order ($\sim \varepsilon$) and will be neglected later for the linear theory.

The wave equations for the coupled interfaces can be derived following the procedure described in [60]:

1. take time derivative of the non-dimensional linearised equations (5.15),(5.16):

$$\partial_{it} U_{i1} = -\frac{\varepsilon}{h_{01}} \partial_{tt} \zeta_1, \tag{5.23}$$

$$\partial_{it} U_{i2} = -\frac{\varepsilon}{h_{02}} \partial_{tt} (\zeta_2 - \zeta_1), \tag{5.24}$$

2. substitute (5.23), (5.24) into the horizontal divergence of (5.19),(5.20)

3. take the difference of the resulting equations.

This procedure eliminates the common unknown pressure $p_p^{(1)}$ on the interface ζ_1:

$$\begin{aligned} &\alpha_1 \partial_{tt} \zeta_1 + k_{fe1} \partial_t \zeta_1 - \frac{\rho_2}{h_{02}} \partial_{tt} \zeta_2 - \frac{\rho_2 k_{f2}}{h_{02}} \partial_t \zeta_2 \\ &= R_1 \partial_{jj} \zeta_1 - \rho_1 E_1 \partial_i F_{i1} + \rho_2 E_2 \partial_i F_{i2} \\ &+ \varepsilon [\rho_1 \partial_j (U_{k1} \partial_k U_{j1}) - \rho_2 \partial_j (U_{k2} \partial_k U_{j2})]. \end{aligned} \tag{5.25}$$

The corresponding boundary conditions for the normal velocity $u_n = 0$ at the side walls can be obtained by taking the difference between (5.19) and (5.20) to eliminate the common pressure at the interface ζ_1:

$$\partial_n \zeta_1 = (\rho_1 E_1 F_{n1} - \rho_2 E_2 F_{n2}) / R_1. \tag{5.26}$$

In a similar manner the wave equation for the upper interface ζ_2 can be obtained:

$$\begin{aligned} &\alpha_2 \partial_{tt} \zeta_2 + k_{fe2} \partial_t \zeta_2 - \frac{\rho_2}{h_{02}} \partial_{tt} \zeta_1 - \frac{\rho_2 k_{f2}}{h_{02}} \partial_t \zeta_1 \\ &= R_2 \partial_{jj} \zeta_2 - \rho_2 E_2 \partial_i F_{i2} + \rho_3 E_3 \partial_i F_{i3} \\ &+ \varepsilon [\rho_2 \partial_j (U_{k2} \partial_k U_{j2}) - \rho_3 \partial_j (U_{k3} \partial_k U_{j3})], \end{aligned} \tag{5.27}$$

and the corresponding boundary conditions

$$\partial_n \zeta_2 = (\rho_2 E_2 F_{n2} - \rho_3 E_3 F_{n3})/R_2. \tag{5.28}$$

The new constants introduced in the above equations are defined as:

$$\alpha_1 = \frac{\rho_1}{h_{01}} + \frac{\rho_2}{h_{02}}, \quad \alpha_2 = \frac{\rho_2}{h_{02}} + \frac{\rho_3}{h_{03}}, \tag{5.29}$$

$$k_{fe1} = \frac{\rho_1 k_{f1}}{h_{01}} + \frac{\rho_2 k_{f2}}{h_{02}}, \quad k_{fe2} = \frac{\rho_3 k_{f3}}{h_{03}} + \frac{\rho_2 k_{f2}}{h_{02}}, \tag{5.30}$$

$$R_1 = (\rho_1 - \rho_2)g, \quad R_2 = (\rho_2 - \rho_3)g. \tag{5.31}$$

The newly derived set equations of (5.25)-(5.31) accounts for the previously unreported effects: electromagnetic forcing and dissipation effects in the three layer system. As it can be seen from (5.25) and (5.27), both interfaces can not be considered independently due to the presence of coupling terms. The non-linear terms represent the wave interaction with the velocity field. These terms are of ε order and are expected to have a smaller impact on interfacial dynamics if compared to electromagnetic forcing and the interfacial coupling. However in the presence of a relatively large electomagnetically induced rotational velocity in the liquid layers ($Re \approx 1000$ [51]), the non-linear terms can be retained in the numerical model (see Chapter 6 and 7). In the following it will be assumed that the interfacial drag k_{f2} is negligible in comparison to the top and bottom solid surface drag coefficients k_{f1} and k_{f3}. The set of the equations (5.25) and (5.27) in the electrically nonconductive limit, in the absence of viscous dissipation and if dispersive effects are neglected is in correspondence with the set of the equations obtained by [61] derived for the dynamics of internal solitary waves in stratified 3-layer ocean. The aluminium electrolysis cell MHD wave model can be recovered if $\zeta_2 = 0$ in (5.25).

5.3 Electric current distribution

For energy storage and supply the LMB must operate in two regimes: charge and discharge, resulting in the current flowing (upwards or downwards). In this research only the charging process is considered due to the physical symmetry of both operational regimes. The current flow in the layered structure is illustrated in Figure 5.1. In the low Rm approximation when the flow effect is neglected the electric current can be expressed as

$$j_k = -\sigma_k \nabla \varphi_k \tag{5.32}$$

and is described by a set of coupled Laplace equations for the electric potential $\varphi_k(x, y, z)$:

$$\partial_{ii}\varphi_k = 0, \tag{5.33}$$

where $k = 1, 2, 3$ corresponds to the layer number (see Chapter 4). The continuity conditions for the electric potential and the normal current component $\boldsymbol{j} \cdot \boldsymbol{n}$ at the interfaces $z = H_m$ $(m = 1, 2)$ are

$$\varphi_m = \varphi_{m+1}, \tag{5.34}$$

$$\sigma_{m+1}\partial_n\varphi_{m+1} = \sigma_m\partial_n\varphi_m. \tag{5.35}$$

The normal derivatives at the deformed interfaces are defined as (assuming the summation over the repeated index i only):

$$\partial_n\varphi_k = \boldsymbol{n} \cdot \nabla\varphi_k = \frac{\partial_z\varphi_k - \partial_i H_k \partial_i \varphi_k}{(1 + \partial_i H_k \partial_i H_k)^{1/2}}. \tag{5.36}$$

With (5.36) the current continuity (5.35) at the interfaces H_1 and H_2 can be written explicitly in the nondimensional form in order to estimate the leading order terms:

$$s_1\delta^2(\partial_{\bar{z}}\varphi_2 - \varepsilon\delta^2\partial_i\bar{\zeta}_1\partial_i\varphi_2) = \partial_{\bar{z}}\varphi_1 - \varepsilon\delta^2\partial_i\bar{\zeta}_1\partial_i\varphi_1, \tag{5.37}$$

$$\partial_{\overline{z}}\varphi_3 - \varepsilon\delta^2\partial_i\overline{\zeta}_2\partial_i\varphi_3 = s_3\delta^2(\partial_{\overline{z}}\varphi_2 - \varepsilon\delta^2\partial_i\overline{\zeta}_2\partial_i\varphi_2), \tag{5.38}$$

where the four orders of magnitude difference in the electrical conductivities permit to define $\sigma_2/\sigma_1 = s_1\delta^2$, $\sigma_2/\sigma_3 = s_3\delta^2$ and the stretched $\overline{\zeta}_i = \zeta_i/\delta$. These definitions allow to compare numerically the electrical conductivities in the poorly conducting electrolyte relative to the well conducting liquid metals, and the effect of the small depth ($\sim \delta$) of the layers. The side walls of the domain are considered to be electrically insulating:

$$(\partial_n\varphi_k)_{x=0,L_x;y=0,L_y} = 0. \tag{5.39}$$

In this analysis it is assumed without reducing the generality, that the applied current distributions at the top and the bottom are uniform and equal:

$$(j)_{\overline{z}=\overline{H}_0} = (j)_{\overline{z}=\overline{H}_3} = -j_0. \tag{5.40}$$

In principle, $j(x, y, t)$ could be used, however requiring an external circuit solution.

The set of Laplace equations (5.33) can be rewritten in a nondimensional form

$$\delta^2\partial_{ii}\varphi_k + \partial_{\overline{z}\overline{z}}\varphi_k = 0. \tag{5.41}$$

The shallow water approximation requires that the potential is expanded in terms of the parameter δ:

$$\varphi_k(x, y, \overline{z}, t) = \varphi_{0k} + \delta\varphi_{1k} + \delta^2\varphi_{2k} + O(\delta^3), \tag{5.42}$$

where the expansion terms are expressed in a similar manner as in [5]:

$$\varphi_{0k} = (a_k + \varepsilon A_k)\overline{z} + (b_k + \varepsilon B_k), \tag{5.43}$$

$$\varphi_{1k} = (c_k + \varepsilon C_k)\overline{z} + (d_k + \varepsilon D_k), \tag{5.44}$$

$$\varphi_{2k} = (e_k + \varepsilon E_k)\overline{z} + (g_k + \varepsilon G_k) - \frac{1}{6}\overline{z}^3\partial_{ii}(a_k + \varepsilon A_k) - \frac{1}{2}\overline{z}^2\partial_{ii}(b_k + \varepsilon B_k), \tag{5.45}$$

where a, b, c, d, e, g are the coordinate x and y dependent functions that correspond to the unperturbed interfaces. The functions A, B, C, D, E, G are x, y and time t dependent, corresponding the perturbed interfaces. Taking into account the previously described boundary conditions and neglecting the higher order terms, the following coefficient equalities can be obtained at the lower metal interface $\overline{z} = \overline{H}_1$:

$$a_1 = A_1 = 0, \tag{5.46}$$

$$c_1 = C_1 = 0, \tag{5.47}$$

$$s_1 a_2 = e_1, \tag{5.48}$$

$$s_1 A_2 = E_1 - \overline{H}_{01}\partial_{ii}B_1, \tag{5.49}$$

$$a_2\overline{H}_{01} + b_2 = b_1, \tag{5.50}$$

$$A_2\overline{H}_{01} + a_2\overline{\zeta}_1 + B_2 = B_1. \tag{5.51}$$

Similarly, at the upper metal interface $\overline{z} = \overline{H}_2$:

$$a_3 = A_3 = 0, \tag{5.52}$$

$$c_3 = C_3 = 0, \tag{5.53}$$

$$s_3 a_2 = e_3, \tag{5.54}$$

$$s_3 A_2 = E_3 - \overline{H}_{02}\partial_{ii}B_3, \tag{5.55}$$

$$a_2\overline{H}_{02} + b_2 = b_3, \tag{5.56}$$

$$A_2\overline{H}_{02} + a_2\overline{\zeta}_2 + B_2 = B_3. \tag{5.57}$$

At the bottom and top current collectors, $\overline{z} = \overline{H}_0, \overline{H}_3$:

$$\overline{j}_3 = \frac{j_0}{\delta\sigma_3} = e_3, \tag{5.58}$$

$$0 = E_3 - \overline{H}_3\partial_{ii}B_3, \tag{5.59}$$

$$\overline{j}_1 = \frac{j_0}{\delta\sigma_1} = e_1, \tag{5.60}$$

$$0 = E_1 - \overline{H}_0\partial_{ii}B_1. \tag{5.61}$$

From (5.46)-(5.61) the unknown coefficients for unperturbed and perturbed parts can be expressed in terms of b_1, b_3 and B_1, B_3 respectively. Then combining (5.49), (5.55), (5.59) and (5.61) leads to the following expression:

$$-\frac{s_3}{s_1}(\overline{H}_{01} - \overline{H}_0)\partial_{ii}B_1 = (\overline{H}_3 - \overline{H}_{02})\partial_{ii}B_3, \tag{5.62}$$

which after integration is

$$-\frac{s_3}{s_1}(\overline{H}_{01} - \overline{H}_0)B_1 = (\overline{H}_3 - \overline{H}_{02})B_3 + C, \tag{5.63}$$

where C is a function of x and y, satisfying $\partial_{ii}C = 0$. From the boundary conditions it follows that on the vertical walls of the cell $\partial_n C = 0$, meaning that $C = const = 0$ due to the freedom to choose the arbitrary constant in the perturbed potential definition. Physically this means that the perturbed electric current is formed of closed

loops within the 3 liquid layers and the potentials are linearly correlated. By means of (5.49), (5.51), (5.55), (5.57) with (5.62) the governing set of the equations for the perturbed potentials $\Phi_1 = \varepsilon B_1$ and $\Phi_3 = \varepsilon B_3$ can be derived. For application in LMB the newly derived dimensional equations for the electric potential perturbations are linearly correlated to the respective interface perturbations:

$$h_{01}h_{02}\partial_{ii}\Phi_1 - \sigma_{e,1}\Phi_1 = \frac{j_0}{\sigma_1}(\zeta_2 - \zeta_1), \tag{5.64}$$

$$h_{02}h_{03}\partial_{ii}\Phi_3 - \sigma_{e,2}\Phi_3 = -\frac{j_0}{\sigma_3}(\zeta_2 - \zeta_1), \tag{5.65}$$

where

$$\sigma_{e,1} = \frac{\sigma_2}{\sigma_1}\left(1 + \frac{\sigma_1}{\sigma_3}\frac{h_{01}}{h_{03}}\right), \tag{5.66}$$

$$\sigma_{e,2} = \frac{\sigma_2}{\sigma_3}\left(1 + \frac{\sigma_3}{\sigma_1}\frac{h_{03}}{h_{01}}\right). \tag{5.67}$$

The current distribution in the electrolyte is almost purely vertical due to fact that $\sigma_2 \ll \sigma_1 \sim \sigma_3$. According to (5.64) and (5.65), the current flow is perturbed by the electrolyte thickness perturbations. Finally, the corresponding dimensional current components can be expressed as

$$\boldsymbol{j}_1 = -\sigma_1\left(\partial_x\Phi_1, \partial_y\Phi_1, \frac{j_0}{\sigma_1} + (H_0 - z)\partial_{ii}\Phi_1\right), \tag{5.68}$$

$$\boldsymbol{j}_2 = -\sigma_2\left(0, 0, \left(1 - \frac{h_2 - h_{02}}{h_{02}}\right)\frac{j_0}{\sigma_2} + \frac{\Phi_3 - \Phi_1}{h_{02}}\right), \tag{5.69}$$

$$\boldsymbol{j}_3 = -\sigma_3\left(\partial_x\Phi_3, \partial_y\Phi_3, \frac{j_0}{\sigma_3} + (H_3 - z)\partial_{ii}\Phi_3\right). \tag{5.70}$$

In the following chapter it will be shown that some of these perturbations may become electromagnetically coupled due to the presence of magnetic field and may lead to an instability resulting in a short circuit state at the extreme case.

5.4 Fluid dynamics

Similarly to the HHC case the fluid flow in shallow LMBs can be described by the linearised depth-averaged Navier-Stokes equation (3.16). The velocity components are expressed as the superposition of the potential and rotational combinations

$$U_{xk} = \partial_x \chi_k - \partial_y \psi_k, \tag{5.71}$$

$$U_{yk} = \partial_y \chi_k + \partial_x \psi_k, \tag{5.72}$$

where $k = 1, 2, 3$ represents the layer number. For the LMB case velocity potentials are defined by the linearised (5.15)-(5.17):

$$-\frac{1}{h_{01}} \partial_t \zeta_1 = \partial_{ii} \chi_1, \tag{5.73}$$

$$-\frac{1}{h_{02}} \partial_t (\zeta_2 - \zeta_1) = \partial_{ii} \chi_2, \tag{5.74}$$

$$\frac{1}{h_{03}} \partial_t \zeta_2 = \partial_{ii} \chi_3. \tag{5.75}$$

Similarly to the HHC the stream function is described by

$$\rho_k (\partial_{tjj} \psi_k + k_{fk} \partial_{jjjj} \psi_k) = -\partial_y F_{kx} + \partial_x F_{ky}. \tag{5.76}$$

The electromagnetic force components are defined as

$$F_{kx} = j_{ky} B_{kz} - j_{kz} B_{ky}, \tag{5.77}$$

$$F_{ky} = j_{kz} B_{kx} - j_{kx} B_{kz}. \tag{5.78}$$

Drag coefficient determination for the layered system

The following examples consider purely laminar wave mass flow, with typical Reynolds number $Re = UL/\nu = 10^{-3}\text{m/s} \cdot 10^{-2}\text{m}/10^{-6}\text{m}^2/\text{s} \approx 10$. The flow in 1D case can be

analysed analytically: $\boldsymbol{u}_k = (u_k, 0, 0)$ in the layered system ($k = 1, 2, 3$) with the forcing: $\boldsymbol{f}_k = (f_k, 0, 0)$, where $f_k = const$ and the index k stands for the layer number. The simplified 1D models will be derived in order to estimate the linear friction law in similarity to the Darcy law.

Single layer steady flow between two fixed parallel plates is characterised by the following equation:

$$\eta_1 \frac{d^2 u_1}{dz^2} = -f_1, \tag{5.79}$$

where η stands for dynamic viscosity. There are no-slip boundary conditions on the walls ($z = H_0, H_1$)

$$(u_1)_{z=H_0} = (u_1)_{z=H_1} = 0. \tag{5.80}$$

The following velocity distribution along z-axis is obtained

$$u_1(z) = -\frac{1}{2\eta} f_1 z(z - h_{01}). \tag{5.81}$$

After averaging over the depth (5.81) rewrites as:

$$U_1 = \frac{1}{h_1} \int_{H_0}^{H_1} u_1(z) dz = \frac{h_{01}^2}{12\eta_1} f_1. \tag{5.82}$$

The equivalent Darcy friction law is

$$-\alpha_1 U_1 + F_1 = 0 \Longrightarrow \alpha_1 = \frac{12\eta_1}{h_{01}^2}. \tag{5.83}$$

Steady flow with free surface above the solid bottom is described by the equation (5.79). In this case corresponding boundary conditions (assuming that free boundary is on the top) are:

$$(u_1)_{z=H_0} = \left(\frac{du_1}{dz}\right)_{z=H_1} = 0. \tag{5.84}$$

The velocity and its depth-averaged value are

$$u_1(z) = -\frac{f_1 z(z - 2h_{01})}{2\eta_1}, \tag{5.85}$$

$$U_1 = \frac{h_{01}^2}{3\eta_1} f_1. \tag{5.86}$$

For this case the Darcy friction law expresses as

$$-\alpha_1 U_1 + F_1 = 0 \Longrightarrow \alpha_1 = \frac{3\eta_1}{h_{01}^2}. \tag{5.87}$$

The last expression can be used for a multilayer system

$$\alpha_k = \frac{3\eta_k}{h_{0k}^2}. \tag{5.88}$$

Two layer steady flow between two fixed parallel plates for the case when the applied forcing is present in the lower layer is described by the set of the following equations

$$\eta_1 \frac{d^2 u_1}{dz^2} = -f_1, \tag{5.89}$$

$$\eta_2 \frac{d^2 u_2}{dz^2} = 0. \tag{5.90}$$

The boundary conditions are

$$(u_1)_{z=H_0} = (u_2)_{z=H_2} = 0, \tag{5.91}$$

$$(u_1)_{z=H_1} = (u_2)_{z=H_1}, \tag{5.92}$$

$$\left(\eta_1 \frac{du_1}{dz}\right)_{z=H_1} = \left(\eta_2 \frac{du_2}{dz}\right)_{z=H_1}. \tag{5.93}$$

The corresponding velocity distributions are

$$u_1(z) = -\frac{(\eta_2 h_{01} - h_{02}\eta_1)z^2 + (2h_{01}h_{02}\eta_1 + h_{01}^2\eta_2)z}{2\eta_1(\eta_1 h_{02} + \eta_2 h_{01})} f_1, \tag{5.94}$$

$$u_2(z) = \frac{(h_{01} + h_{02} - z)h_{01}^2}{2(\eta_1 h_{02} + \eta_2 h_{01})} f_1. \tag{5.95}$$

The depth averaged velocity for the lower layer is

$$U_1 = \frac{1}{h_1}\int_{H_0}^{H_1} u_1 dz = \frac{h_{01}^2(4\eta_1 h_{02} + \eta_2 h_{01})}{12\eta_1(\eta_1 h_{02} + \eta_2 h_{01})} f_1. \tag{5.96}$$

In this case the corresponding Darcy's law can be expressed as:

$$-(\alpha_1 + \alpha_{12,1})U_1 + F_1 = 0, \tag{5.97}$$

where $\alpha_{12,1}$ coefficient describes the friction of upper layer at the bounding plate due to the induced motion by the lower layer. It can be determined as follows

$$\alpha_{12,1} = \frac{F_1}{U_1} - \alpha_1 = \gamma_{12,1}\alpha_1, \tag{5.98}$$

$$\gamma_{12,1} = \frac{3}{4\frac{\eta_1}{\eta_2}\frac{h_{02}}{h_{01}} + 1}. \tag{5.99}$$

In a similar manner the case when $f_1 = 0$ and $f_2 \neq 0$ will describe forcing only in the upper layer. Applying the previously used derivation the friction coefficient for the lower layer due to the induced motion from the upper one results in:

$$\alpha_{21,2} = \gamma_{21,2}\alpha_2, \tag{5.100}$$

$$\gamma_{21,2} = \frac{3}{4\frac{\eta_2}{\eta_1}\frac{h_{01}}{h_{02}} + 1}. \tag{5.101}$$

In the general case when $f_1, f_2 \neq 0$, the forcing is present in both layers. For this case the total drag in the first layer will be a superposition of three components:

$$\alpha_1^{\text{2layers}} = \alpha_1 + \alpha_{12,1} + \alpha_{21,2}, \tag{5.102}$$

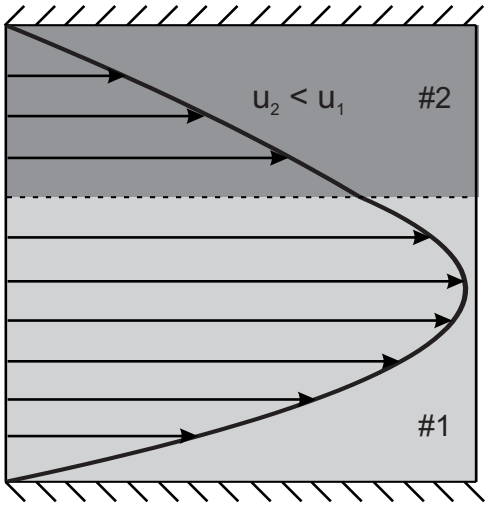

FIGURE 5.2: 1D velocity distribution in the 2-layer system response to differential forcing action $f_1 > f_2$.

or

$$\alpha_1^{2\text{layers}} = (1 + \gamma_{12,1})\alpha_1 + \gamma_{21,2}\alpha_2. \tag{5.103}$$

For the second layer the total drag expresses as

$$\alpha_2^{2\text{layers}} = \alpha_2 + \alpha_{21,1} + \alpha_{12,1}, \tag{5.104}$$

$$\alpha_2^{2\text{layers}} = (1 + \gamma_{21,2})\alpha_2 + \gamma_{12,1}\alpha_1. \tag{5.105}$$

An example of the velocity profile in the 2-layer system (HHC prototype) accounting for the friction is shown on the Figure 5.2. Due to the condition $f_1 > f_2$ the velocity in the lower layer is larger then in the upper one. Tangential stress continuity leads to continuous velocity change at the interface from parabolic to linear profile.

Two layer steady flow along single fixed plate For the case when the upper layer has a free surface the forcing set of equations will be the same as in the previously considered example, with $f_1 = 0$ and $f_2 \neq 0$. The corresponding boundary conditions are

$$(u_1)_{z=H_0} = \left(\frac{du_2}{dz}\right)_{z=H_2} = 0, \tag{5.106}$$

$$(u_1)_{z=H_1} = (u_2)_{z=H_1}, \tag{5.107}$$

$$\left(\eta_1 \frac{du_1}{dz}\right)_{z=H_1} = \left(\eta_2 \frac{du_2}{dz}\right)_{z=H_1}. \tag{5.108}$$

The velocities are:

$$u_1(z) = \frac{h_{02} z}{\eta_1} f_2, \tag{5.109}$$

$$u_2(z) = \frac{[2(h_{01}+h_{02})\eta_1 - z]z - (2h_{02}+h_{01})\eta_1 h_{01} + 2h_{01}h_{02}\eta_2}{2\eta_1\eta_2} f_2. \tag{5.110}$$

The averaged velocity expresses as

$$U_2 = \frac{h_{02}(\eta_1 h_{02} + 3\eta_2 h_{01})}{3\eta_1\eta_2} f_2. \tag{5.111}$$

From the Darcy equation as in all the previous cases the coefficient for the drag for the second layer due to the bottom layer friction at the bounding plate is

$$\alpha_{21,2} = \gamma_{21,2}\alpha_1, \tag{5.112}$$

where

$$\gamma_{21,2} = \frac{\eta_2 h_{01}^2}{h_{02}(\eta_1 h_{02} + 3\eta_2 h_{01})}. \tag{5.113}$$

For the case with the same forcing, but with a free surface at the bottom (three layer system prototype) the corresponding boundary conditions are

$$\left(\frac{du_2}{dz}\right)_{z=H_1} = (u_3)_{z=H_3} = 0, \tag{5.114}$$

$$(u_2)_{z=H_2} = (u_3)_{z=H_2}, \tag{5.115}$$

$$\left(\eta_2 \frac{du_2}{dz}\right)_{z=H_2} = \left(\eta_3 \frac{du_3}{dz}\right)_{z=H_2}. \tag{5.116}$$

The drag coefficient for this case are

$$\alpha_{23,2} = \gamma_{23,2}\alpha_2, \tag{5.117}$$

where

$$\gamma_{23,2} = \frac{\eta_2 h_{03}^2}{h_{02}(\eta_1 h_{02} + 3\eta_2 h_{01})}. \tag{5.118}$$

Three layer steady flow between two fixed parallel plates with forcing For the case when the forcing is applied only in one the system is characterised by the following set of equations:

$$\eta_1 \frac{d^2u_1}{dz^2} = -f_1, \tag{5.119}$$

$$\eta_2 \frac{d^2u_2}{dz^2} = 0, \tag{5.120}$$

$$\eta_3 \frac{d^2u_3}{dz^2} = 0, \tag{5.121}$$

with the boundary conditions

$$(u_1)_{z=H_0} = (u_3)_{z=H_3} = 0, \tag{5.122}$$

$$(u_1)_{z=H_1} = (u_2)_{z=H_1}, \tag{5.123}$$

$$(u_2)_{z=H_2} = (u_3)_{z=H_2}, \tag{5.124}$$

$$\left(\eta_1 \frac{du_1}{dz}\right)_{z=H_1} = \left(\eta_2 \frac{du_2}{dz}\right)_{z=H_1}, \tag{5.125}$$

$$\left(\eta_2 \frac{du_{2x}}{dz}\right)_{z=H_2} = \left(\eta_3 \frac{du_3}{dz}\right)_{z=H_2}. \tag{5.126}$$

The velocity distribution in this particular case is

$$u_1(z) = \frac{(\eta_1\eta_2 h_{03} + \eta_1\eta_3 h_{02} + \eta_2\eta_3 h_{01})z^2 - (2\eta_1\eta_2 h_{01}h_{03} + 2\eta_1\eta_3 h_{01}h_{02} + \eta_2\eta_3 h_{01}^2 h_{03})z}{2\eta_1(\eta_1\eta_2 h_{03} + \eta_1\eta_3 h_{02} + \eta_2\eta_3 h_{01})} f_1, \tag{5.127}$$

$$u_2(z) = \frac{\eta_3(h_{01} + h_{02} - z) + \eta_2 h_{03}}{2(\eta_1\eta_2 h_{03} + \eta_1\eta_3 h_{02} + \eta_2\eta_3 h_{01})} f_1 h_{01}^2 z, \tag{5.128}$$

$$u_3(z) = \frac{\eta_2(h_{01} + h_{02} + h_{03} - z)}{2(\eta_1\eta_2 h_{03} + \eta_1\eta_3 h_{02} + \eta_2\eta_3 h_{01})} f_1 h_{01}^2 z. \tag{5.129}$$

The averaged velocity for the 1st layer is

$$U_1 = \frac{1}{h_1}\int_{H_0}^{H_1} u_1 dz = \frac{h_{01}^2(4\eta_1\eta_2 h_{03} + 4\eta_1\eta_3 h_{02} + \eta_2\eta_3 h_{01})}{12\eta_1(\eta_1\eta_2 h_{03} + \eta_1\eta_3 h_{02} + \eta_2\eta_3 h_{01})} f_1. \tag{5.130}$$

The Darcy equation is

$$-(\alpha_1 + \alpha_{13,1})U_1 + F_1 = 0. \tag{5.131}$$

The drag coefficient in the 1st layer due to the 3 layer friction at the upper wall can be determined in a following way

$$\alpha_{13,1} = \frac{F_1}{U_1} - \alpha_1 = \gamma_{13,1}\alpha_1, \tag{5.132}$$

$$\gamma_{13,1} = \frac{3}{4\left(\frac{\eta_1}{\eta_3}\frac{h_{03}}{h_{01}} + \frac{\eta_1}{\eta_2}\frac{h_{02}}{h_{01}}\right) + 1}. \tag{5.133}$$

For the case when $f_2 \neq 0$ and $f_1 = f_3 = 0$ the corresponding drag will be the superposition of two drag components: upper/lower layer interaction with the middle layer:

$$\alpha_{21,2} + \alpha_{23,2}. \tag{5.134}$$

When $f_3 \neq 0$ and $f_1 = f_2 = 0$ the averaged velocity in upper layer is described by

$$U_3 = \frac{1}{h_3}\int_{H_2}^{H_3} u_3 dz = \frac{h_{03}^2(4\eta_2\eta_3 h_{01} + 4\eta_1\eta_3 h_{02} + \eta_1\eta_2 h_{03})}{12\eta_3(\eta_1\eta_2 h_{03} + \eta_1\eta_3 h_{02} + \eta_2\eta_3 h_{01})} f_3. \tag{5.135}$$

For this case the Darcy equation is

$$-(\alpha_3 + \alpha_{31,3})U_3 + F_3 = 0. \tag{5.136}$$

The friction coefficient of upper layer can be found in a following way

$$\alpha_{31,3} = \frac{U_3}{F_3} - \alpha_3 = \gamma_{31,3}\alpha_3, \tag{5.137}$$

$$\gamma_{31,3} = \frac{3}{4\left(\frac{\eta_3}{\eta_1}\frac{h_{01}}{h_{03}} + \frac{\eta_3}{\eta_2}\frac{h_{02}}{h_{03}}\right) + 1}. \tag{5.138}$$

In the general case when $f_1, f_2, f_3 \neq 0$ the corresponding total drag in the first layer will be a superposition of the four drag components:

$$\alpha_1^{\text{3layers}} = \alpha_1 + \alpha_{13,1} + \alpha_{21,2} + \alpha_{31,3}, \tag{5.139}$$

$$\alpha_1^{\text{3layers}} = (1 + \gamma_{13,1} + \gamma_{21,2})\alpha_1 + \alpha_{31,3}\alpha_3. \tag{5.140}$$

For the second layer it will be the superposition of the two:

$$\alpha_2^{\text{3layers}} = \alpha_{21,2} + \alpha_{23,2}, \tag{5.141}$$

$$\alpha_2^{\text{3layers}} = \gamma_{21,2}\alpha_1 + \gamma_{23,2}\alpha_3. \tag{5.142}$$

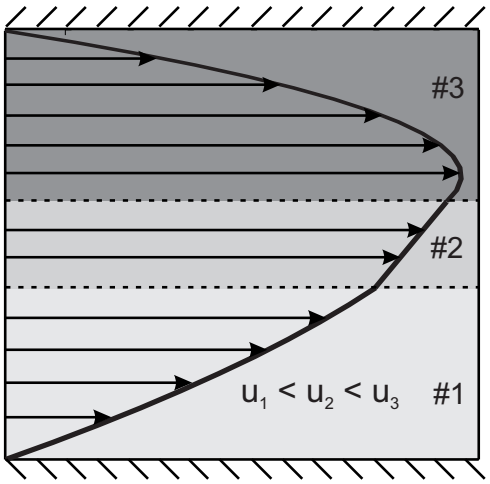

FIGURE 5.3: 1D velocity distribution in the 3-layer system response to a differential forcing action $f_3 > f_1 > f_2$.

For the third layer similarly to the first one:

$$\alpha_3^{3\text{layers}} = \alpha_3 + \alpha_{31,3} + \alpha_{23,2} + \alpha_{13,1}, \tag{5.143}$$

$$\alpha_3^{3\text{layers}} = (1 + \gamma_{31,3} + \gamma_{23,2})\alpha_3 + \alpha_{13,1}\alpha_1. \tag{5.144}$$

An example of the velocity profile in the 3-layer system (LMB prototype) is shown in the Figure 5.3. The condition $f_3 > f_1 > f_2$ results in the largest velocity in upper layer. Velocity in the middle layer varies linearly, while in the surrounding layers profiles are parabolic.

The obtained expressions are based on the purely physical assumptions and will be used in the following chapters to analyse impact of the drag mechanism on the interfacial stability in the LMBs.

5.5 Numerical model for fully coupled 3 shallow layers

5.5.1 Interfacial dynamics

The set of the wave equations (5.25), (5.27) with the corresponding boundary conditions (5.26), (5.28) can be rewritten in a weak form by means of integrating the equations on the horizontal interface Γ against a regular function q, similar strategy was applied for the two layer problem in [5]

$$\int_\Gamma \alpha_1(\partial_{tt}\zeta_1)qd\sigma + \int_\Gamma k_{f1}(\partial_t\zeta_1)qd\sigma - \int_\Gamma \frac{\rho_2}{h_{02}}(\partial_{tt}\zeta_2)qd\sigma - \int_\Gamma \frac{\rho_2 k_{f2}}{h_{02}}(\partial_t\zeta_2)qd\sigma$$
$$+ \int_\Gamma R_1(\boldsymbol{\nabla}\zeta_1, \boldsymbol{\nabla}q)d\sigma = \int_\Gamma [F_{j2} - F_{j1} + \rho_1(U_{k1}\partial_k U_{j1}) - \rho_2(U_{k2}\partial_k U_{j2})]\partial_j q d\sigma, \tag{5.145}$$

$$\int_\Gamma \alpha_2(\partial_{tt}\zeta_2)qd\sigma + \int_\Gamma k_{f3}(\partial_t\zeta_2)qd\sigma - \int_\Gamma \frac{\rho_2}{h_{02}}(\partial_{tt}\zeta_1)qd\sigma - \int_\Gamma \frac{\rho_2 k_{f2}}{h_{02}}(\partial_t\zeta_1)qd\sigma$$
$$+ \int_\Gamma R_2(\boldsymbol{\nabla}\zeta_2, \boldsymbol{\nabla}q)d\sigma = \int_\Gamma [F_{j3} - F_{j2} + \rho_1(U_{k2}\partial_k U_{j2}) - \rho_2(U_{k3}\partial_k U_{j3})]\partial_j q d\sigma, \tag{5.146}$$

where $d\sigma = dxdy$ and the integration is over Γ. In the particular case ζ must satisfy the corresponding equations for all test-functions q that belong to $H^1(\Gamma)$. The following set of functions is introduced:

$$\Lambda = \left\{ \frac{2}{\sqrt{L_x L_y}} \epsilon_{\boldsymbol{k}} \cos(k_x x)\cos(k_y y); k_x = \frac{m\pi}{L_x}, k_y = \frac{n\pi}{L_y}; m, n \in N \right\}, \tag{5.147}$$

$$\epsilon_{\boldsymbol{k}} = \begin{cases} 1 & \text{if } k_x, k_y \neq 0, \\ 1/\sqrt{2} & \text{if } k_x \text{ or } k_y = 0, k_x \neq k_y, \\ 1/2 & \text{if } k_x = k_y = 0. \end{cases}$$

The elements of Λ form orthogonal basis of $H^1(\Gamma)$ and the corresponding physical unknowns can be expressed in a similar form as the series:

$$\zeta_1 = \sum_{\boldsymbol{k}} \widehat{\zeta}_{1,\boldsymbol{k}}(t) \frac{2}{\sqrt{L_x L_y}} \epsilon_{\boldsymbol{k}} \cos(k_x x)\cos(k_y y), \tag{5.148}$$

$$\zeta_2 = \sum_{\boldsymbol{k}} \widehat{\zeta}_{2,\boldsymbol{k}}(t) \frac{2}{\sqrt{L_x L_y}} \epsilon_{\boldsymbol{k}} \cos(k_x x)\cos(k_y y), \tag{5.149}$$

where $\boldsymbol{k} = (k_x, k_y)$. Note, that the boundary conditions are satisfied in the weak sense only when using the functions (5.148) and (5.149). Taking into account the

orthogonality properties of the cosine functions the set of wave equations including the boundary conditions can be rewritten in the spectral coefficient space:

$$\partial_{tt}\widehat{\zeta}_{1,k} + \gamma_1 \partial_t \widehat{\zeta}_{1,k} - R_{C,1}\partial_{tt}\widehat{\zeta}_{2,k} - \gamma_{12}\partial_t \widehat{\zeta}_{2,k} + \omega_{1,k}^2 \widehat{\zeta}_{1,k} = \alpha_1^{-1}\widehat{\Xi}_{1,k}, \tag{5.150}$$

$$\partial_{tt}\widehat{\zeta}_{2,k} + \gamma_2 \partial_t \widehat{\zeta}_{2,k} - R_{C,2}\partial_{tt}\widehat{\zeta}_{1,k} - \gamma_{21}\partial_t \widehat{\zeta}_{1,k} + \omega_{2,k}^2 \widehat{\zeta}_{2,k} = \alpha_2^{-1}\widehat{\Xi}_{2,k}, \tag{5.151}$$

where the new coefficients are defined as

$$\gamma_1 = \alpha_1^{-1}(\rho_1 k_{f1}/h_{01} + \rho_2 k_{f2}/h_{02}), \tag{5.152}$$

$$\gamma_2 = \alpha_2^{-1}(\rho_2 k_{f2}/h_{02} + \rho_3 k_{f3}/h_{03}), \tag{5.153}$$

$$R_{C,1} = \alpha_1^{-1}\rho_2/h_{02}, \tag{5.154}$$

$$R_{C,2} = \alpha_2^{-1}\rho_2/h_{02}, \tag{5.155}$$

$$\gamma_{12} = R_{C,1}k_{f2}, \tag{5.156}$$

$$\gamma_{21} = R_{C,2}k_{f2}. \tag{5.157}$$

The corresponding uncoupled shallow layer gravity wave frequencies are

$$\omega_{1,k}^2 = R_1\alpha_1^{-1}\boldsymbol{k}^2, \tag{5.158}$$

$$\omega_{2,k}^2 = R_2\alpha_2^{-1}\boldsymbol{k}^2. \tag{5.159}$$

The notation $\widehat{\Xi}_k$ symbolically represents the combination of the electromagnetic forcing and the non-linear velocity terms:

$$\widehat{\Xi}_{1,k} = \int_\Gamma [F_{j2} - F_{j1} + \rho_1(U_{k1}\partial_k U_{j1}) - \rho_2(U_{k2}\partial_k U_{j2})]\partial_j q d\sigma, \tag{5.160}$$

$$\widehat{\Xi}_{2,k} = \int_\Gamma [F_{j3} - F_{j2} + \rho_2(U_{k2}\partial_k U_{j2}) - \rho_3(U_{k3}\partial_k U_{j3})]\partial_j q d\sigma. \tag{5.161}$$

The set of equations (5.150) and (5.151) in the second order accurate central finite difference representation is

$$\begin{aligned}&\frac{\widehat{\zeta}_{1,k}(t_{i+1}) - 2\widehat{\zeta}_{1,k}(t_i) + \widehat{\zeta}_{1,k}(t_{i-1})}{(\triangle t)^2} + \gamma_1 \frac{\widehat{\zeta}_{1,k}(t_{i+1}) - \widehat{\zeta}_{1,k}(t_{i-1})}{2\triangle t} - \gamma_{12} \frac{\widehat{\zeta}_{2,k}(t_{i+1}) - \widehat{\zeta}_{2,k}(t_{i-1})}{2\triangle t} \\ &- R_{c,1} \frac{\widehat{\zeta}_{2,k}(t_{i+1}) - 2\widehat{\zeta}_{2,k}(t_i) + \widehat{\zeta}_{2,k}(t_{i-1})}{(\triangle t)^2} + \omega_{1,k}^2 \frac{\widehat{\zeta}_{1,k}(t_{i+1}) - \widehat{\zeta}_{1,k}(t_{i-1})}{2} = \widehat{\Xi}_{1,k}(t_i),\end{aligned} \tag{5.162}$$

$$\begin{aligned}&\frac{\widehat{\zeta}_{2,k}(t_{i+1}) - 2\widehat{\zeta}_{2,k}(t_i) + \widehat{\zeta}_{2,k}(t_{i-1})}{(\triangle t)^2} + \gamma_2 \frac{\widehat{\zeta}_{2,k}(t_{i+1}) - \widehat{\zeta}_{2,k}(t_{i-1})}{2\triangle t} - \gamma_{21} \frac{\widehat{\zeta}_{1,k}(t_{i+1}) - \widehat{\zeta}_{1,k}(t_{i-1})}{2\triangle t} \\ &- R_{c,2} \frac{\widehat{\zeta}_{1,k}(t_{i+1}) - 2\widehat{\zeta}_{1,k}(t_i) + \widehat{\zeta}_{1,k}(t_{i-1})}{(\triangle t)^2} + \omega_{2,k}^2 \frac{\widehat{\zeta}_{2,k}(t_{i+1}) - \widehat{\zeta}_{2,k}(t_{i-1})}{2} = \widehat{\Xi}_{2,k}(t_i),\end{aligned} \tag{5.163}$$

where $\triangle t$ is the time step. The corresponding integrals are approximated with a trapezoidal integration scheme which is the most sufficient for trigonometric functions [59].

5.5.2 Electric current flow

The set of the equations for the electric potential perturbations (5.64), (5.65) with the boundary conditions (5.40) give the following weak form:

$$\int_\Gamma h_{01}h_{02}(\boldsymbol{\nabla}\Phi_1, \boldsymbol{\nabla} r)d\sigma + \int_\Gamma \sigma_{e,1}\Phi_1 r d\sigma = -\frac{j_0}{\sigma_1}\int_\Gamma (\zeta_2 - \zeta_1) r d\sigma, \tag{5.164}$$

$$\int_\Gamma h_{02}h_{03}(\boldsymbol{\nabla}\Phi_3, \boldsymbol{\nabla}r)d\sigma + \int_\Gamma \sigma_{e,2}\Phi_3 r d\sigma = \frac{j_0}{\sigma_3}\int_\Gamma(\zeta_2 - \zeta_1)rd\sigma. \tag{5.165}$$

Similarly to previous case, the solution is constructed in the $H^1(\Gamma)$ space using functions from the Λ set. The unknowns are expressed in a following form:

$$\Phi_1 = \sum_{\boldsymbol{k}} \widehat{\Phi}_{1,\boldsymbol{k}}(t)\frac{2}{\sqrt{L_x L_y}}\epsilon_{\boldsymbol{k}}\cos(k_x x)\cos(k_y y), \tag{5.166}$$

$$\Phi_3 = \sum_{\boldsymbol{k}} \widehat{\Phi}_{3,\boldsymbol{k}}(t)\frac{2}{\sqrt{L_x L_y}}\epsilon_{\boldsymbol{k}}\cos(k_x x)\cos(k_y y). \tag{5.167}$$

The resulting set of the equations for the potentials in the spectral coefficient space is

$$\left(h_{01}h_{02}\boldsymbol{k}^2 + \sigma_{e,1}\right)\widehat{\Phi}_{1,\boldsymbol{k}} = -\frac{j_0}{\sigma_1}(\widehat{\zeta}_{2,\boldsymbol{k}} - \widehat{\zeta}_{1,\boldsymbol{k}}); \tag{5.168}$$

$$\left(h_{02}h_{03}\boldsymbol{k}^2 + \sigma_{e,2}\right)\widehat{\Phi}_{3,\boldsymbol{k}} = \frac{j_0}{\sigma_3}(\widehat{\zeta}_{2,\boldsymbol{k}} - \widehat{\zeta}_{1,\boldsymbol{k}}). \tag{5.169}$$

The potential distribution can be easily determined from (5.168) and (5.169) for particular interfacial deformations. Using (5.68)-(5.70) the electric current distribution in the system can be reconstructed.

5.5.3 Fluid dynamics

Potential flow

The weak form of the continuity equations (5.73)-(5.75) is

$$\frac{1}{h_{01}}\int_\Gamma(\partial_t\zeta_1)qd\sigma = \int_\Gamma(\boldsymbol{\nabla}\chi_1, \boldsymbol{\nabla}q)d\sigma, \tag{5.170}$$

$$\frac{1}{h_{02}}\int_\Gamma[\partial_t(\zeta_2 - \zeta_1)]qd\sigma = \int_\Gamma(\boldsymbol{\nabla}\chi_2, \boldsymbol{\nabla}q)d\sigma, \tag{5.171}$$

$$\frac{1}{h_{03}}\int_\Gamma(\partial_t\zeta_2)qd\sigma = -\int_\Gamma(\boldsymbol{\nabla}\chi_3, \boldsymbol{\nabla}q)d\sigma. \tag{5.172}$$

The solution form of the potential velocities is expressed as follows

$$\chi_1 = \sum_k \widehat{\chi}_{1,k}(t) \frac{2}{\sqrt{L_x L_y}} \epsilon_k \cos(k_x x) \cos\big(k_y y\big), \tag{5.173}$$

$$\chi_2 = \sum_k \widehat{\chi}_{2,k}(t) \frac{2}{\sqrt{L_x L_y}} \epsilon_k \cos(k_x x) \cos\big(k_y y\big), \tag{5.174}$$

$$\chi_3 = \sum_k \widehat{\chi}_{3,k}(t) \frac{2}{\sqrt{L_x L_y}} \epsilon_k \cos(k_x x) \cos\big(k_y y\big), \tag{5.175}$$

Resulting set of the equations in the spectral space is

$$\partial_t \widehat{\zeta}_{1,k} = h_{01} \boldsymbol{k}^2 \widehat{\chi}_{1,k}, \tag{5.176}$$

$$\partial_t (\widehat{\zeta}_{2,k} - \widehat{\zeta}_{1,k}) = h_{02} \boldsymbol{k}^2 \widehat{\chi}_{2,k}, \tag{5.177}$$

$$\partial_t \widehat{\zeta}_{2,k} = -h_{03} \boldsymbol{k}^2 \widehat{\chi}_{3,k}, \tag{5.178}$$

The evolution of the velocity potential in the second order accurate central finite difference representation is

$$\widehat{\chi}_{1,k}(t_{i+1}) = \frac{\frac{3}{2}\widehat{\zeta}_{1,k}(t_{i+1}) - 2\widehat{\zeta}_{1,k}(t_i) + \frac{1}{2}\widehat{\zeta}_{1,k}(t_{i-1})}{h_{01} \boldsymbol{k}^2 \triangle t}, \tag{5.179}$$

$$\widehat{\chi}_{3,k}(t_{i+1}) = -\frac{\frac{3}{2}\widehat{\zeta}_{2,k}(t_{i+1}) - 2\widehat{\zeta}_{2,k}(t_i) + \frac{1}{2}\widehat{\zeta}_{2k}(t_{i-1})}{h_{03} \boldsymbol{k}^2 \triangle t}, \tag{5.180}$$

$$\widehat{\chi}_{2,k}(t_{i+1}) = -\frac{h_{03}\widehat{\chi}_{3,k}(t_{i+1}) + h_{01}\widehat{\chi}_{1,k}(t_{i+1})}{h_{02}}. \tag{5.181}$$

Vortical flow

The equation for the stream function (5.76) in the weak formulation is

$$\int_{\partial\Gamma} \rho s \partial_n (\partial_t \psi_k + \kappa_k \psi_k) d\tau - \int_\Gamma \rho_k \partial_i s (\partial_{ti} \psi_m + \kappa_k \partial_i \psi_k) d\sigma = \int_\Gamma s(\partial_x F_{ky} - \partial_y F_{kx}) d\sigma \tag{5.182}$$

The test-functions s also belong to $H^1(\Gamma)$. The following set of functions will be used

$$\Omega = \left\{ \frac{2}{\sqrt{L_x L_y}} \sin(k_x x) \sin(k_y y); k_x = \frac{m\pi}{L_x}, k_y = \frac{n\pi}{L_y}; m, n \in N \right\}. \tag{5.183}$$

The physical unknown functions which satisfy the boundary conditions are expressed as:

$$\psi_1 = \sum_{\boldsymbol{k}} \widehat{\psi}_{1,k}(t) \frac{2}{\sqrt{L_x L_y}} \sin(k_x x) \sin(k_y y), \tag{5.184}$$

$$\psi_2 = \sum_{\boldsymbol{k}} \widehat{\psi}_{2,k}(t) \frac{2}{\sqrt{L_x L_y}} \sin(k_x x) \sin(k_y y), \tag{5.185}$$

$$\psi_3 = \sum_{\boldsymbol{k}} \widehat{\psi}_{3,k}(t) \frac{2}{\sqrt{L_x L_y}} \sin(k_x x) \sin(k_y y). \tag{5.186}$$

Using orthogonality properties, the following equation for the stream function in the spectral coefficient space can be derived

$$\partial_t \widehat{\psi}_{k,\boldsymbol{k}} + k_{fk} \widehat{\psi}_{k,\boldsymbol{k}} = (\rho_k \boldsymbol{k}^2)^{-1} \widehat{\Upsilon}_{k,\boldsymbol{k}}, \tag{5.187}$$

where

$$\widehat{\Upsilon}_{k,\boldsymbol{k}} = \int_\Gamma (\partial_x F_{ky} - \partial_y F_{kx}) s d\sigma. \tag{5.188}$$

The equation (5.187) in the second order accurate central finite difference representation is

$$\frac{\widehat{\psi}_{k,\boldsymbol{k}}(t_{i+1}) - \widehat{\psi}_{k,\boldsymbol{k}}(t_{i-1})}{2\triangle t} + k_{fk} \frac{\widehat{\psi}_{k,\boldsymbol{k}}(t_{i+1}) + \widehat{\psi}_{k,\boldsymbol{k}}(t_{i-1})}{2} = (\rho_k \boldsymbol{k}^2)^{-1} \widehat{\Upsilon}_{k,\boldsymbol{k}}(t_i). \tag{5.189}$$

The numerical solution is obtained following the schematic representation shown in Figure 5.4. Assuming that the initial interfacial perturbations, the electric current

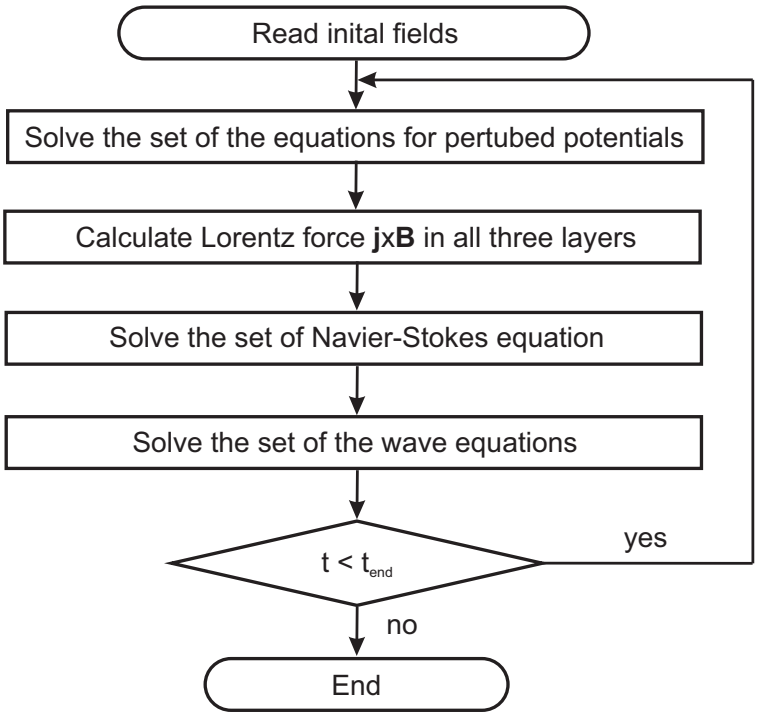

FIGURE 5.4: Flow chart of the fully coupled 3-layer simulation model.

and the magnetic field distribution are given the perturbed electric potentials are determined at the first time step. Then distribution of the Lorentz forces is found. In the following step the Navier-Stokes equations are computed (5.189). In the main loop of the numerical scheme the wave equations (5.162) and (5.163) are solved accounting for the non-linear interaction with the velocity. The velocity field and interfacial deformations are used to continue time stepping until the predetermined exit time. The interface, velocity and electric current fields are stored at selected time steps for the purpose of graphical presentation in animated form using Matlab and Tecplot. In the numerical examples $\triangle t = 0.05$s for time step and $(N, M) = (87, 31)$ for Fourier modes were found to be sufficient if comparing to simulations with reduced values. The typical Courant-Friedrich-Lewy parameter in 2D domain [59]: $C_i = R_i \alpha_i^{-1} \triangle t (1/\triangle x + 1/\triangle y)$ for the lower interface is $C_1 = 0.62 < 1$, whereas for the upper interface it is $C_2 = 0.002 < 1$. The advantage of the chosen numerical strategy based on the spectral methodology compared to the 3D finite volume based solvers is high accuracy, no numerical diffusion of the free interfaces and significantly reduced computational times [11, 59].

The following Chapter 6 considers linear stability of the interfacial waves in

purely vertical magnetic field. Applicability limits of this approximation using the described numerical model will be estimated for realistic battery cases.

Chapter 6

Linear stability analysis

6.1 Overview

In this chapter linear stability analysis of the multiple mode interaction is investigated accounting for continuous electric current in the presence of a purely vertical magnetic field. The role of dissipation rate will be considered using both analytical tools and numerical solutions.

6.2 Coupled 3-layer problem

The wave equations (5.25)-(5.27) can be linearised neglecting the ε-order nonlinear terms and assuming a given magnetic field distribution, which can be expanded in terms of the small parameter δ: $\boldsymbol{B}(x,y,z) = \boldsymbol{B}^0(x,y) + \delta\boldsymbol{B}^1(x,y,z) + O(\delta^2)$. It was shown in [5, 39, 43, 44] that the interaction of the vertical magnetic field component with horizontal currents is the most crucial for the interfacial wave stability in HHC. In this chapter impact of this interaction on the stability of LMB is analysed. It is assumed that the magnetic field is purely-vertical $\boldsymbol{B} = \boldsymbol{B}^0 = B_z^0(x,y)\boldsymbol{e}_z$, it is caused by external sources (supply lines, neighbouring batteries etc.). The set of the derived wave equations for this case has the following form after assuming that the friction at the electrolyte top and bottom is negligible in comparison to the friction at the solid top and bottom:

$$\begin{aligned} \alpha_1\partial_{tt}\zeta_1 \quad + \quad & k_{f1}\partial_t\zeta_1 - \frac{\rho_2}{h_2}\partial_{tt}\zeta_2 \\ & = R_1\partial_{jj}\zeta_1 + \sigma_1(\partial_y\Phi_1\partial_x B_z^0 - \partial_x\Phi_1\partial_y B_z^0), \end{aligned} \tag{6.1}$$

$$\alpha_2\partial_{tt}\zeta_2 + k_{f3}\partial_t\zeta_2 - \frac{\rho_2}{h_2}\partial_{tt}\zeta_1 = R_2\partial_{jj}\zeta_2 + \sigma_3(\partial_x\Phi_3\partial_y B_z^0 - \partial_y\Phi_3\partial_x B_z^0), \tag{6.2}$$

with the boundary conditions at the side-walls:

$$R_1\partial_n\zeta_1 - B_z^0\sigma_1(n_y\partial_x\Phi_1 - n_x\partial_y\Phi_1) = 0, \tag{6.3}$$

$$R_2\partial_n\zeta_2 - B_z^0\sigma_3(n_x\partial_y\Phi_3 - n_y\partial_x\Phi_3) = 0. \tag{6.4}$$

The electric potential distribution is governed by the set of equations (5.64), (5.65). Note, that the coefficients in (5.64) and (5.65) contain only the constant parts of the layer thickness.

Following the same strategy as it was described in the Chapter 5 the problem can be rewritten in the spectral coefficient space:

$$\begin{aligned}\partial_{tt}\widehat{\zeta}_{1,\boldsymbol{k}} + \gamma_1\partial_t\widehat{\zeta}_{1,\boldsymbol{k}} - R_{c,1}\partial_{tt}\widehat{\zeta}_{2,\boldsymbol{k}} + \omega_{1,\boldsymbol{k}}^2\widehat{\zeta}_{1,\boldsymbol{k}} \\ = -\sum_{\boldsymbol{k}'\geq 0}\frac{\sigma_1}{4\alpha_1}\epsilon_{\boldsymbol{k}}\epsilon_{\boldsymbol{k}'}[(k_y'k_x - k_x'k_y)(\widehat{B}_{k_x'+k_x,k_y'+k_y} - \widehat{B}_{k_x'-k_x,k_y'-k_y}) \\ +(k_y'k_x + k_x'k_y)(\widehat{B}_{k_x'+k_x,k_y'-k_y} - \widehat{B}_{k_x'-k_x,k_y'+k_y})]\widehat{\Phi}_{1,\boldsymbol{k}'},\end{aligned} \tag{6.5}$$

$$\begin{aligned}\partial_{tt}\widehat{\zeta}_{2,\boldsymbol{k}} + \gamma_2\partial_t\widehat{\zeta}_{2,\boldsymbol{k}} - R_{c,2}\partial_{tt}\widehat{\zeta}_{1,\boldsymbol{k}} + \omega_{2,\boldsymbol{k}}^2\widehat{\zeta}_{2,\boldsymbol{k}} \\ = -\sum_{\boldsymbol{k}'\geq 0}\frac{\sigma_3}{4\alpha_2}\cdot\epsilon_{\boldsymbol{k}}\epsilon_{\boldsymbol{k}'}[(k_y'k_x - k_x'k_y)(\widehat{B}_{k_x'-k_x,k_y'-k_y} - \widehat{B}_{k_x'+k_x,k_y'+k_y}) \\ +(k_y'k_x + k_x'k_y)(\widehat{B}_{k_x'-k_x,k_y'+k_y} - \widehat{B}_{k_x'+k_x,k_y'-k_y})]\widehat{\Phi}_{3,\boldsymbol{k}'}.\end{aligned} \tag{6.6}$$

The selection of the magnetic field modes in (6.5), (6.6) are obtained from the given magnetic field $B_z^0(x,y)$ with a Fourier expansion in sine functions:

$$\widehat{B}_{k_x,k_y} = \frac{4}{L_x L_y} \int_\Gamma B_z^0 \sin(k_x x) \sin\big(k_y y\big) dxdy, \tag{6.7}$$

for both positive and negative k_x, k_y. In the particular case of a uniform constant magnetic field $B_z = B_z^0 = const$ the expansion coefficients are

$$\widehat{B}_{k_x,k_y} = \frac{4B_z^0}{mn\pi^2}[1-(-1)^m][1-(-1)^n], \tag{6.8}$$

where $(k_x, k_y) = (m\pi/L_x, n\pi/L_y)$.

The set of equations for the potentials in the spectral representation is

$$\left(h_1 h_2 \boldsymbol{k}^2 + \sigma_{e,1}\right) \widehat{\Phi}_{1,k} = -\frac{j_0}{\sigma_1}(\widehat{\zeta}_{2,k} - \widehat{\zeta}_{1,k}), \tag{6.9}$$

$$\left(h_2 h_3 \boldsymbol{k}^2 + \sigma_{e,2}\right) \widehat{\Phi}_{3,k} = \frac{j_0}{\sigma_3}(\widehat{\zeta}_{2,k} - \widehat{\zeta}_{1,k}). \tag{6.10}$$

The wave equations and the potential equations can be combined by means of the following transformation [5]:

$$\widetilde{\zeta}_{1,k} = \left(h_1 h_2 \boldsymbol{k}^2 + \sigma_{e,1}\right)^{-1/2} \widehat{\zeta}_{1,k}, \tag{6.11}$$

$$\widetilde{\zeta}_{2,k} = \left(h_1 h_2 \boldsymbol{k}^2 + \sigma_{e,1}\right)^{-1/2} \widehat{\zeta}_{2,k}. \tag{6.12}$$

The resulting set of wave equations will have the following form suitable for eigenvalue analysis:

$$\partial_{tt}\widetilde{\zeta}_{1,k} + \gamma_1 \partial_t \widetilde{\zeta}_{1,k} - R_{c,1}\partial_{tt}\widetilde{\zeta}_{2,k} + \omega_{1,k}^2 \widetilde{\zeta}_{1,k} = \sum_{k' \geq 0} G_{1,k,k'}(\widetilde{\zeta}_{1,k'} - \widetilde{\zeta}_{2,k'}), \tag{6.13}$$

$$\partial_{tt}\widetilde{\zeta}_{2,k} + \gamma_2 \partial_t \widetilde{\zeta}_{2,k} - R_{c,2}\partial_{tt}\widetilde{\zeta}_{1,k} + \omega_{2,k}^2 \widetilde{\zeta}_{2,k} = \sum_{k' \geq 0} G_{2,k,k'}(\widetilde{\zeta}_{2,k'} - \widetilde{\zeta}_{1,k'}), \tag{6.14}$$

where the magnetic interaction matrices are introduced as

$$
\begin{aligned}
G_{1,\boldsymbol{k},\boldsymbol{k'}} &= -\frac{j_0}{4\alpha_1}\epsilon_{\boldsymbol{k}}\epsilon_{\boldsymbol{k'}}[(k'_y k_x - k'_x k_y)(\widehat{B}_{k'_x+k_x,k'_y+k_y} - \widehat{B}_{k'_x-k_x,k'_y-k_y}) \\
&\quad +(k'_y k_x + k'_x k_y)(\widehat{B}_{k'_x+k_x,k'_y-k_y} - \widehat{B}_{k'_x-k_x,k'_y+k_y})] \\
&\quad \times \left(h_1 h_2 \boldsymbol{k}^2 + \sigma_{e,1}\right)^{-1/2} \left(h_1 h_2 \boldsymbol{k'}^2 + \sigma_{e,1}\right)^{-1/2}, \qquad (6.15)
\end{aligned}
$$

$$
\begin{aligned}
G_{2,\boldsymbol{k},\boldsymbol{k'}} &= -\frac{j_0}{4\alpha_2}\epsilon_{\boldsymbol{k}}\epsilon_{\boldsymbol{k'}}[(k'_y k_x - k'_x k_y)(\widehat{B}_{k'_x-k_x,k'_y-k_y} - \widehat{B}_{k'_x+k_x,k'_y+k_y}) \\
&\quad +(k'_y k_x + k'_x k_y)(\widehat{B}_{k'_x-k_x,k'_y+k_y} - \widehat{B}_{k'_x+k_x,k'_y-k_y})] \\
&\quad \times \left(h_1 h_2 \boldsymbol{k}^2 + \sigma_{e,1}\right)^{-1/2} \left(h_1 h_2 \boldsymbol{k'}^2 + \sigma_{e,1}\right)^{1/2} \left(h_2 h_3 \boldsymbol{k'}^2 + \sigma_{e,2}\right)^{-1}. \qquad (6.16)
\end{aligned}
$$

As it can be seen, $G_{1,\boldsymbol{k},\boldsymbol{k'}}$ matches the interaction matrix obtained in [5] for the HHC stability description, however $G_{2,\boldsymbol{k},\boldsymbol{k'}}$ is different and the skew-symmetry for this particular matrix is not retained. The interaction matrices $G_{1,\boldsymbol{k},\boldsymbol{k'}}$ and $G_{2,\boldsymbol{k},\boldsymbol{k'}}$ are valid for an arbitrary $B_z^0(x,y)$.

6.3 Coupled gravity waves

Before performing a stability analysis of the electro-magnetically caused interactions, let us consider properties of the purely hydrodynamically coupled waves. By neglecting the electro-magnetic and the dissipation terms, equations (6.13) and (6.14) can be solved for the 2 coupled interface gravity wave frequencies:

$$
\omega^2_{12,\boldsymbol{k}} = \frac{-(\omega^2_{1,\boldsymbol{k}} + \omega^2_{2,\boldsymbol{k}}) \pm [(\omega^2_{1,\boldsymbol{k}} - \omega^2_{2,\boldsymbol{k}})^2 + 4R_{c,1}R_{c,2}\omega^2_{1,\boldsymbol{k}}\omega^2_{2,\boldsymbol{k}}]^{1/2}}{2(1 - R_{c,1}R_{c,2})}, \qquad (6.17)
$$

where $"+"$ sign stands for upper metal interface and $"-"$ sign for the lower metal interface. The physical meaning of the solutions (6.17) is best analysed by solving numerically the wave evolution equations (6.13), (6.14) to inspect specific initial perturbation effects on the two coupled interfaces. For this purpose the fully coupled 3-layer simulation model, which was described in the previous Chapter 5, was applied.

Liquid	ρ_i, kg m^{-3}	$\approx \nu_i$, m^2 s^{-1}	σ_i, S m^{-1}
Sb	6450	10^{-6}	$0.88 \cdot 10^6$
$MgCl_2$-KCl-NaCl	1715	10^{-6}	250
Mg	1585	10^{-6}	$3.65 \cdot 10^6$

TABLE 6.1: Material parameters used in numerical examples: density ρ, kinematic viscosity ν, conductivity σ of the three fluids comprising magnesium-based LMB ($\triangle\rho_1 \gg \triangle\rho_2$).

The results are shown as interface oscillations at the fixed position ($x = 0$, $y = 0$) and the respective Fourier power spectra determined for different perturbation types: $(m, n) = \cos(m\pi/L_x) + \cos(n\pi/L_y)$. The first analysed case is for the Mg|$MgCl_2$-KCl-NaCl|Sb battery when $\rho_1 - \rho_2 \gg \rho_2 - \rho_3$ (the component physical properties are given in Table 6.1). Large scale rectangular cell with the dimensions: $L_x = 8$ m and $L_y = 3.6$ m and for a layer thicknesses: $h_1 = 0.2$, $h_2 = 0.04$, $h_3 = 0.2$ m. The results obtained are summarised in Figure 6.1. If only the upper interface is initially perturbed at the amplitude $A = 0.005$ m, using the single mode $m = 1$, $n = 0$, denoted as $(1, 0)$, and the lower interface is initially unperturbed, the initial value problem solution shows that there is only one peak in the spectra, see the Figure 6.1 (a,b). This indicates that the lower interface remains practically motionless while the upper one is oscillating at the chosen initial perturbation frequency. In this example the 2-layer gravity frequencies: (5.158) and (5.159) can be compared to the 3-layer frequencies defined by (6.17). For the upper interface, 2 and 3-layer approaches match quiet well $\omega^{3lay}_{2(1,0)} \approx \omega^{2lay}_{2(1,0)}$. However this is not the case for the lower interface for which $\omega^{3lay}_{1(1,0)}$ is shifted towards higher frequencies compared to the $\omega^{2lay}_{1(1,0)}$.

In the following example shown in Figure 6.1 (c,d), when the lower interface is perturbed and the upper is initially unperturbed, a pair of the frequencies are excited in the system. The lower interface oscillates only at the frequency $\omega^{3lay}_{1(1,0)} (\neq \omega^{2lay}_{1(1,0)})$. The spectrum of the upper interface consists of two peaks excited by the lower interface oscillation: $\omega^{3lay}_{1(1,0)}$ and $\omega^{3lay}_{2(1,0)} \approx \omega^{2lay}_{2(1,0)}$.

When both interfaces are initially perturbed in an asymmetric way (in opposite phase) in the (1,0) modes for amplitudes $A = 0.005$ m, see the Figure 6.1, (e,f), the qualitative picture of the spectrum is similar to the previous case. The upper one contains a superposition of the two frequencies: $\omega^{3lay}_{1(1,0)}$ and $\omega^{3lay}_{2(1,0)}$, whereas the

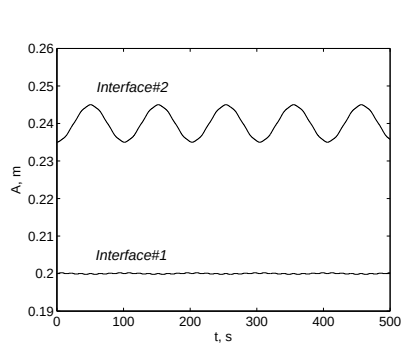

(a) Only the top surface is perturbed

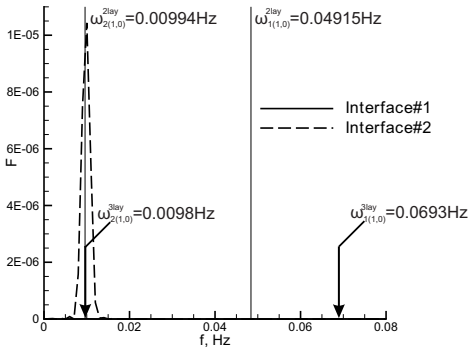

(b)

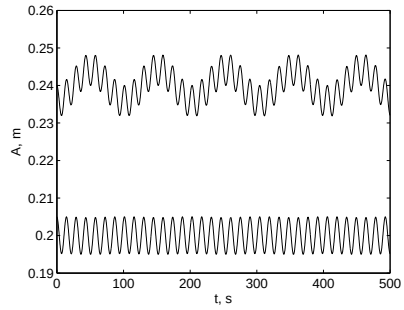

(c) Only the bottom surface is perturbed

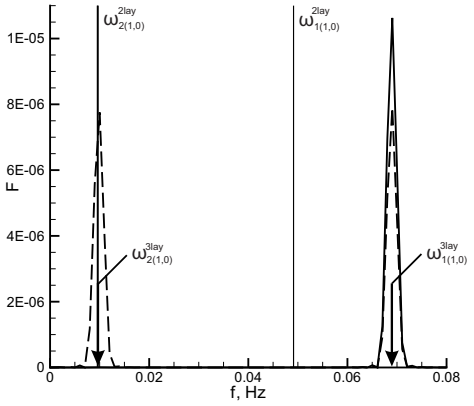

(d)

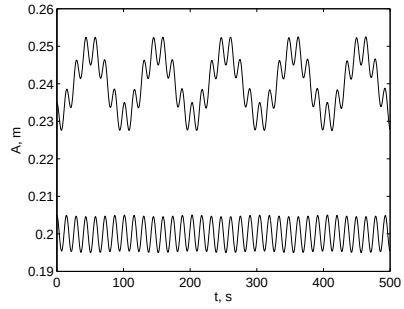

(e) If both surfaces are perturbed asymmetrically

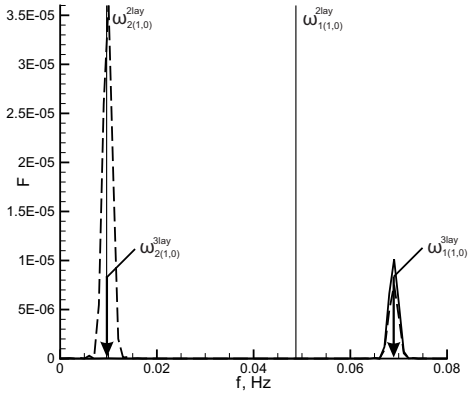

(f)

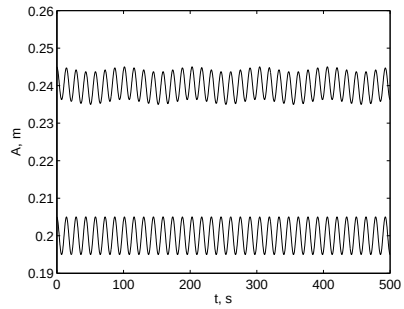

(g) If both surfaces are perturbed symmetrically

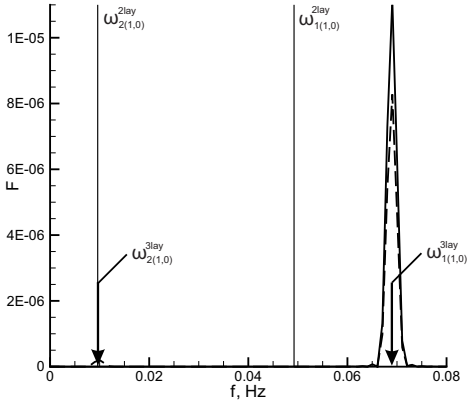

(h)

FIGURE 6.1: 3-layer coupled gravity waves as initial value problem for different perturbation cases for a Mg||Sb battery: the left hand side corresponds to the interface oscillations at the fixed position ($x = 0$, $y = 0$); the right hand side shows the Fourier power spectra.

Liquid	ρ_i, kg m^{-3}	ν_i, m^2 s^{-1}	σ_i, S m^{-1}
Te	5782	10^{-6}	$0.18 \cdot 10^6$
LiCl-LiF-LiI	2690	10^{-6}	250
Li	489	10^{-6}	$4.17 \cdot 10^6$

TABLE 6.2: Material parameters used in numerical examples: density ρ, kinematic viscosity ν, conductivity σ of the three fluids comprising lithium-based LMB ($\triangle\rho_1 \approx \triangle\rho_2$).

lower oscillates at a single frequency: $\omega^{3lay}_{1(1,0)}$.

When the two interfaces are initially perturbed in a symmetric way (in phase) at the respective (1,0) modes, see the Figure 6.1 (g,h), the wave response is quite different. The upper and lower metal interfaces oscillate at the single frequency: $\omega^{3lay}_{1(1,0)}$.

From the above examples it can be concluded that the coupling of wave dynamics in the considered system is not symmetric. This is due to the significant density difference between the layers $\rho_1 - \rho_2 \gg \rho_2 - \rho_3$ (similar results were obtained in direct numerical simulations by [52]).

The excitation frequency response will be different if $\rho_1 - \rho_2 \approx \rho_2 - \rho_3$. To demonstrate this, an exotic battery case: Li|LiCl-LiF-LiI|Te [2] is considered (the component physical properties are given in Table 6.2). The same system geometry and the perturbation strategy as in the previous examples is used. The results obtained are summarised in Figure 6.2. If only the upper interface is initially perturbed and the lower interface is initially unperturbed, there are two frequency peaks observed on each of the interfaces, see the figure Figure 6.2 (a,b). Both interfaces are set into the motion. Each interface oscillates at $\omega^{3lay}_{1(1,0)} \neq \omega^{2lay}_{1(1,0)}$ and $\omega^{3lay}_{2(1,0)} \neq \omega^{2lay}_{2(1,0)}$. In this case $\omega^{3lay}_{1(1,0)}$ is shifted towards higher frequencies compared to $\omega^{2lay}_{1(1,0)}$, and $\omega^{3lay}_{2(1,0)}$ is shifted towards lower frequencies compared to $\omega^{2lay}_{2(1,0)}$.

In the following example (shown in the figure Figure 6.2 (c,d), when the lower interface is perturbed and the upper is initially unperturbed, the situation is very similar to the previous example. Interfaces are oscillating at the two frequencies $\omega^{3lay}_{1(1,0)}$ and $\omega^{3lay}_{2(1,0)}$.

When both interfaces are initially perturbed in the asymmetric way (opposite phase), see the figure Figure 6.2 (e,f), the qualitative picture of the oscillations and

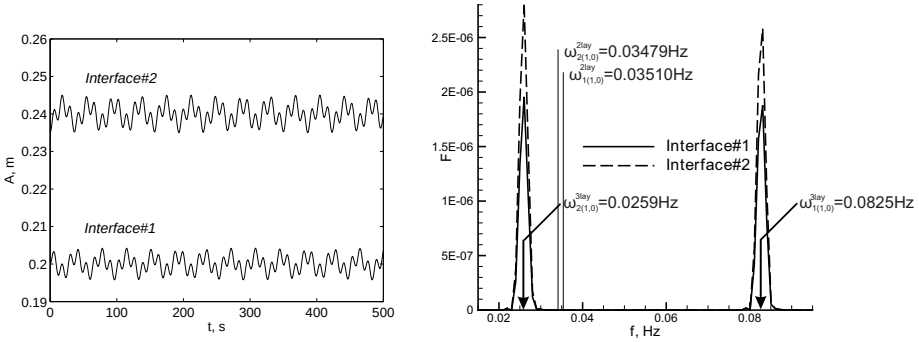

(a) Only the top surface is perturbed

(b)

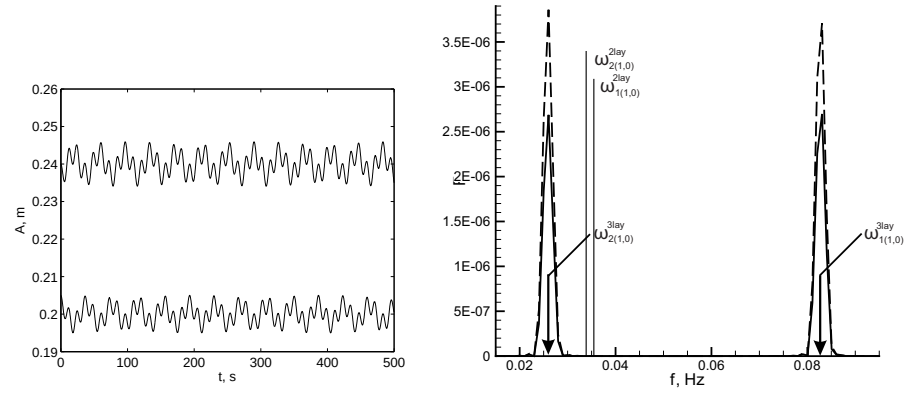

(c) Only the bottom surface is perturbed

(d)

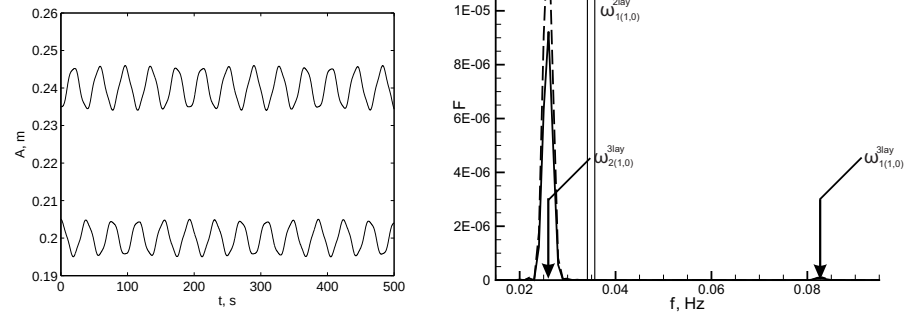

(e) If both surfaces are perturbed asymmetrically

(f)

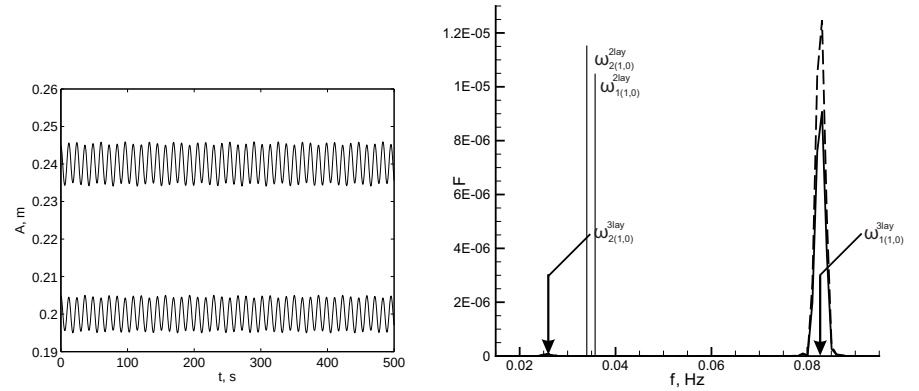

(g) If both surfaces are perturbed symmetrically

(h)

FIGURE 6.2: 3-layer coupled gravity waves as initial value problem for different perturbation cases for a Li||Te battery: the left hand side corresponds to the interface oscillations at the fixed position ($x = 0$, $y = 0$); the right hand side shows the Fourier power spectra.

the spectrum is different. The upper and lower interfaces oscillate at the single frequency, which is $\omega^{3lay}_{2(1,0)}$, while the $\omega^{3lay}_{1(1,0)}$ vanishes from the spectrum.

When both interfaces are initially perturbed in a symmetric way (in phase), see the Figure 6.2 (e,d), the qualitative picture changes again. The upper and lower metal interfaces oscillate at the frequency $\omega^{3lay}_{1(1,0)}$. In this case $\omega^{3lay}_{2(1,0)}$ is absent in the spectrum. Similar differences between the symmetric and asymmetric perturbations when $\rho_1 - \rho_2 \approx \rho_2 - \rho_3$ were predicted in [52].

As it was just shown by the fully coupled 3-layer simulation model the coupled wave dynamics strongly depend on the initial conditions. The question of great importance is if the eigenvalue analysis reproduces the same wave response. To find the answer to this, an additional eigenvalue/eigenvector analysis for purely hydrodynamic waves was performed (details of the model set-up can be found in the next Section 6.4). The coupled interfaces amplitude ratios were compared between the 3-layer simulation model and the eigenvalue analysis predictions. For the Mg||Sb case the initial value problem solution gives the amplitude ratio $\zeta_2/\zeta_1 = 25$ when the $\omega^{3lay}_{2(1,0)}$ frequency is dominant (Figure 6.1 (a,b)) whereas when $\omega^{3lay}_{1(1,0)}$ is dominant the $\zeta_2/\zeta_1 = 1$ (Figure 6.1 (g,h)). For the same system the eigenvalue analysis predicts $\zeta_2/\zeta_1 = 27$ and $\zeta_2/\zeta_1 = 1$ correspondingly. For the Li||Te case the initial value problem solution gives $\zeta_2/\zeta_1 = 1.2$ for the $\omega^{3lay}_{2(1,0)}$ (Figure 6.2 (a,b)), and $\zeta_2/\zeta_1 = 1.18$ for the $\omega^{3lay}_{1(1,0)}$ (Figure 6.2 (g,h)). The eigenvalue analysis predicts respectively $\zeta_2/\zeta_1 = 1.19$ and $\zeta_2/\zeta_1 = 1.18$. The obtained results indicate a relatively good agreement between the two models. However the initial value problem solution outperforms the eigenvalue analysis because it gives the clear answer about the system response depending on the initial state, whereas the eigenvalue analysis provides all possible solutions from which it is non-trivial to choose the outcome for the real system.

In the following sections attention will be focused mainly on the Mg||Sb battery case. The reason is relatively good electrochemical performance, as well as low estimated energy costs for this particular electrode combination [2] (see Figure 6.3).

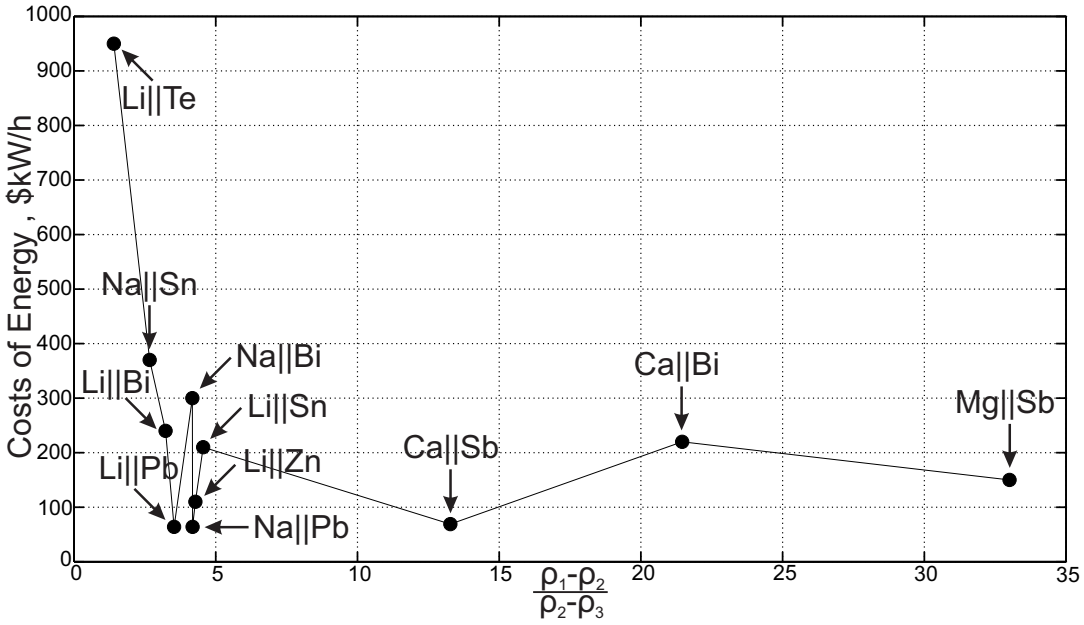

FIGURE 6.3: LMB energy storage costs according to [2].

6.4 MHD eigenvalue problem

Let us proceed now with the stability analysis of the full MHD problem, taking into account the described coupling properties. For this purpose let us assume that the solution form is $\widetilde{\zeta}_i \sim e^{\mu t}$, where μ is representing a set of complex eigenvalues to be obtained from the following eigenvalue problem:

$$(A\mu^2 + B\mu + C) \cdot \zeta = 0. \tag{6.18}$$

The stability analysis will be restricted to selected two mode interaction as in [5]. Then from (6.13), (6.14) the two mode interaction results in:

$$\zeta = \begin{bmatrix} \widetilde{\zeta}_{1,k_1} \\ \widetilde{\zeta}_{1,k_2} \\ \widetilde{\zeta}_{2,k_1} \\ \widetilde{\zeta}_{2,k_2} \end{bmatrix}, \tag{6.19}$$

$$A = \begin{bmatrix} 1 & 0 & -R_{c,1} & 0 \\ 0 & 1 & 0 & -R_{c,1} \\ -R_{c,2} & 0 & 1 & 0 \\ 0 & -R_{c,2} & 0 & 1 \end{bmatrix}, \tag{6.20}$$

$$B = \begin{bmatrix} \gamma_1 & 0 & 0 & 0 \\ 0 & \gamma_1 & 0 & 0 \\ 0 & 0 & \gamma_2 & 0 \\ 0 & 0 & 0 & \gamma_2 \end{bmatrix}, \tag{6.21}$$

$$C = \begin{bmatrix} \omega_{1,k_1}^2 & G_{1,k_1,k_2} & 0 & -G_{1,k_1,k_2} \\ -G_{1,k_1,k_2} & \omega_{1,k_2}^2 & G_{1,k_1,k_2} & 0 \\ 0 & -G_{2,k_1,k_2} & \omega_{3,k_1}^2 & G_{2,k_1,k_2} \\ -G_{2,k_1,k_2}^T & 0 & G_{2,k_1,k_2}^T & \omega_{3,k_2}^2 \end{bmatrix}. \tag{6.22}$$

The problem (6.18) was solved using the QZ algorithm from the standard linear algebra software library LAPACK. At first the role of applied magnetic field on the stability is considered when the uniform vertical B_z is varied from 0 to 3 mT while the total applied current is fixed at: $I = 10^5$ A and the dissipation is neglected ($\gamma_1 = \gamma_2 = 0$). The same cell geometry as in Section 6.3 and the material parameters from the table 6.1 are used. The selected mode interaction for the upper interface is shown in Figure 6.4 (a). With the increase of magnetic field the frequencies of the corresponding modes are shifted towards each other and, when the critical value is reached, the eigenvalues collide, followed by generation of a pair of complex-conjugate eigenvalues. One of these gives a positive growth increment that leads to the system destabilization. The results are indicating that different interactions exhibit different behaviour, however according to the Figure 6.4 (a) the most dangerous growth rates are (1,0)+(0,1); (1,1)+(2,0) and (2,1)+(3,0). To get better understanding which of these interactions might potentially lead to the instability the corresponding eigenvector

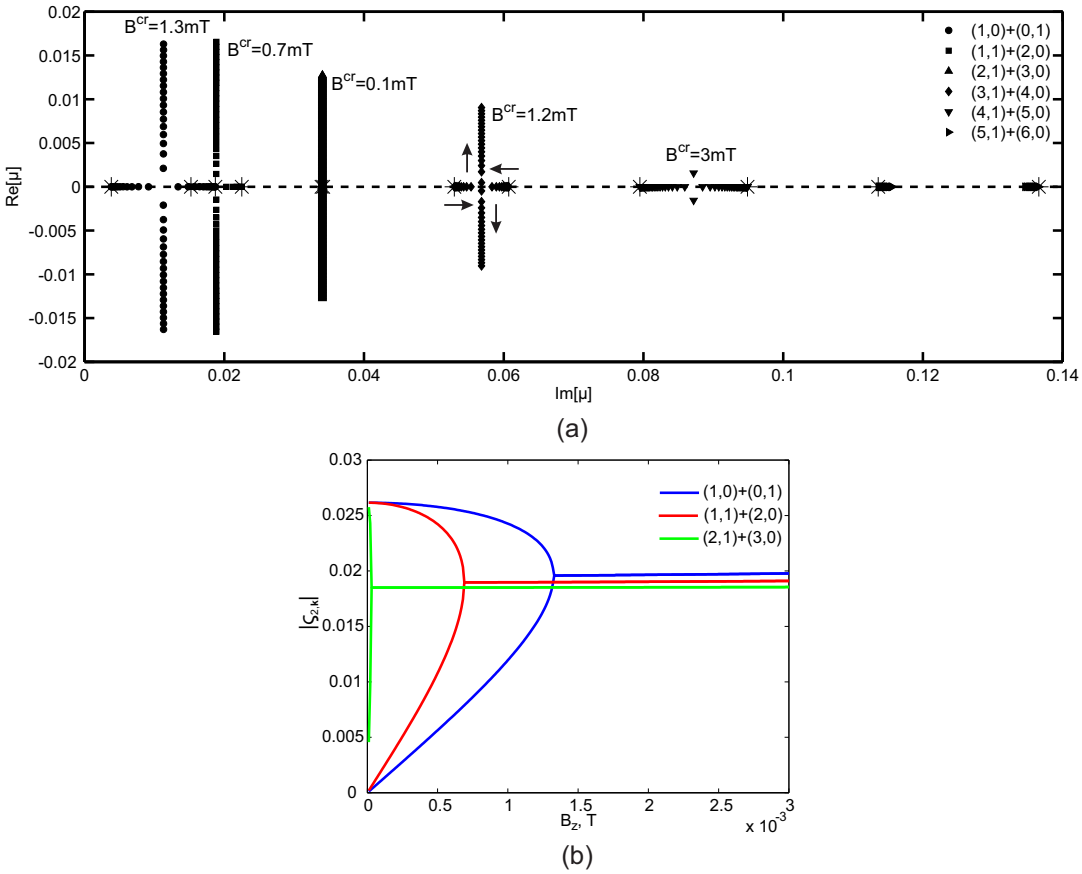

FIGURE 6.4: Eigenvalue/eigenvector analysis for the upper interface: (a) eigenvalues; (b) eigenvector magnitudes ($|\varsigma_{2,k}| = \sqrt{\mathrm{Re}(\varsigma_{2,k})^2 + \mathrm{Im}(\varsigma_{2,k})^2}$) with the incremental rise of magnetic field $B_z = B_z^0 + \Delta B$, where $0 \leq B_z \leq 3$ mT, $\Delta B = 0.1$ mT, $L_x/L_y = 2.2$.

interaction can be considered (Figure 6.4 (b)). With the increase of magnetic field the interacting eigenvectors shift towards each other, and when the critical magnetic field value is reached, similarly to the eigenmodes, they collide and the exponential growth of interfacial displacement starts. After the collision the two eigenvectors continue as a single joint eigenvector, which remains almost constant in magnitude. This indicates that the growth rates of the interactions grow linearly with the magnetic field. In this particular cell the modes (1,0)+(0,1) have the highest magnitude after collision, while the modes (2,1)+(3,0) have lower magnitude. From this it can be concluded that the stability is mostly dominated by (1,0)+(0,1) interaction, as it will be shown in the Sections 6.6 and 6.7. The larger the interacting mode wave number, the larger is the critical magnetic field value at which they collide. For the lower

metal interface all the mode interactions in the considered magnetic field range remain stable due to the considerable density difference of the lower metal and the electrolyte.

6.5 Stability of cell when aspect ratio is natural number

The previous examples demonstrate that some unperturbed gravity wave mode frequencies are very close in value, however at relatively higher mode orders. In the presence of dissipation these will be damped more rapidly than the leading modes $(1,0)$ and $(0,1)$. In a special case, when the cell aspect ratio $L_x/L_y = 1$, the square horizontal section cell is expected to be the most unstable case. The following results are not dependent on the magnitude of the L_x, L_y as long as the δ parameters is sufficiently low to validate the shallow water approximation. If keeping the same total current and the unperturbed current density as in the previous large scale examples, cell stability analysis was performed when aspect ratio is varied. Figure 6.5 shows a comparison of the growth increment dependency on the depth of electrolyte for the cases of coupled all three layers and the two top layers only for cases when $L_x/L_y = 1,2,3,4$. As previously, analysis is restricted to the typical two mode interactions to gain insight to the specific mode interaction mechanisms.

As expected for the cell with $L_x/L_y = 1$ the $(1,0)+(0,1)$ interaction has the lowest critical magnetic field value, whereas when $L_x/L_y = 3$ it is $(4,1)+(5,0)$. From the linear stability analysis these interactions become unstable at the infinitesimally small magnetic field values for all considered electrolyte depth values. On the other hand cells with even aspect ratios e.g. $L_x/L_y = 2$ with the critical $(2,1)+(3,0)$ and $L_x/L_y = 4$ with $(7,1)+(8,0)$ have a finite critical magnetic field values. From this it can be concluded that LMB cells with odd aspect ratios, similarly to HHC [43], are expected to be more unstable than cells with even aspect ratios. As can be seen from the Figure 6.5, the full three layer model is just marginally different to the two layer approach.

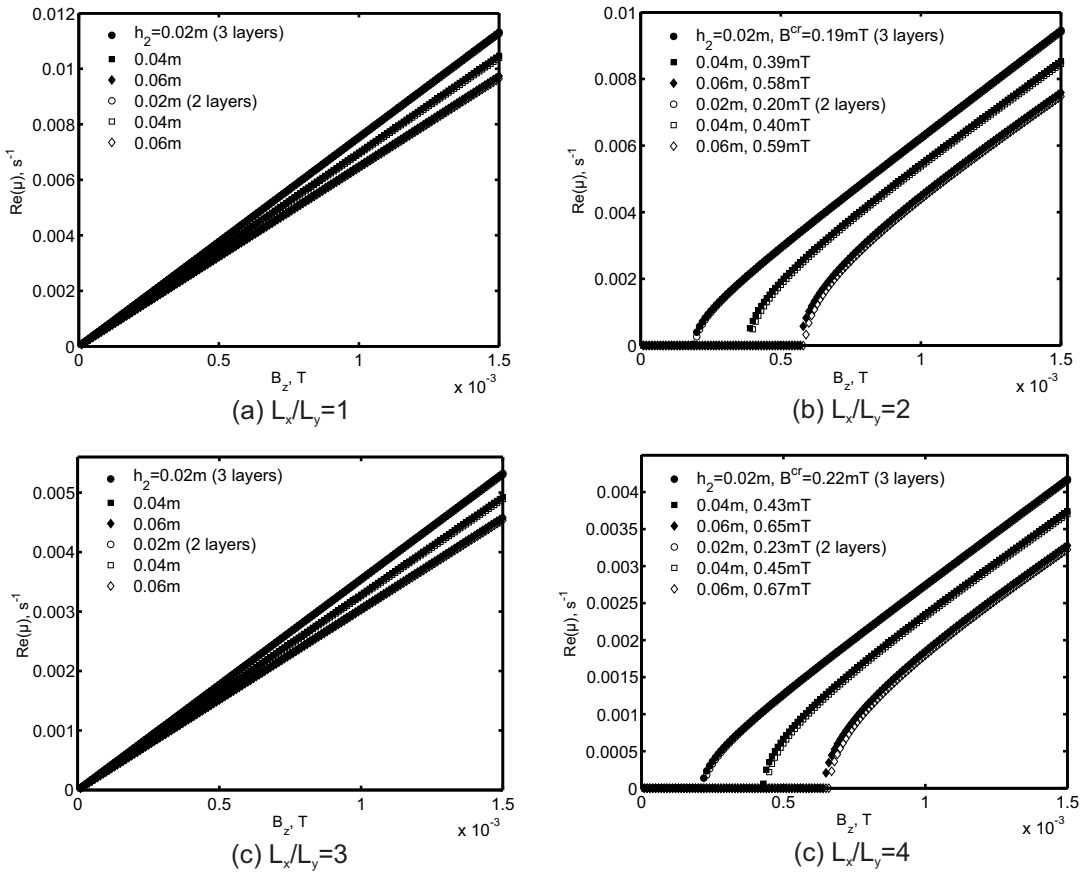

FIGURE 6.5: Comparison of the growth increment dependency on applied magnetic field for the 2-layer and 3-layer models for various values of the electrolyte thickness for cells with different aspect ratio: (a) $(1,0)+(0,1)$ ($L_x = L_y = 5.36$ m); (b) $(1,1)+(2,0)$ ($L_x = 7.58$ m, $L_y = 3.79$ m); (c) $(4,1)+(5,0)$ ($L_x = 9.29$ m, $L_y = 3.09$ m); (d) $(7,1)+(8,0)$ ($L_x = 10.73$ m, $L_y = 2.68$ m).

6.6 Stability criteria with friction effect

The effect of bottom friction on the gravity wave damping is analysed in [62, 63] for laminar flow. In reality the friction coefficient values in the equations (6.13), (6.14) could be significantly higher due to the surface roughness and turbulence generated by the horizontal recirculation flow due to the rotational part of the electromagnetic force in the fluid [45, 64, 65]. The numerical models for aluminium electrolysis cells typically invoke additional turbulence models and empirical values for the bottom friction coefficients, see [37]. The present linear theory can be used to obtain some analytical estimates of the stability criteria for the liquid metal battery MHD waves when the top and bottom friction coefficients are included.

In the previous sections it was demonstrated that the upper interface stability is

the most critical, therefore the derivation will simplified by restricting to the equation for the ζ_2 interface. This derivation extends the results by adding the effects of friction, while maintaining the electric current redistribution due to the lower metal layer. Based on the assumption that the lower metal is at significantly higher density ($\rho_1 \gg \rho_3$, $\zeta_1 \to 0$), the wave equation for the upper interface is

$$\partial_{tt}\widetilde{\zeta}_{\boldsymbol{k}} + \gamma\partial_t\widetilde{\zeta}_{\boldsymbol{k}} + \omega_{\boldsymbol{k}}^2\widetilde{\zeta}_{\boldsymbol{k}} = \sum_{\boldsymbol{k}'\geq 0} G_{\boldsymbol{k},\boldsymbol{k}'}\widetilde{\zeta}_{\boldsymbol{k}'}. \tag{6.23}$$

Taking into account that $\left(h_1h_2\boldsymbol{k}^2 + \sigma_{e,1}\right) \approx \left(h_2h_3\boldsymbol{k}^2 + \sigma_{e,2}\right)$ (6.15) reduces to:

$$\begin{aligned} G_{\boldsymbol{k},\boldsymbol{k}'} \;=\; & -\frac{j}{4\alpha_2}\epsilon_{\boldsymbol{k}}\epsilon_{\boldsymbol{k}'}[(k'_yk_x - k'_xk_y)(\widehat{B}_{k'_x+k_x,k'_y+k_y} - \widehat{B}_{k'_x-k_x,k'_y-k_y}) \\ & +(k'_yk_x + k'_xk_y)(\widehat{B}_{k'_x+k_x,k'_y-k_y} - \widehat{B}_{k'_x-k_x,k'_y+k_y})] \\ & \times \left(h_2h_3\boldsymbol{k}^2 + \sigma_{e,2}\right)^{-1/2}\left(h_2h_3\boldsymbol{k}'^2 + \sigma_{e,2}\right)^{-1/2}. \end{aligned} \tag{6.24}$$

The solution of the eigenvalue problem, when a two mode interaction stability is considered, can be reduced to a dispersion relation of the 4-th order, that can be written as

$$\sum_{n=0}^{4} a_n\mu^n = 0. \tag{6.25}$$

The explicit solution can be obtained for the selected $\boldsymbol{k}_1$ and $\boldsymbol{k}_2$ mode interaction:

$$\mu = -\frac{\gamma}{2} \pm \left(\Gamma_{k_1k_2} + (\Delta^2_{k_1k_2})^{1/2}\right)^{1/2}, \tag{6.26}$$

where

$$\Gamma_{k_1k_2} = \frac{\gamma^2}{4} - \Omega^2_{k_1k_2}, \quad \Omega^2_{k_1k_2} = \frac{\omega^2_{k_1} + \omega^2_{k_2}}{2}, \quad \Delta^2_{k_1k_2} = \left(\frac{\omega^2_{k_1} - \omega^2_{k_2}}{2}\right)^2 - |G_{k_1,k_2}|^2. \tag{6.27}$$

In the frictionless case ($\gamma = 0$) the sufficient condition for the instability is

$$\Delta_{k_1k_2}^2 \leq 0. \tag{6.28}$$

If the stability is reached at a finite γ, then $\mathrm{Re}\{\mu\} > 0$ and (6.26) rewrites as

$$\mu = -\frac{\gamma}{2} \pm \left(\Gamma_{k_1k_2} \pm i|\Delta_{k_1k_2}|\right)^{1/2}. \tag{6.29}$$

In the case when the system is slightly above the instability threshold ($|\Delta_{k_1k_2}| \to 0$), the square root in (6.26) can be expanded in Taylor series, to find the fastest growing mode:

$$\mu = -\frac{\gamma}{2} + \Gamma_{k_1k_2}^{1/2} + \frac{1}{2}\Gamma_{k_1k_2}^{-1/2} i|\Delta_{k_1k_2}| + O(|\Delta_{k_1k_2}|^2). \tag{6.30}$$

For a small friction ($\gamma \to 0$) (6.30) reduces to:

$$\mu = -\frac{\gamma}{2} + i\Omega_{k_1k_2} + \frac{|\Delta_{k_1k_2}|}{2\Omega_{k_1k_2}}. \tag{6.31}$$

The system will be unstable if $\mathrm{Re}\{\mu\} \geq 0$, meaning that the friction coefficient

$$\gamma \leq \frac{|\Delta_{k_1k_2}|}{\Omega_{k_1k_2}}. \tag{6.32}$$

The explicit criterion for the instability is

$$\gamma \leq \left(\frac{2}{\omega_{k_1}^2 + \omega_{k_2}^2}\right)^{1/2} \left(|G_{k_1,k_2}|^2 - \left(\frac{\omega_{k_1}^2 - \omega_{k_2}^2}{2}\right)^2\right)^{1/2}. \tag{6.33}$$

Alternatively the stability condition (6.33) can be derived applying the Routh-Hurwitz [66] criterion to (6.25), giving the same expression as (6.33).

If the considered modes $\boldsymbol{k}_1$ and $\boldsymbol{k}_2$ are close enough ($\mathrm{Im}\{\mu_1\} \to \mathrm{Im}\{\mu_2\}$) then (6.33) reduces to

$$\gamma \leq \left(\frac{2}{\omega_{k_1}^2 + \omega_{k_2}^2}\right)^{1/2} |G_{k_1,k_2}|. \tag{6.34}$$

The results correlating the critical magnetic field B_z and the friction coefficient γ are depicted in the Figure 6.6. The same cell geometry as in the Section 6.3 and the material parameters from the Table 6.1 are used for the total electric current $I = 10^5$ A.

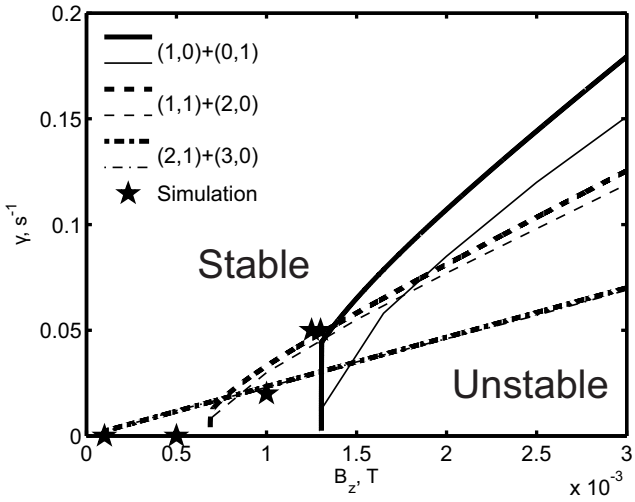

FIGURE 6.6: The critical stabilizing friction dependency on the magnetic field for two mode interaction: the thick lines from the asymptotic relations (6.33), the thin lines (6.26). The symbols $(\star)$ indicate representative numerical test cases shown in the Figure 6.8.

The asymptotic relation (6.33) gives a good approximation to the general expression (6.26), which is solved using the QZ algorithm from the standard, linear algebra software library LAPACK, except in the case of $(1,0)$, $(0,1)$ interaction with a relatively large gap between the unperturbed gravity frequencies (Figure 6.4). Note that discontinuity of stabilizing friction dependency on the magnetic field appears due to the critical magnetic field threshold, below which the two mode interaction will be always stable in the inviscid limit (mode collision will not happen at a lower field value). This is due to the condition (6.33) with the friction which contains also the condition: $\mathrm{Im}\left(\sqrt{|G_{k_1,k_2}|^2-(\omega_{k_1}^2-\omega_{k_2}^2)^2/4}\right)\neq 0$ to remain for the inviscid two mode stability [5]. Physically this means that a particular two mode interaction remains stable until a critical magnetic field is reached even in the inviscid case, however adding a small friction coefficient can stabilize this two mode interaction as it is graphically shown in the Figure 6.6. For this stabilization a finite value of the friction coefficient γ is needed, hence the curve in the Figure 6.6 'jumps' vertically to the respective value of the friction.

6.7 Numerical example

In order to demonstrate the validity of the 2-layer approximation vs 3-layer approximation of the batteries for a selection of materials ([67] the fully coupled numerical model of (5.25)-(5.27) and (5.64)-(5.65) taking into account the effect of the fluid flow was solved. The full coupled 3-layer solutions were compared to the decoupled 2-layer numerical solutions and respective linear stability results for the same cell geometry as in Section 6.3, when the total applied current is fixed at $I = 10^5$ A while the dissipation is neglected ($\gamma_1 = \gamma_2 = 0$).

The critical magnetic field dependency on the ratio of the density differences $(\rho_1 - \rho_2)/(\rho_2 - \rho_3)$ was analysed. The following approximations were compared: 1) linear stability for the 2-layer case, 2) linear stability for 3-layers, 3) decoupled 2 interface simulation, 4) fully coupled 3-layer simulation. The obtained results are summarized in the Figure 6.7. Overall a relatively good agreement between all approximations can be seen for the majority of material combinations (with the maximal difference of B_{cr} compared to the fully coupled 3-layer simulation less than $< 18\%$). When $(\rho_1 - \rho_2)/(\rho_2 - \rho_3) < 5$ the 2-layer linear stability overestimates the critical magnetic field, while the 2 interface simulation underestimates it. The 3-layer linear stability is in a reasonable agreement with the fully coupled 3-layer simulation except for the case $(\rho_1 - \rho_2)/(\rho_2 - \rho_3) \approx 1$, which corresponds to Li||Te battery. In this particular case 3-layer linear stability, predicts lower critical magnetic field value 0.365 mT if compared to the fully coupled approach giving $B_{cr} = 0.49$ mT, while the 2-layer linear stability and the decoupled 2 interface simulation gives 0.525 mT and 0.4 mT. The lowest critical magnetic field value is found for the Mg||Sb battery. This result emphasises the importance of the interfacial stability for this material combination. For this particular case the 2 and 3-layer linear stability predict $B_{cr} = 0.135$ mT; the numerical simulations for the decoupled 2 interfaces gives 0.125 mT and the fully coupled case results in 0.135 mT critical value respectively. With decrease of the density ratio all four approximations predict increase of the critical magnetic field value except the Na||Sn battery. For this case a drop of the critical magnetic field is observed. This appears due to the lower density difference between the electrolyte and the upper metal $\rho_2 - \rho_3 = 1619$ kg/m^3 if compared to the density differences in

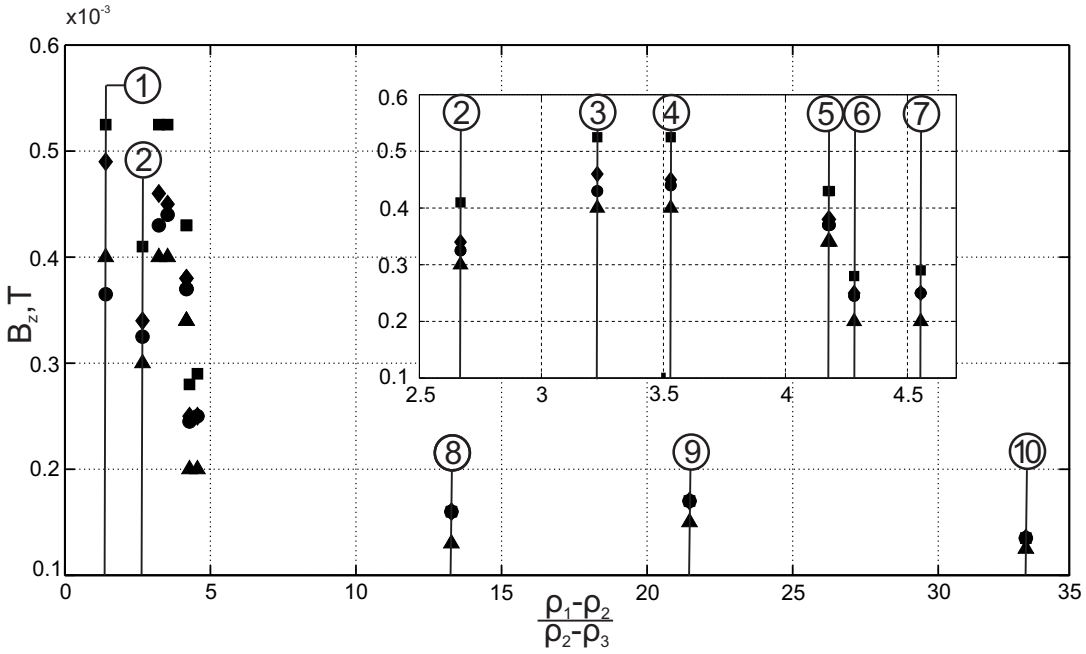

FIGURE 6.7: Critical stability comparison for different battery compositions: (■) linear stability for the 2-layers, (●) linear stability for the 3-layers, (▲) decoupled 2 interface simulation, (♦) fully coupled 3-layer simulation. 1) Li||Te, 2) Na||Sn, 3) Li||Bi, 4) Li||Pb, 5) Na||Bi, Na||Pb, 6) Li||Zn, 7) Li||Sn, 8) Ca||Sb, 9) Ca||Bi, 10) Mg||Sb.

the Li||Te and Li||Bi, which are 2201 and 2202 kg/m^3 respectively.

Based on the findings that the top 2-layer model is a good approximation to LMB stability for the majority of the practically important cases of material selection, it attempted to compare the LMB case against existing numerical model MHD-VALDIS for aluminium electrolysis cell which was previously validated against experiments [37, 68]. The model was adjusted for the cell geometry given in the Section 6.3, and for the material properties given as in the Table 6.1. In order to model a liquid metal battery cell two cases based on the aluminium reduction cell were used to describe the two interface interaction. The upper interface of the cell is represented by inverting the gravity direction (effectively moving the electrolyte from the bottom to the top of liquid metal). For the lower interface description the direction of the gravity remains down ward as in normal case. An additional adjustment was required to include numerically the electric current redistribution when accounting for the bottom interface presence. In the Mg||Sb case the lower interface is nearly flat and the MHD stability of the upper interface is hydrodynamically uncoupled. The model permits inclusion of the wave dissipation effects given by the friction coefficient γ as in the linear theory. The initial perturbation of the mode $(1,0)$ of amplitude $A = 0.005$

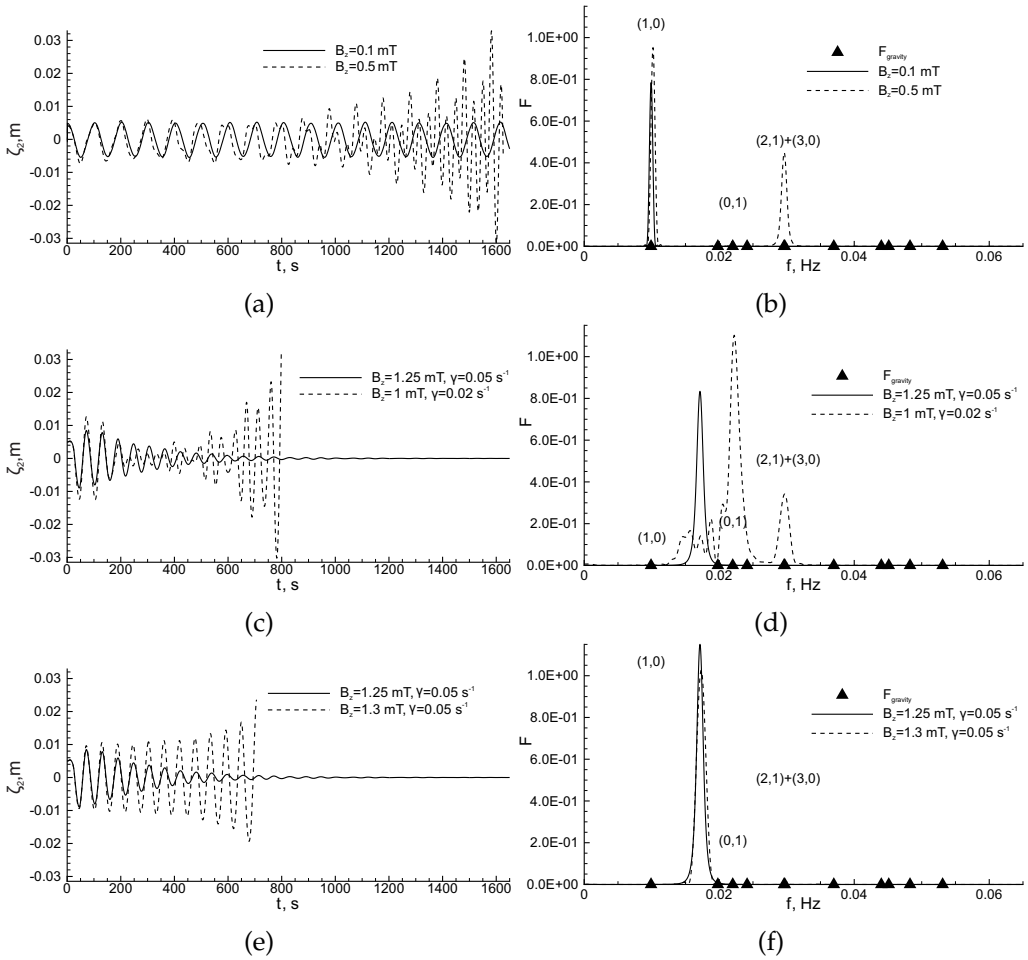

FIGURE 6.8: Numerical results for the top interface oscillation at a fixed position ($x = 0, y = 0$) following the initial $(1,0)$ mode perturbation at $A = 0.005$ m: a) oscillation in the frictionless case ($\gamma = 0$) for subcritical and overcritical magnetic fields, b) the power spectra for $\gamma = 0$ cases, the black triangles mark the gravity wave frequencies, c) oscillation in the presence of friction , d) the power spectra for two friction coefficients at the marginally stable and unstable cases, e) oscillation at higher friction ($\gamma = 0.05$ s^{-1}) for B_z near stability limit, f) the spectral peaks near the stability limit.

m and the total electric current $I = 10^5$ A was used in all cases. In the frictionless case ($\gamma = 0$) at low magnetic field $B_z = 0.1$ mT the $(1,0)$ sloshing wave is continuously oscillating at the same frequency without signs of significant growth or damping, see Figure 6.8 (a,b). The MHD interaction of the waves becomes unstable at $B_z = 0.5$ mT after a large number of oscillation cycles as shown in Figure 6.8 (a). The Fourier transform of the computed wave amplitude time dependence indicates that the instability sets in due to the $(2,1) + (3,0)$ mode interaction for this particular cell, Figure 6.8 (b). These results show the advantage of using the coupled fluid dynamic stability analysis over the purely mechanical solid plate model [48]

which predicts a significantly higher stability level ($B_{cr} = 11$ mT). This conclusion is confirmed independently by the numerical simulations in [52].

After adding the friction coefficient with empirical value $\gamma = 0.05\ \mathrm{s}^{-1}$, which is close to the typical value $(0.02 - 0.08)\ \mathrm{s}^{-1}$, used for commercial aluminium reduction cells [69], the cell becomes unstable at $B_z = 1.3$ mT. The transition to the instability is rather sensitive to the B_z value, as can be seen from the Figure 6.8 (e,f) showing the oscillation with the damped oscillation for $B_z = 1.25$ mT. For a lower B_z the damping is dominant, for a higher B_z the growth rate increases: at $B_z = 1.5$ mT it takes only 97 seconds for the wave to breach the middle layer and short circuit the cell. The typical wave snapshots at the late stage of development are shown in the Figure 6.9, 6.10. The four frames shown at intervals of approximately a quarter of the period ($T_{(2,1)} \approx 33.71$ s) are demonstrating a more complex wave rotation pattern than a typical rotating wave along the whole cell perimeter. The instability threshold at $\gamma = 0.02\ \mathrm{s}^{-1}$, $B_z = 1$ mT found from the numerical wave evolution simulation matches the instability onset according to the analytical criterion (6.33) (see the Figure 6.6).

The other transition to instability when the longitudinal mode $(1,0)$ interacts to $(0,1)$ transversal mode in Figure 6.10 is reached at a higher friction $\gamma = 0.05\ \mathrm{s}^{-1}$ and $B_z = 1.3$ mT according to the analytical criterion (6.34) or (6.26), as deduced from the Figure 6.6. This is confirmed by the direct numerical wave evolution simulation as shown in the Figure 6.8 (e). The corresponding "rotating" wave frames are shown in the Figure 6.10. The mode $(1,0)$ and $(0,1)$ interaction occurs at the shifted oscillation frequency $\mathrm{Im}\{\mu\} = f$ located between the original gravity wave frequencies, see the Figure 6.8 (f).

In the following chapter double-interface simulation is validated, against a fully coupled 3 layer simulation for the 3D magnetic field. Afterwards, the interfacial stability in two possible large scale battery types: non-optimized (the single collector cell) and an optimized (the multiple collector cell) is compared.

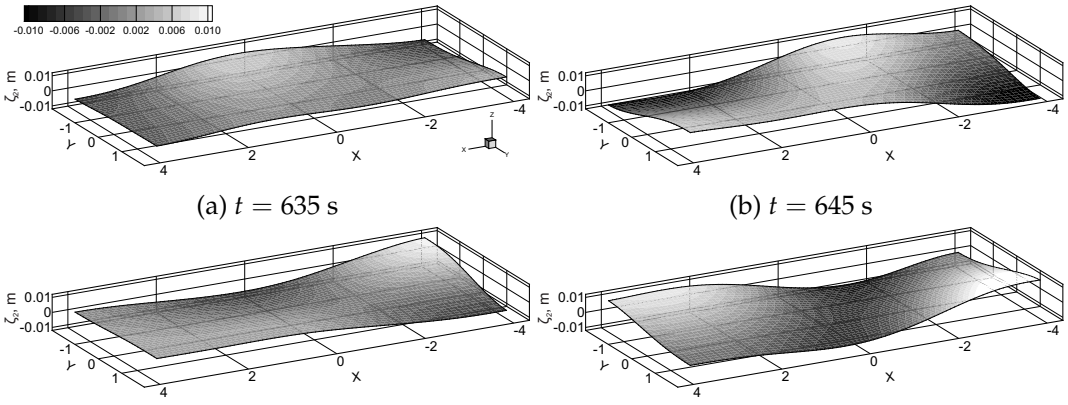

(a) $t = 635$ s (b) $t = 645$ s

(c) $t = 655$ s (d) $t = 665$ s

FIGURE 6.9: The computed interface of growing amplitude with the friction $\gamma = 0.02$ and $B_z = 1$ mT. The frames at 10 s illustrate the $(1,0) + (0,1)$ and $(2,1) + (3,0)$ mode interactions.

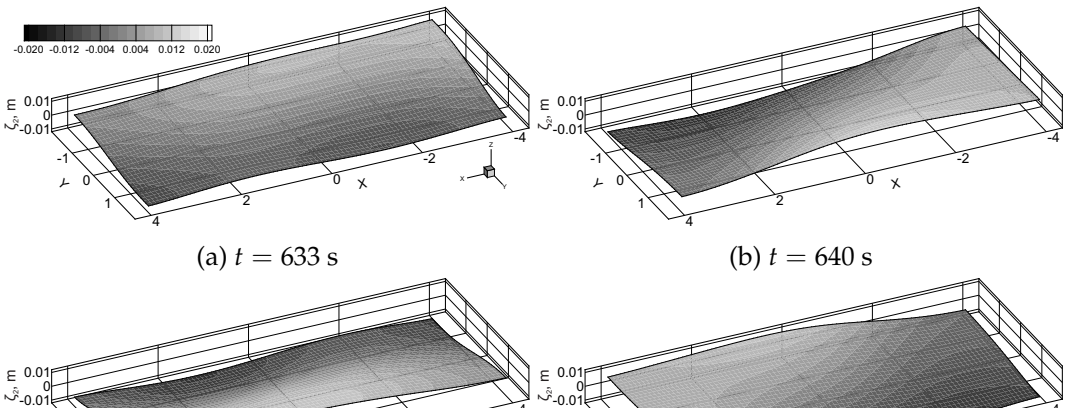

(a) $t = 633$ s (b) $t = 640$ s

(c) $t = 660$ s (d) $t = 668$ s

FIGURE 6.10: The computed interface of growing amplitude with $\gamma = 0.05$ and $B_z = 1.3$ mT. The frames show the $(1,0) + (0,1)$ mode interaction.

Chapter 7

Wave dynamics for more realistic battery cases

7.1 Overview

In this chapter a decoupled 2 interface simulation is compared, with the fully coupled 3-layer simulation for the given 3D magnetic field case of Mg||Sb battery. This provides additional confidence in the decoupled 2 interface approximation to describe two possible large scale battery types: with the non-optimized (the single collector cell) and the optimized (the multiple collector cell which corresponds to the commercial Trimet 180 kA cell series [37, 70]) magnetic field distribution.

7.2 3D magnetic field effect on the stability of LMB

Magnetic field distribution in the battery is defined by the full path of the electric current: arrangement of the bus-bars and the neighbouring batteries, the return line, as well as the steel magnetization in cell construction as in the HHC. Figure 7.1 (a) shows time averaged 3D magnetic field distributions for two battery bus-bar cases: non-optimized (Figure 4.3) and optimized (Figure 4.5). For these given magnetic field distributions the computed Mg||Sb system stability was analysed by means of fully coupled 3-layer simulations. A small-amplitude $A = 0.005$ m gravity wave of mode $(1, 0)$ was used as initial perturbation for both interfaces. The cell stability for two magnetic fields was compared for the case when the metal electrode thicknesses $h_1 = h_3 = 0.2$ m, the electrolyte $h_2 = 0.05$ m, and the applied electric current

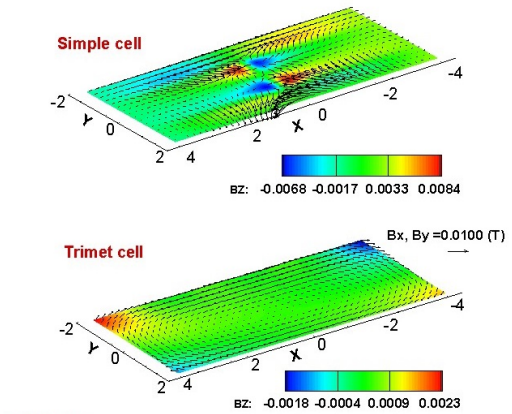

(a) Comparison of the magnetic field at 75 kA current for the non-optimized cell vs the optimized cell

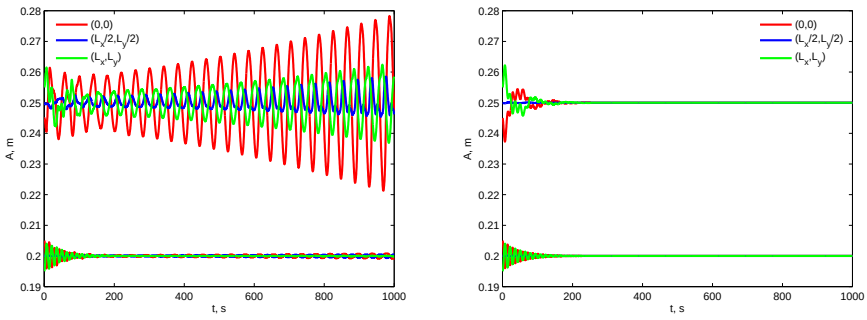

(b) Non-optimized cell

(c) Optimized cell

FIGURE 7.1: Comparison of the interfacial oscillations at fixed positions for $I = 75$ kA, $h_{1,3} = 20$ cm, $h_2 = 5$ cm for the two magnetic field cases.

$I = 75$ kA. The computed results of the interfacial motion are presented in the Figure 7.1 (b,c). As it can be seen, unstable interfacial motion develops in the cell with non-optimized magnetic field, however, in the case of the optimized magnetic field all oscillations are damped. Results demonstrate that the bottom, heaviest, metal interface is very stable to the perturbation effects, while the top metal interface is easily destabilized, leading to wave amplitude growth and the development of an unstable wave motion. The computed sequence of the interface shapes for the unstable cases are presented in the Figures 7.2, 7.3. The cell with optimized magnetic field becomes unstable at a significantly lower electrolyte thickness $h_2 = 0.02$ m, and higher total current $I = 100$ kA ($h_1 = h_3 = 0.1$ m). The destabilisation mechanisms are considerably different from the previously analysed linear rotating wave instability for the cases with purely vertical and uniform magnetic field distribution. The system with the optimised field distribution retains stability for a lower electrolyte

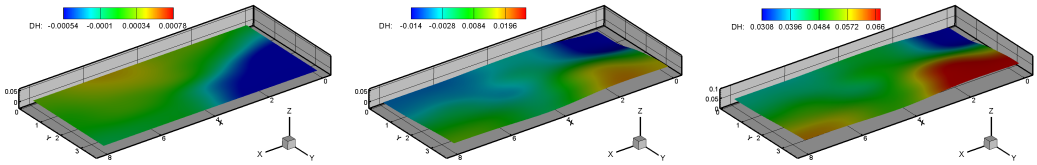

(a) Lower metal at $t = 968$ s (b) Upper metal (c) Electrolyte thickness.

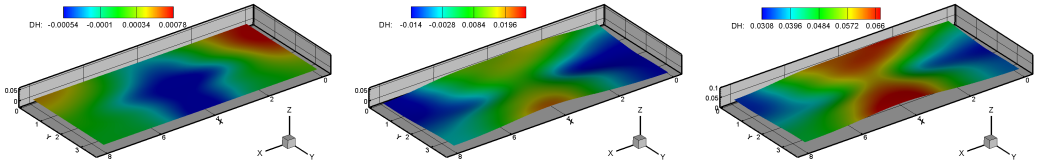

(d) $t = 977.2$ s (e) (f)

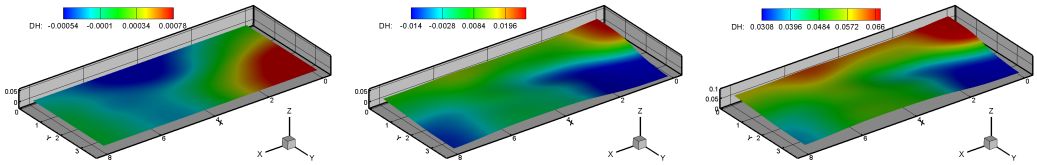

(g) $t = 987$ s (h) (i)

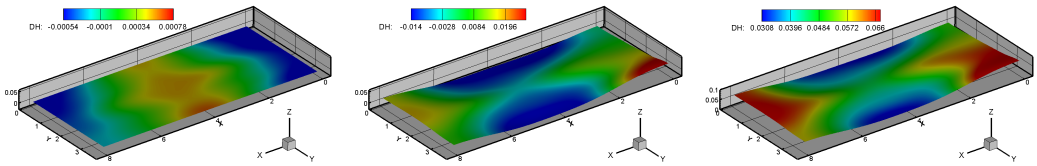

(j) $t = 999.2$ s (k) (l)

FIGURE 7.2: The computed interfaces of growing amplitude for the cell with non-optimized magnetic field distribution at $I = 75$ kA, $h_{1,3} = 20$ cm, $h_2 = 5$ cm.

thickness and higher current. More detailed examination will be provided in the following sections.

Decoupled 2 interface simulations were compared with fully coupled 3-layer

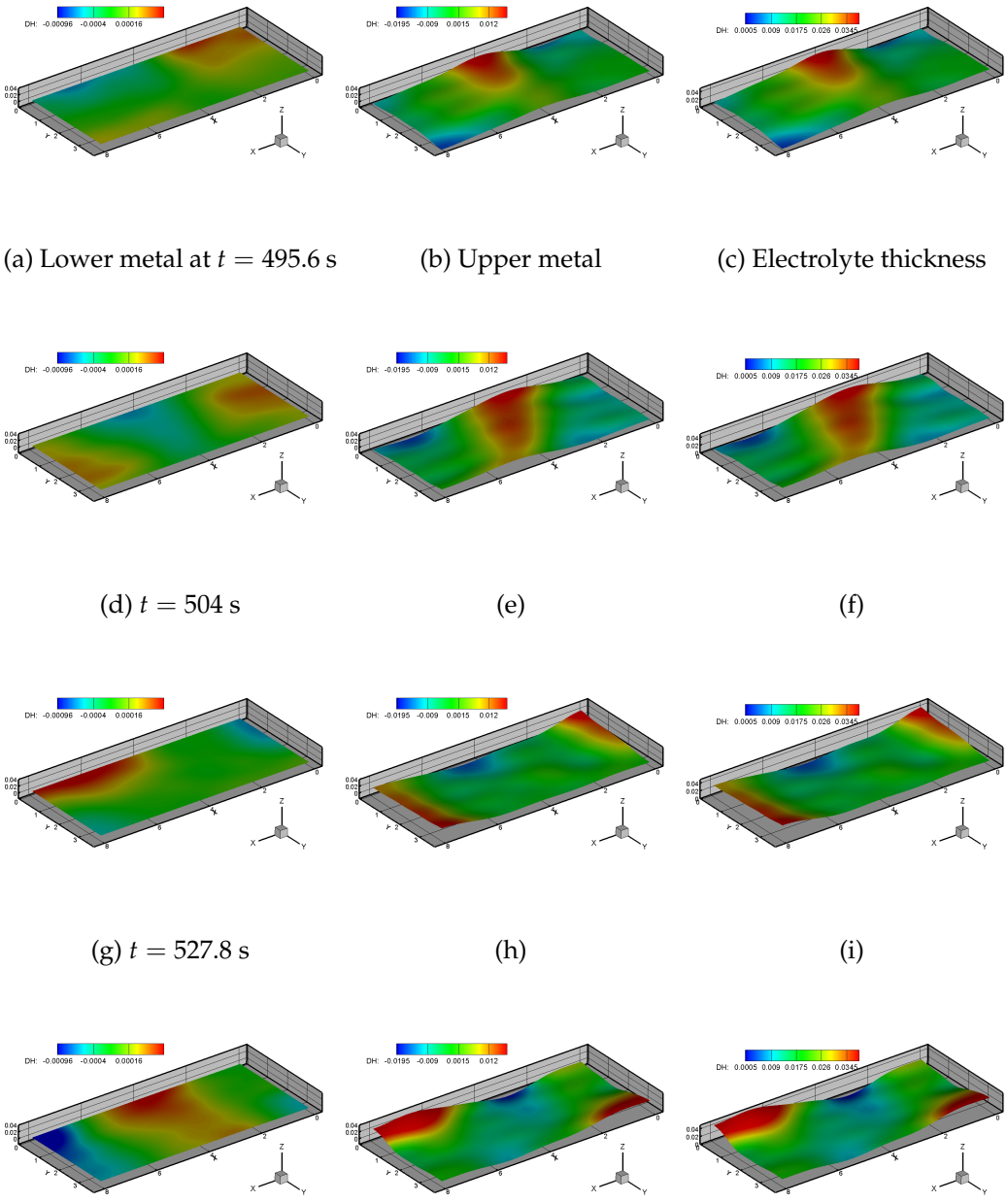

(a) Lower metal at $t = 495.6$ s (b) Upper metal (c) Electrolyte thickness

(d) $t = 504$ s (e) (f)

(g) $t = 527.8$ s (h) (i)

(j) $t = 540.8$ s (k) (l)

FIGURE 7.3: The computed interfaces of growing amplitude for the cell with optimized magnetic field distribution at $I = 100$ kA, $h_{1,3} = 10$ cm, $h_2 = 2$ cm.

simulation for the cell with non-optimized magnetic field. Stable and unstable interfacial dynamics cases were considered. The results are shown in Figure 7.4 and 7.5. When the total current $I < I_{cr}$ system remains stable. The corresponding Fourier spectra are indicating the single low energy peak. The difference between the two

approximations is negligible, see Figure 7.4 (a,c,e,g). For the case when $I \geq I_{cr}$ an unstable interfacial motion is induced. In the latter case Fourier spectra are matching quiet well, both indicating a single resonance peak of the instability. Both approximations predict very similar onset of the instability and a decrease in the local thickness of the electrolyte, see Figure 7.4 (b,d,f,h). Overall conclusion is that the decoupled 2 interface approximation is sufficient for the stability analysis of the system when $\rho_1 - \rho_2 \gg \rho_2 - \rho_3$.

Figure 7.6 provides an example of the coupling between different physical phenomena in the battery when magnetic field is non-optimized. Interfacial variations lead to the redistribution of the electric current in the layers. Changes in the electric current distribution leading to the changes of Lorentz forcing in the system and the modification of the flow structures. Change in the fluid flow influences the dynamics of the interfaces.

The existing code MHD-VALDIS which was originally developed for HHC description was adjusted for the LMB application. It was also used in the previous Chapter 6 for the linear stability result validation and is equivalent to the decoupled 2 interface simulation model. An advantage of this code is its ability to account for different electric current collector configurations, as well as time variable distribution of the full magnetic field in the system including the full path of the electric current and the surrounding cells with the return current line.

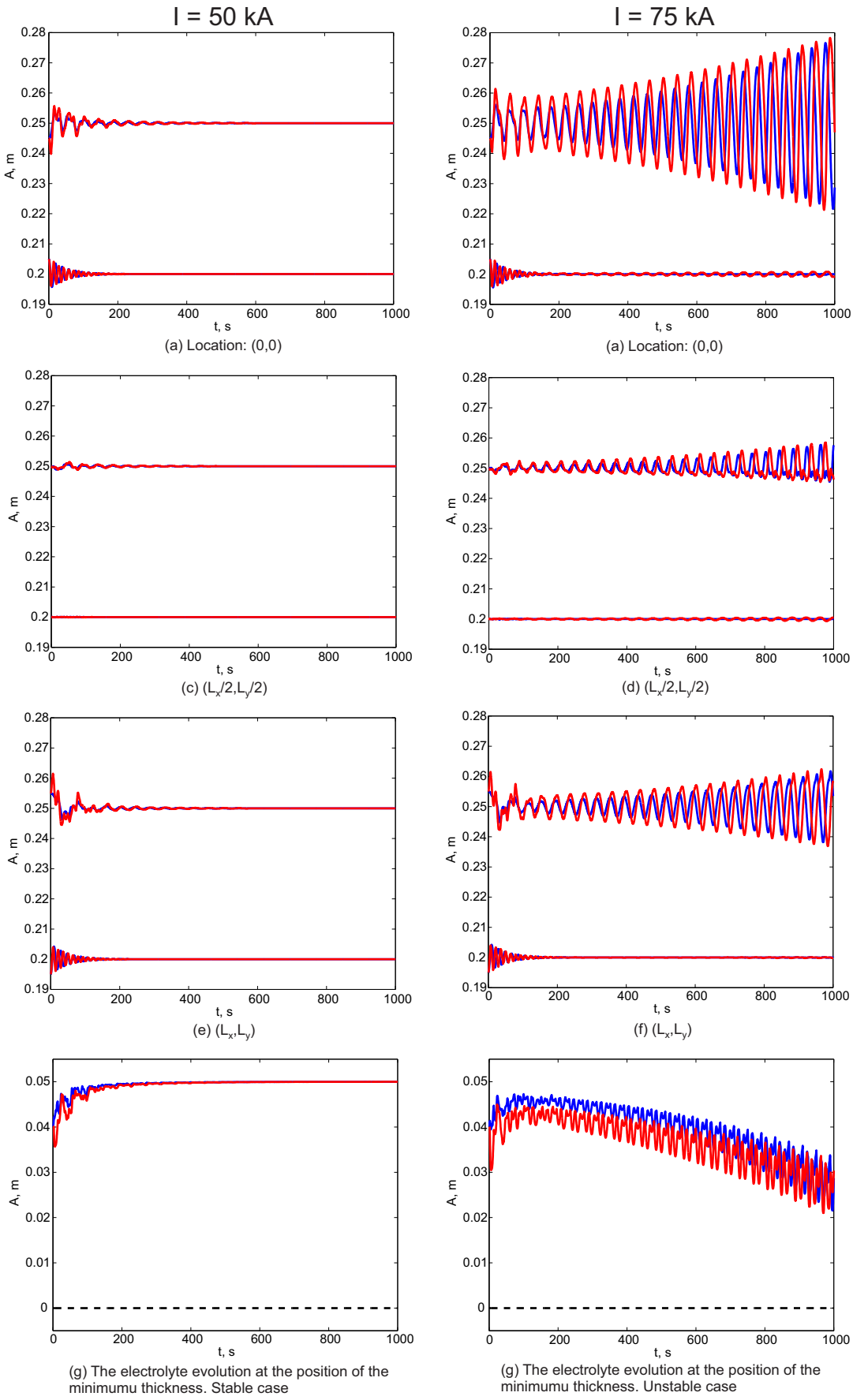

FIGURE 7.4: Interfacial oscillation at a fixed position comparison of the decoupled (blue line) and fully coupled (red line) approximation for the non-optimized cells magnetic field distribution ($h_{1,3} = 20$ cm, $h_2 = 5$ cm).

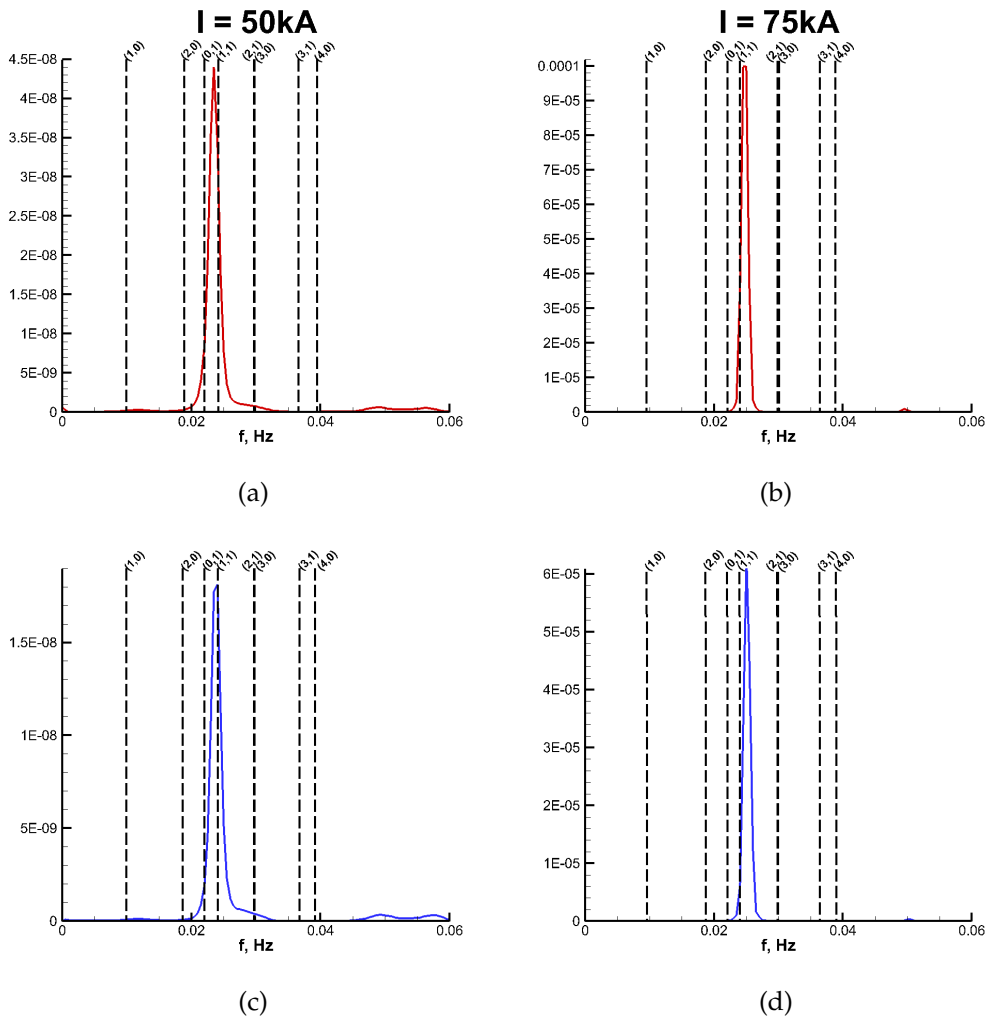

FIGURE 7.5: Comparison of the computed spectra of the decoupled (blue line) and fully coupled (red line) models for the non-optimized magnetic field ($h_{1,3} = 20$ cm, $h_2 = 5$ cm).

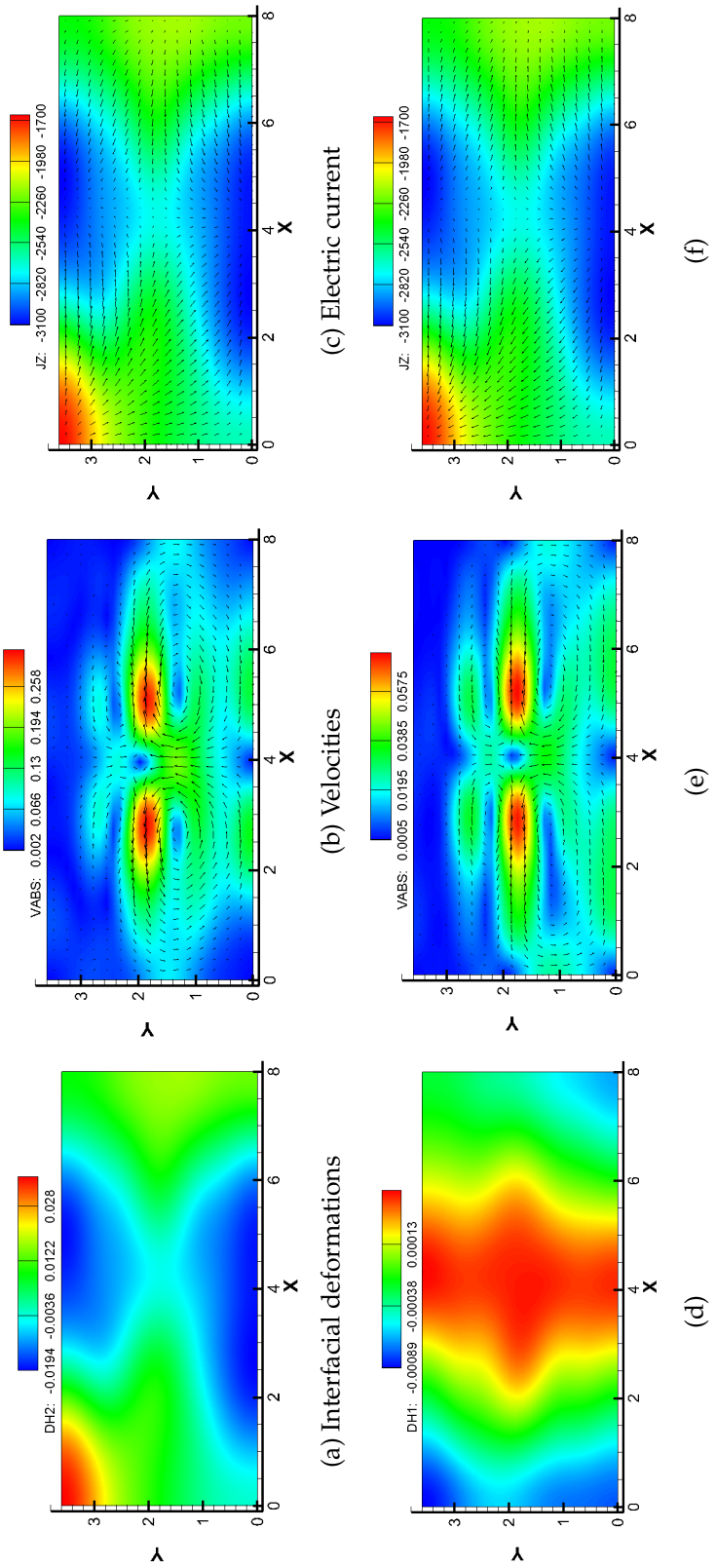

FIGURE 7.6: Example of the multiphysical coupling in the cell with non-optimized magnetic field when $I = 75$ kA, $h_2 = 5$ cm, $t = 999.2$ s. The lower row corresponds to the lower metal, the upper row corresponds to the upper metal.

7.3 Full interaction with 3D magnetic field

In this section the impact on the stability of LMB of full magnetic field created by the complete path of electric current will be analysed. Two cases will be considered: the single collector cell and the multiple collector cell. The ohmic voltage loss will be minimized by reducing the electrolyte depth while preserving the magnetic stability.

7.3.1 Single collector battery

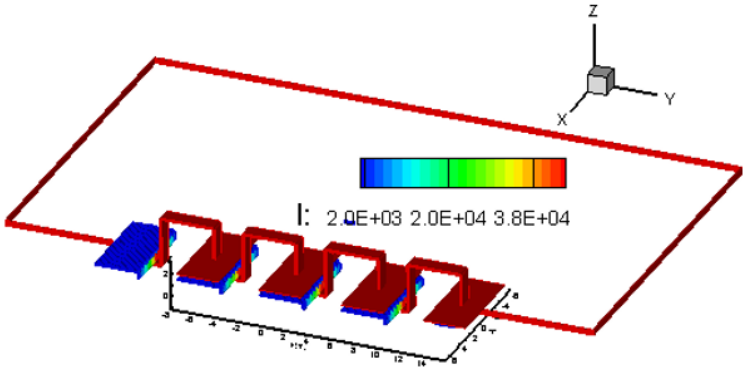

FIGURE 7.7: Schematic representation of the single collector battery.

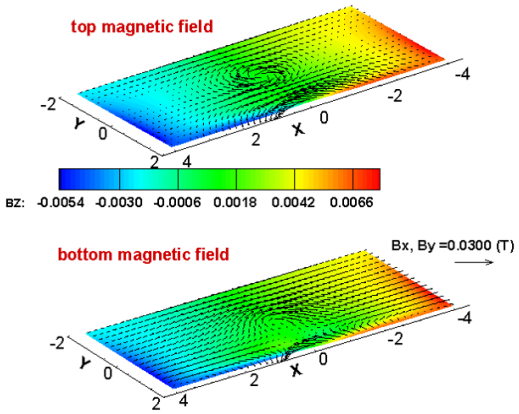

FIGURE 7.8: Magnetic field distribution in the two metal electrodes for the single collector battery ($I = 50$ kA and $h_2 = 5$ cm).

A selection of computed results for the time dependent flow and interface wave development is presented for the case of Mg||Sb battery. A small amplitude $A = 0.005$ m gravity wave of mode $(1, 0)$ was used as initial perturbation for both interfaces. Horizontal cavity contain 20 cm of liquid Sb, 20 cm of liquid Mg, and 5 or 8 cm of the liquid electrolyte. The electric current $I = 100$ kA is supplied by a single central collector from the top and removed at a one sided collector at the bottom, more detailed description is provided in the Chapter 4, see also Figure 4.4, 7.7. The

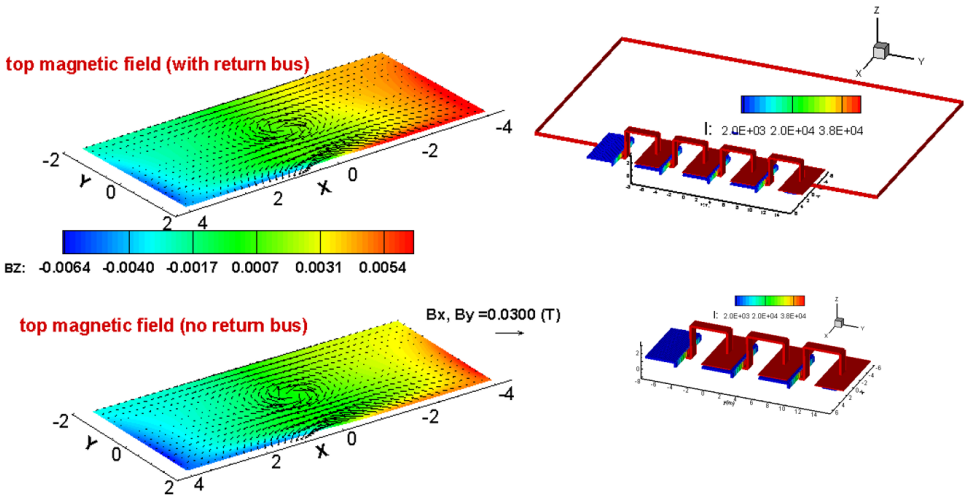

FIGURE 7.9: The return circuit effect on the magnetic field distribution in the top metal ($I = 50$ kA and $h_2 = 5$ cm).

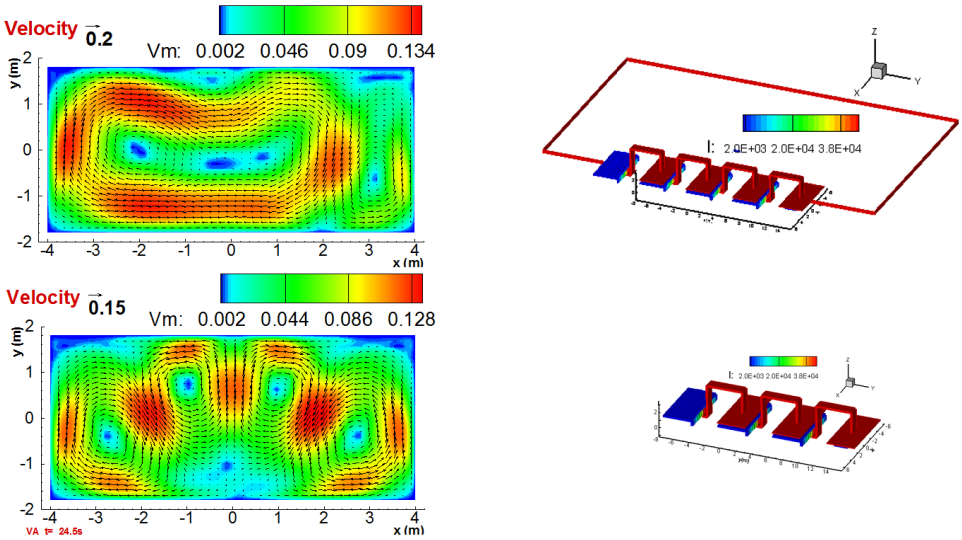

FIGURE 7.10: The return circuit effect on the velocity field distribution in the bottom metal ($I = 50$ kA and $h_2 = 5$ cm).

distribution of the full magnetic field in the layered system depends on the full path of the electric current including the surrounding cells and the return current line. The existing code MHD-VALDIS developed for HHC description and optimisation [37], was used to account these effects. The previous agreement between the decoupled 2 interface and fully-coupled 3-layer numerical models allows to consider the interfacial dynamics in the system.

The magnetic field distribution in the system was analysed first. The Figure 7.8 shows time averaged magnetic field distributions in the metal electrodes. As it can be seen, the distributions slightly differ in the both layers, however are qualitatively the same. The magnetic field distribution is also influenced by the return line presence, see the Figure 7.9. As a consequence of that elecromagnetic force distribution

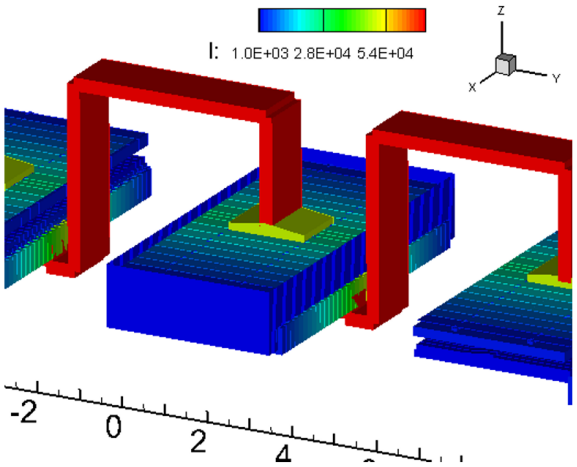

FIGURE 7.11: Schematic representation of the single collector battery with rearranged current connector, with added ferromagnetic box.

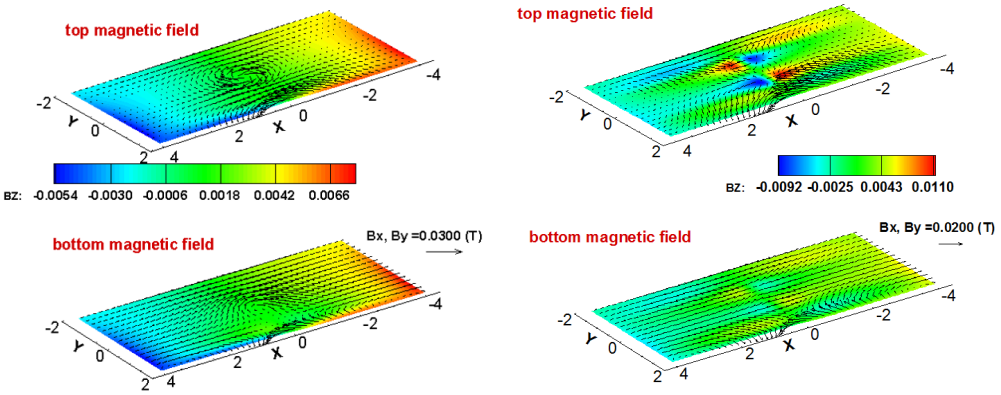

(a) Single small area collector.

(b) Single wide collector.

FIGURE 7.12: The effect of the steel box on the magnetic field distribution in the top metal ($I = 50$ kA and $h_2 = 5$ cm).

changes and as a result generated EVF structures are modified, see the Figure 7.10. The symmetric flow pattern becomes less structured. These results emphasise the important contribution of the magnetic field components generated by the return line. All of the following results in this and the following section are obtained taking into account the impact of the return line.

A common way to control the magnetic field distribution in the HHC is by means of the current connector optimization and construction steel magnetization. This strategy can be also applied to LMBs. In Figure 7.12 it is shown how the magnetic field distribution can be modified by the rearrangement of the current connector and an added steel box (see Figure 7.11). The changes in the distribution are quite

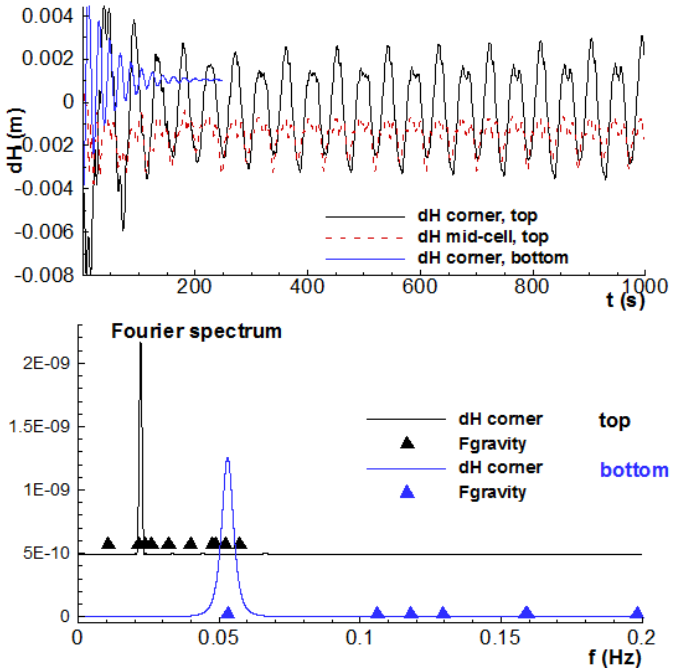

FIGURE 7.13: Oscillation patterns for top and bottom metal/electrolyte interfaces and the computed Fourier spectra for $I = 100$ kA and $h_2 = 8$ cm [38].

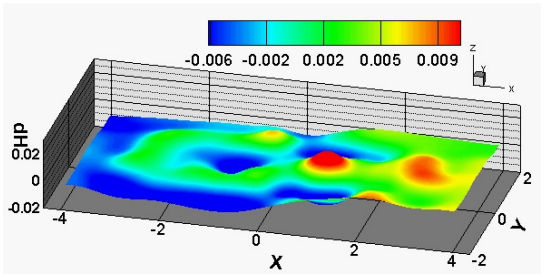

(a) The top metal interface.

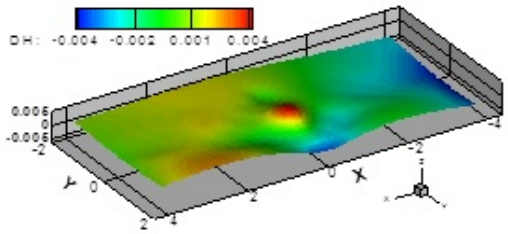

(b) The bottom metal interface.

FIGURE 7.14: The final computed stable interfaces for the single collector cell ($I = 100$ kA and $h_2 = 8$ cm) [38].

significant, and as it will be demonstrated in the following subsection with the magnetically optimized cell example they can be crucial for the interfacial stability.

Long term simulation of the wave dynamics with fully coupled electromagnetic interaction was performed and results for interfacial dynamics were obtained shown in the Figure 7.13, 7.14. Similarly to previous examples results indicating that the

bottom metal interface is very stable, while the top metal interface is easily destabilized. The cell response can be stabilised by reducing the magnitude of the total current (from 100 to 75 kA) or by increasing the electrolyte thickness from 5 cm to 8 cm.

7.3.2 Multiple collector battery

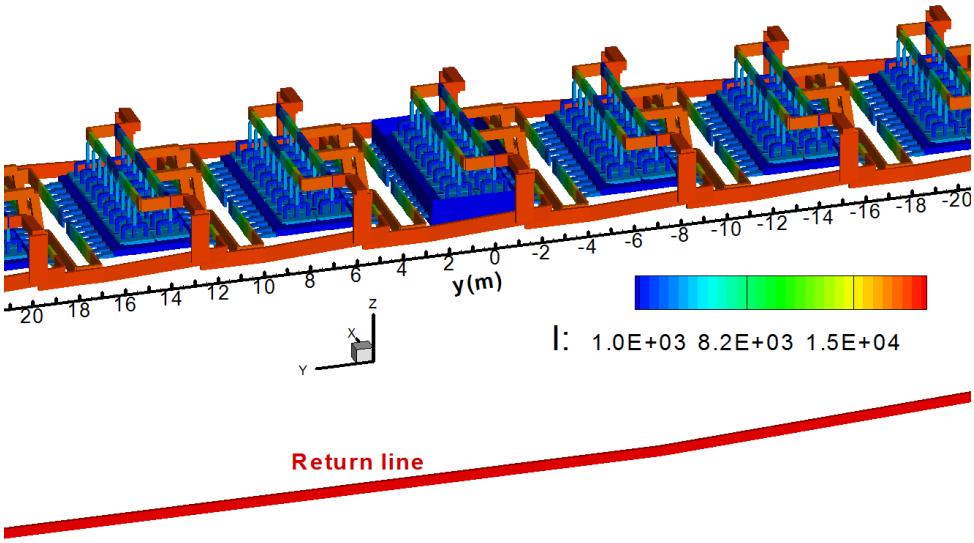

FIGURE 7.15: Schematic representation of the optimized collector cell (Trimet).

In the previous example with the single collector supply the cell could be stabilized for the MHD effects only at relatively high electrolyte thickness (5 or 8 cm), meaning that the ohmic voltage drop at the 100 kA current is far exceeding the thermodynamic EMF available for the Mg||Sb battery in the discharge period (about 0.4 V [1]). It would be possible to operate this battery at significantly lower current at low efficiency. An improvement of efficiency can be achieved by optimizing the current supply bus-bar path in such a way that the vertical magnetic field is reduced in magnitude and its distribution optimized to avoid the MHD wave instability. The commercial aluminium electrolysis cells were developed following such stringent guidelines. Hence, it was attempted to keep one of the bus bar configurations for the case of 3 liquid layers filling the cell cavity. The considered configuration is shown in the Figure 7.15. The magnetic field distribution comparison for the optimized multiple collector cell and the the non-optimized one is shown Figure 7.1 (a). The magnetic field B_z component magnitude is much less for the multiple collector

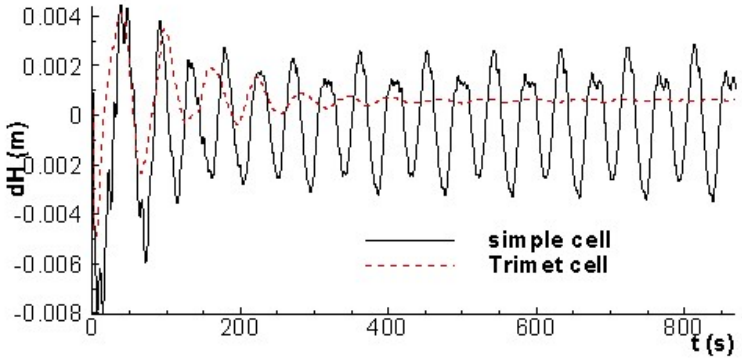

FIGURE 7.16: The non-optimized cell ($I = 100$ kA, $h_2 = 8$ cm) versus the optimized cell ($I = 100$ kA, $h_2 = 2.5$ cm) top metal oscillation [38].

cell at the same value of the total electric current. In this case the electric current in the liquid layers has smaller horizontal component, particularly in the longer dimension x, as it was demonstrated in the Chapter 4 about the 3D current flow, see the Figure 4.6. From the Figure 4.6 it can be seen that the 0.65 V voltage drop is too high for the 0.4 V discharge current to be driven by the battery EMF. Therefore the current needs to be reduced to 75 kA.

The wave stability for the two cells was compared. At 100 kA the single collector cell was stabilized if the electrolyte thickness was increased to 8 cm. In contrast the optimized multiple collector cell holding three metal layers appears to be more stable even if reducing the electrolyte thickness to 2.5 cm (Figure 7.16). The voltage drop in the electrolyte is still too high (0.49 V) for the discharge to be feasible, however this combination of the current and electrolyte thickness could be used in the dynamic charging periods when the external circuit current is subject to high fluctuation. For the stable discharge at reasonable voltage drop of 0.29 V the current can reach 75 kA and the electrolyte thickness is reduced to 2 cm. In this case to optimize required volume of the battery the metal layer thickness can also be reduced safely to 10 cm. A further reduction of the current magnitude to 50 kA reduces the ohmic voltage drop to 0.19 V.

The computed interface deformations become stable and smaller in magnitude after the perturbation dies out, see Figure 7.17 (a,b). The bottom metal interface is very stable, the perturbation is damped fast while oscillating at the initial gravity wave frequency, without any shift due to the MHD interaction. The top metal even for the stable case of 75 kA shows the presence of the magnetic interaction by shifting

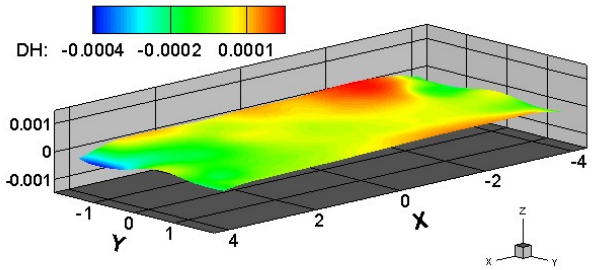

(a) The top metal interface.

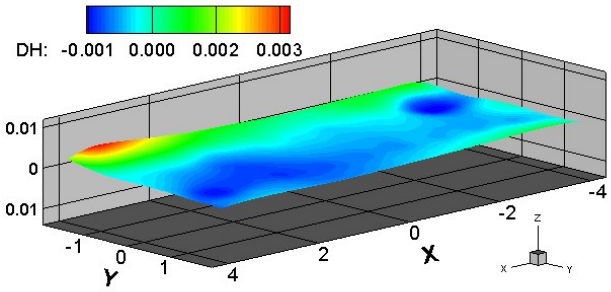

(b) The bottom metal interface.

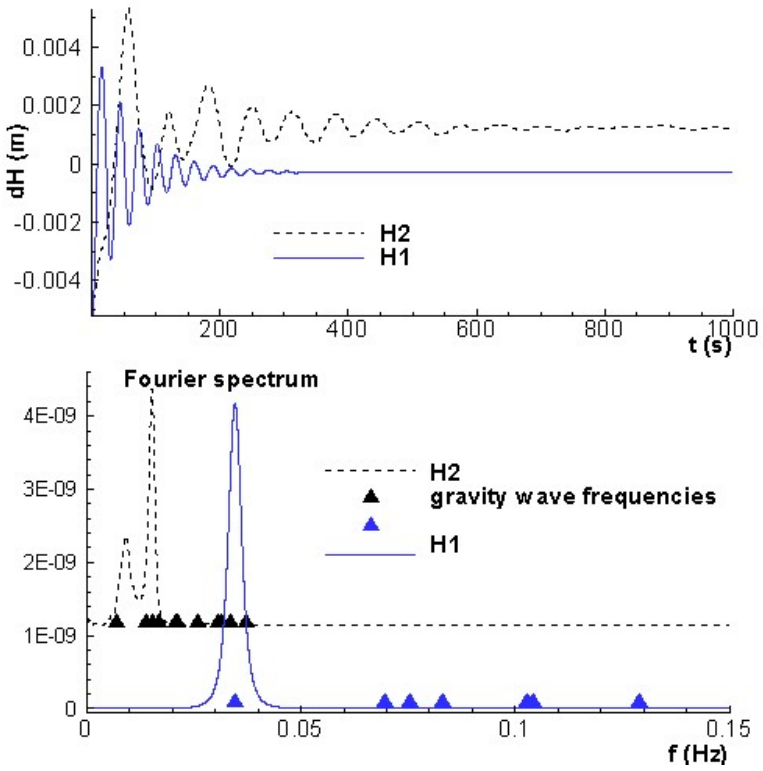

(c) The bottom metal interface.

FIGURE 7.17: The final computed stable interfaces for the multiple collector cell ($I = 75$ kA and $h_2 = 2$ cm) [38].

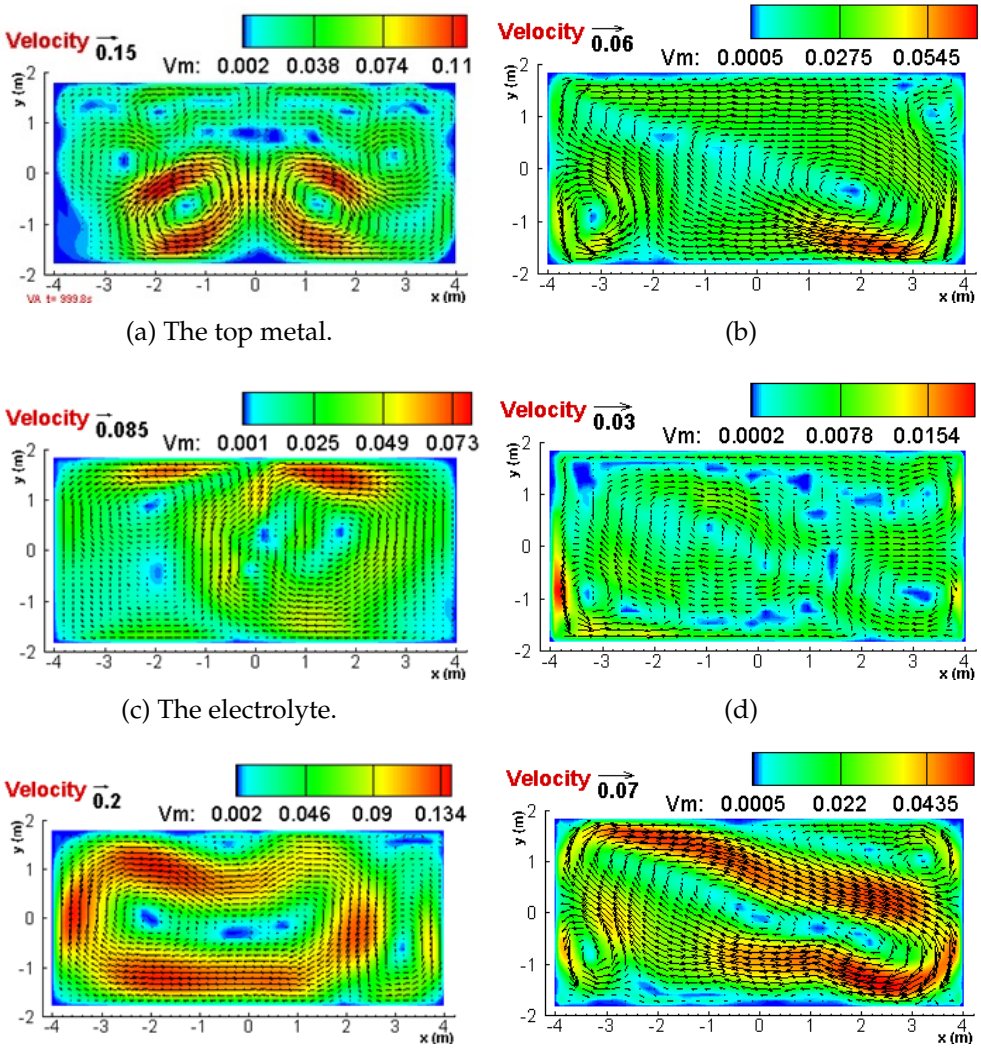

(a) The top metal. (b)

(c) The electrolyte. (d)

(e) The bottom metal. (f)

FIGURE 7.18: Velocity distribution in positive electrode, electrolyte and negative electrode for the single collector battery (on the left) at $I = 50$ kA with $h_2 = 5$ cm and the multiple collector battery (on the right) at $I = 75$ kA with $h_2 = 2$ cm [38].

the oscillation frequencies of the two modes, which are initiated from the single mode $(1, 0)$ perturbation, as it is illustrated in Figure 7.17 (c).

The results for mixing velocities for both cells are compared in the Figure 7.18. As it can be seen, the most intensive motion appears in the upper electrode layer, which is an expected outcome due to the layer's high electrical conductivity. Liquid motion is present also in the electrolyte layer in spite of the low conductivity, mainly due to the momentum transfer from the liquid electrodes through the interfacial stress continuity. The horizontal velocities for the multiple collector cell are reduced in magnitude compared to the single collector one.

Chapter 8

Research Summary and Further Work

8.1 Research Summary

This section summarises the most important outcomes of the research.

1. A mathematical model for three density-stratified electrically conducting liquid layers is derived starting with a full 3D formulation, then introducing the shallow water approximation for high aspect ratio batteries to take into account specific MHD effects during periods of battery charge/discharge. The analogy of the aluminium electrolysis cell is used for this.

2. A linear stability model for the interface wave analysis has been derived and implemented. The most important outcomes of the model simulations are:

    - For the selection of liquid materials most suitable for practical implementation, the interface between the lower metal and the electrolyte is significantly more stable than the interface between the electrolyte and the top (lighter) metal.
    - Similarly to the Hall-Heroult cells the most dangerous mode interactions are the combination of the long waves characterised by the mode numbers (1,0)+(0,1); (1,1)+(2,0).
    - The analytical estimate for the laminar dissipation rate in the 3-layer system is derived. Purely laminar viscous dissipation is insufficient for the

long wave stabilization. Turbulent effective dissipation is required appropriate for the Reynolds number.

- The analytical stability criterion for dissipation rate is derived for different interaction cases, accounting for the cell aspect ratio, the liquid layer electrical conductivities and thicknesses. The derived criterion gives a good match for the instability onset, with numerical solutions available for the aluminium electrolysis cells.
- The 2-layer approximation is sufficient in the most of the considered cases for stability prediction of the batteries, due to the insensitivity of the heavy bottom layer.

3. A fully coupled 3-layer numerical model was also developed. It is well suited for analysis of the following situations: interaction of the background melt flow and the interface deformations, for spatially complex, time-dependent distribution of the base electric current and magnetic field. The main outcomes of this part are:

   - The instability caused by the interaction between the externally generated vertical magnetic field and horizontal electric current perturbations associated with the interface deformations is analysed. The growing perturbations have the form of rotating, large-scale interfacial waves. The instability mechanism is similar to the mechanism of the rolling pad instability known for the aluminum reduction cells.
   - In the case when the density difference at upper interface is much larger than the density difference at the lower interface, only the upper interface is significantly deformed in the course of the perturbation growth. The behaviour is then similar to that of aluminium reduction cells. The instability onset matches very well with linear stability model results for 2-layers and 3-layers (e.g. Li||Bi, Na||Bi, Ca||Sb, Ca||Bi, Mg||Sb batteries).
   - In the case when the density differences at the two interfaces are comparable, both interfaces are significantly deformed, and the behaviour of the system is more complex and quite different from that of a Hall-Heroult cell. The two interfacial waves can be coupled either symmetrically or

antisymmetrically depending on the phase shift between the waves at the initial moment. The presence of the second deformable interface has a stabilizing effect (e.g. Li||Te battery).

- A 3D numerical model for the electric current flow in the LMB with arbitrary geometry is derived and implemented. The model is the alternative optimization tool for the current collector arrangement.

4. Two LMB design cases were considered for a possible practical implementation: the single collector cell (non-optimized) and the multiple collector cell (optimized).

   - The MHD model results demonstrate that it is possible to design a stable to dynamic perturbations operating cell, by using an optimized bus bar configuration.
   - The magnetically optimized battery exhibits much better stability characteristics compared to the non-optimized battery. The optimized battery case can operate at large applied current magnitudes (up to 100 kA) and thin electrolyte layer (down to 2 cm) and metal electrode thickness of about 20 cm for the large scale batteries of up to 8 m horizontal scale.

8.2 Further Work

This work has provided initial predictions of the large scale LMB interfacial stability accounting for the MHD effects. The work is purely theoretical and is based only on implementing reasonable approximations for numerous physical aspects governing stability of the system. So far no experiment has been designed explicitly to observe the effects described in this work. Although this Thesis provides an explanation for the observed phenomena, it does not include a description of important phenomena for the battery efficiency, like electro-chemistry, mass and heat transfer. Here are follow-up tasks that can be pursued for model extensions and the future research:

- Implementation of the Biot-Savart subroutine to account for the of time-dependent magnetic fields.

- Investigation of the stability in the system with large number of the small batteries
- Extension of the presently used hydrodynamic model to account for the effects of turbulent stresses and boundary layers
- Analysis of the current collector configuration impact on the stability and efficiency. Model extension to account for the dynamical control of the electric current distribution in the battery
- Implementation of the mass and heat transfer modules into the model accounting for the electrochemical phenomena
- Analysis of the battery thermal balance
- Addition and estimation of the motion induced ($\boldsymbol{u} \times \boldsymbol{B}$) current effects in the battery
- Comparison of the 3D and shallow water models and analysis of the applicability limits of the latter ones
- Validation of the results against the experiment

References

[1] D. J. Bradwell, H. Kim, A. H. C. Sirk, and D. R. Sadoway. "Liquid metal batteries: Past, Present, and Future". *Journal of American Chemical Society* 134 (2012), pp. 1895–1897.

[2] H. Kim, D. A. Boysen, J. M. Newhouse, B. L. Spatocco, B. Chung, P. J. Burke, D. J. Bradwell, K. Jiang, A. A. Tomaszowska, K. Wang, W. Wei, L. A. Ortiz, S. A. Barriga, S. M. Poizeau, and D. R. Sadoway. "Liquid metal batteries: Past, Present, and Future". *Chemical Reviews* 113 (2013), pp. 2075–2099.

[3] T. Ouchi, H. Kim, B. L. Spatocco, and D. R. Sadoway. "Calcium-based multi-element chemistry for grid-scale electrochemical energy storage". *Nature communications* 7:10999 (2016), pp. 1895–1897.

[4] D. H. Kelley and D. R. Sadoway. "Mixing in liquid metal electrode". *Physcis of Fluids* 26 (2014), pp. 057102–1–12.

[5] V. Bojarevics and M. V. Romerio. "Long waves instability of liquid metal-electrolyte interface in aluminium electrolysis cells: a generalization of Sele's criterion". *European Journal of Mechanics* B13 (1994), pp. 33–56.

[6] E. A. Brandes and G. B. Brook. "Smithells Metals Reference Book". *Elsevier* 7th Edition (1998).

[7] N. Weber, V. Galindo, J. Priede, F. Stefani, and T. Weier. "The influence of current collectors on Tayler instability and electro-vortex flows in liquid metal batteries". *Physics of Fluids* 27 (2015), pp. 014103–1–15.

[8] A. Solheim, K. S. Osen, C. Sommerseth, and O. E. Kongstein. "Liquid metal batteries as a power buffer in aluminium production plants". *Proceedings of 35th International ICSOBA Conference, Hamburg, Germany* (2017), pp. 945–954.

[9] N. Weber, V. Galindo, F. Stefani, and T. Weier. "Current-driven flow instabilities in large-scale liquid metal batteries, and how to tame them". *Journal of Power Sources* 265 (2014), pp. 166–173.

[10] D. S. Severo, V. Gusberti, A. F. Schneider, E. C. Pinto, and V. Potocnik. "Comparison of various methods for modeling the metal-bath interface". *Light Metals* (2008), pp. 379–384.

[11] C. Canuto, M. Y. Hussaini, A. Quateroni, and T. Zhang. "Spectral methods. Fundamentals in single domain". *Springer-Verlag Berlin Heidelberg* (2006).

[12] Z. Yang, J. Zhang, M. C. W. Kintner-Meyer, X. Lu, D. Choi, J. P. Lemmon, and J. Liu. "Electrochemical energy storage for green grid". *Journal of American Chemical Society* 111 (2011), pp. 3577–3613.

[13] H. Li, H. Yin, K. Wang, S. Cheng, K. Jiang, and D. R. Sadoway. "Liquid metal electrodes for energy storage batteries". *Advanced Energy Materials* (2016), pp. 1–19.

[14] J. M. Newhouse, S. Poizeau, H. Kim, B. L. Spatocco, and D. R. Sadoway. "Thermodynamic properties of calcium magnesium alloys determined by emf measurements". *Electrochemica Acta* 91 (2013), pp. 293–301.

[15] H. Kim, D. A. Boysen, T. Ouchi, and D. S. Sadoway. "Calcium-bismuth electrodes for large-scale energy storage (liquid metal batteries)". *Journal of Power Sources* 241 (2013), pp. 239–248.

[16] T. Ouchi, H. Kim, X. Ning, and D. S. Sadoway. "Calcium-antimony alloys as electrodes for liquid metal batteries". *Journal of Electrochemical Society* 161 (2014), A1898–A1904.

[17] X. Ning, S. Phadke, B. Chung, H. Yin, P. Burke, and D. S. Sadoway. "Self-healing Li-Bi liquid metal battery for grid-scale energy storage". *Journal of Power Sources* 275 (2015), pp. 370–376.

[18] P. Leung, S. C. Heck, T. Amietszajew, M. R. Mohamed, M. B. Conde, R. J. Dashwood, and R. Bhagat. "Perfonce and polarization studies of the magnesium-antimony liquid metal battery with the use of in-situ reference electrode". *Royal Society of Chemistry* 5 (2015), pp. 83096–83105.

[19] J. Xu, O. S. Kjos, K. S. Osen, A. M. Martinez, O. E. Kongstein, and G. M. Haarberg. "Na-Zn liquid metal battery". *Journal of Power Sources* 332 (2016), pp. 274–280.

[20] R. F. Ashour, H. Yin, T. Ouchi, D. H. Kelley, and D. S. Sadoway. "Communication - Molten amide-hydroxide-iodide electrolyte for a low-temperature sodium-based liquid metal battery". *Journal of Electrochemical Society* 164 (2017), A535–A537.

[21] J. Lee, S. H. Shin, J. K. Lee, S. Choi, and J. H. Kim. "Corrosion behavior of surface treated steel in liquid sodium negative electrode of liquid metal battery". *Journal of Power Sources* 307 (2016), pp. 526–537.

[22] J. A. Shercliff. "A textbook of magnetohydrodynamics". *Pergamon Press* (1965).

[23] V. Bojarevics, Ya. Freibergs, E. I. Shilova, and V. Shcherbinin. "Electrically Induced Vortical Flows." *Kluwer Academic Publishers, Dordrecht* 111 (1989), pp. 3577–3613.

[24] A. Beltran. "MHD natural convection flow in a liquid metal electrode". *Applied Thermal Engineering* 114 (2017), pp. 1203–1212.

[25] Y. Shen and O. Zikanov. "Thermal convection in a liquid metal battery". *Theoretical and Computational Fluid Dynamics* 30 (2016), pp. 275–294.

[26] A. Dattner, B. Lehnert, and S. Lundquist. "Liquid conductor model of instabilities in a pinched discharge". *Cambridge University Press* 9/1708 (1959), pp. 325–327.

[27] H. Goedbloed and S. Poedts. "Principles of Magnetohydrodynamics". *Cambridge University Press* (2004).

[28] G. Rudiger, M. Schultz, and M. Gellert. "The Tayler instability of toroidal magnetic fields in a columnar gallium experiment". *Asreonische Nachricten* 10 (2011), pp. 1–7.

[29] M. Seilmayer, F. Stefani, T. Gundrum, T. Weier, G. Gerbeth, M. Gellert, and G. Rudiger. "Experimental evidence for transient Tayler instability in a cylindrical liquid-metal column". *Physical Review Letters* 108 (2012), pp. 244501–1–4.

[30] T. Weier, A. Bund ans W. El-Mofid, G. M. Horstmann, C-C Lalau, S. Landgraf, M. Nimtz, M. Starace, F. Stefani, and N. Weber. "Liquid metal batteries - materials selection and fluid dynamics". *IOP Conference Series: Material Science and Engineering* 228 (2017), pp. 012013–1–14.

[31] F. Stefani, T. Weier, T. Gundrum, and G. Gerbeth. "How to circumvent the size limitation of liquid metal batteries due to the Tayler instability". *Energy Conversion and Management* 52 (2011), pp. 2982–2986.

[32] W. Herreman, C. Nore, L. Cappanera, and J. L. Guermond. "Tayler instability in liquid metal columns and liquid metal batteries". *Journal Fluid Mechanics* 771 (2015), pp. 79–114.

[33] J. Priede. "Elementary model of internal electromagnetic pinch-type instability". *Journal Fluid Mechanics* 816 (2017), pp. 705–718.

[34] T. Wiyan. "Shallow water hydrodynamics: Background in mechanics". *Elsevier Amsterdam* (1992), pp. 1–2.

[35] M. W. Dingemans. "Water wave propagation over uneven bottoms (Part 1): Wave on currents in the Boussinesq approximation". *World Scientific* (1997), pp. 476–487.

[36] V. Bojarevics. "Non-linear waves with electromagnetic interaction in aluminium electrolysis cells". *Progress in Astronautics and Aeronautics* 182 (1998), pp. 833–848.

[37] V. Bojarevics and J.W. Evans. "Mathematical modelling of Hall-Heroult pot instability and verification by measurements of anode current distribution". *TMS Light Metals* 4 (2015), pp. 783–788.

[38] V. Bojarevics and A. Tucs. "MHD of large scale liquid metal batteries". *TMS Light Metals* (2017), pp. 687–692.

[39] T. Sele. "Instabilities of the metal surface in electrolyte alumina reduction cells". *Metallurgical Transactions B* 8B (1977), pp. 613–618.

[40] N. Urata. "Magnetics and metal pad instability". *Light Metals* (1985), pp. 581–589.

[41] A. D. Sneyd. "Stability of fluid layers carrying a normal electric current". *Journal Fluid Mechanics* 156 (1985), pp. 223–236.

[42] R. J. Moreau and D. Ziegler. "Stability of aluminium cells: a new approach". *Light Metals* 131 (1986), pp. 359–364.

[43] A. D. Sneyd and A. Wang. "Interfacial instability due to MHD mode coupling in aluminium reduction cells". *Journal Fluid Mechanics* 263 (1994), pp. 343–359.

[44] P. A. Davidson and R. I. Lindsay. "Stability of interfacial waves in aluminium reduction cells". *Journal Fluid Mechanics* 362 (1998), pp. 273–295.

[45] R. J. Moreau and J. W. Evans. "An analysis of the hydrodynamics of aluminium reduction cells". *Journal of Electrochemical Society* (1984), pp. 2251–2259.

[46] W. Rodi. "Examples of calculation methods for flow and mixing in stratified fluids". *Journal of Geophysical Research* 92 (1987), pp. 5305–5328.

[47] S. Chandrasekhar. "Hydrodynamic and hydromagnetic stability: The analysis into normal modes". *Dover Publications Inc.* (2003), p. 24.

[48] O. Zikanov. "Metal pad instabilities in liquid metal batteries". *Physical Review E* 92 (2015), pp. 063021–1–8.

[49] D. Munger and A. Vincent. "A cylindrical model for rotational MHD instabilities in aluminium reduction cells". *New York: Wiley* 22 (2017), pp. 363–382.

[50] V. Bojarevics and J. W. Evans. "An application of the inverse solution for electric current distribution from magnetic field measurements in aluminium electrolysis cells". *Journal of Iron and Steel Research, International* 19 (2012), pp. 561–565.

[51] V. Bojarevics and K. Pericleous. "Comparison of MHD models for aluminium reduction cells". *TMS Light Metals* (2006), pp. 347–352.

[52] N. Weber, P. Beckstein, W. Herreman, G. M. Horstmann, C. Nore, F. Stefani, and T. Weier. "Sloshing instability and electrolyte layer rupture in liquid metal batteries". *Physics of Fluids* 29 (2017), pp. 054101–1–15.

[53] H. Rusche. "Computational fluid dynamics of dispersed two phase flows at high phase fractions". *PhD thesis, Imperical College London* (2006).

[54] J. U. Brackbill, D. B. Kothe, and C. Zemach. “A continuum method for modeling surface tension”. *Journal of Computational Physics* 100 (1992), pp. 335–354.

[55] H. K. Moffatt S. S. Molokov R. Moreau. “Magnetohydrodyanmics: Historical Evolution and trends: Numerical modelling for electromagnetic processing of materials”. *Springer Science and Business Media* (2007), pp. 357–374.

[56] P. A. Davidson. “An introduction to magnetohydrodynamics”. *Cambridge University Press* (2001).

[57] D. Johnson. “Chebyshev polynomials in the spectral tau method and applications to eigenvaue problems”. *Nasa Constractor Report* 198451 (1996).

[58] J. C. Mason and D. C. Handscomb. “Chebyshev polynomials”. *Chapman and Hall/CRC* (2002).

[59] J. P. Boyd. “Chebyshev and Fourier spectral methods: Integration pf periodic functions and the trapezoidal rule”. *Dover Publications, Inc.* (2003).

[60] V. Bojarevics. “Interfacial MHD waves due to the dynamic electric current interaction in an aluminium electrolysis cell”. *Magnetohydrodynamics* 4 (1992), pp. 47–55.

[61] A. Robino, P. Brandt, and R. Weigle. “On the dynamics of internal waves in a nonlinear, weakly nonhydrostatic three-layer ocean”. *Journal of Geophysical Research* 106 (2001), pp. 26899–26915.

[62] J. Lighthill. “Waves in fluids: Water waves”. *Cambridge University Press* (2005), pp. 325–327.

[63] L. D. Landau and E. M. Lifshitz. “Fluid dynamics: Damping of gravity waves”. *Pergamon press* (1987), pp. 92–94.

[64] Q. Wang, B. Li, Z. He, and N. Feng. “Simulation of magnetohydrodynamic multiphase flow phenomena and interface fluctuation in aluminum electrolytic cell with innovative cathode”. *Metallurgical and Material Transactions B* 45B (2014), pp. 273–294.

[65] A. Pedchenko, S. Molokov, and B. Bardet. “The effect of "wave breakers" on the magnetohydrodynamic instability in aluminium reduction cells”. *Metalurgical and Materials Transactions B* 48 (2017), pp. 6–10.

[66] F. R. Gantmacher. "Application of the Theory of Matrices: The Routh-Hurwitz theorem". *New York: Wiley* 29 (1959), pp. 226–233.

[67] G. M. Horstmann, N. Weber, and T. Weier. "Coupling and stability of interfacial waves in liquid metal batteries". *Journal of Fluid Mechanics* 845 (2018), pp. 1–35.

[68] A. Zarouni, L. Mishra, M. Basataki, A. A. Jasmi, A. Arkhipov, and V. Potocnik. "Mathematical model validation of aluminium electrolysis cell at Dubal". *TMS Light Metals* (2013), pp. 597–602.

[69] O. Zikanov, A. Thess, P. A. Davidson, and D. P. Ziegler. "A new approach to numerical simulation of melt flows and interface instability in Hall-Heroult cells". *Metallurgical Transactions B* 31B (1999), pp. 1541–1550.

[70] V. Bojarevics. "Effect of cathode collector copper inserts on the Hall-Heroult cell MHD stability". *TMS Light Metals* (2016), pp. 933–938.

Chapter 9

Publications and conference presentations produced by this research

1. **A. Tucs**, **V. Bojarevics**, **K. Pericleous**. MHD stability of large scale liquid metal batteries. *J. Fluid Mech.*, accepted.

2. **V. Bojarevics**, **A. Tucs**. Large Scale Liquid Metal Batteries. *Magnetohydrodynamics*, Vol. 53, No. 4, 677 - 686, 2017.

3. **V. Bojarevics**, **A. Tucs**, **K. Pericleous**. MHD of Large Scale Liquid Metal Batteries. *Light Metals 2017*, Part of the series The Minerals, Metals & Materials Series, 687 - 692, 2017.

4. **V. Bojarevics**, **A. Tucs**, **K. Pericleous**. MHD Flow Model for Liquid Metal Batteries. TMS 2016 145^{th} Annual Meeting and Exibition, February 14-18, 2016, Nashville, Tennessee, USA.

5. **V. Bojarevics**, **A. Tucs**, **K. Pericleous**. MHD Model for Liquid Metal Batteries. 10^{th} PAMIR International Conference Fundamental and Applied MHD, June 20-24, 2016, Cagliari, Sardinia, Italy.

6. **A. Tucs**, **V. Bojarevics**, **K. Pericleous**. Renewable Energy Supply and Storage: Liquid Metal Batteries. EGL 2016 workshop on numerical mathematics, June 7, 2016, University College London, London, UK.

7. **A. Tucs**, **V. Bojarevics**, **K. Pericleous**. MHD Model for Liquid Metal Battery description. Inaugural UK Fluids Conference, September 7-9, 2016, Imperial College London, London, UK.

8. **A. Tucs**. MHD stability of Liquid Metal Batteries. The Sustainable Researcher, April 27, 2017, University of Greenwich, London, UK.

9. **V. Bojarevics**, **A. Tucs**, **K. Pericleous**. Magnetically Stabilised Large Scale Liquid Metal Batteries. International workshop on liquid metal battery fluid dynamics (LMBFD2017), May 16 - 17, 2017, Dresden, Germany.

10. **A. Tucs**, **V. Bojarevics**, **K. Pericleous**. MHD stability of Liquid Metal Batteries. International workshop on liquid metal battery fluid dynamics (LMBFD2017), May 16 - 17, 2017, Dresden, Germany.

11. **V. Bojarevics**, **A. Tucs**. Large Scale Liquid Metal Batteries. High Temperature Batteries for Stationary Energy Storage Workshop, September 19 - 20, 2017, Trondheim, Norway.

12. **A. Tucs**, **V. Bojarevics**, **K. Pericleous**. Long waves instability due to MHD mode coupling in liquid metal batteries. High Temperature Batteries for Stationary Energy Storage Workshop, September 19 - 20, 2017, Trondheim, Norway.